Characterizing the soil uncertainty in the Port of Rotterdam for the probabilistic design of a pile foundation

Z.Y. Fan

TU Delft

Characterizing the soil uncertainty in the Port of Rotterdam for the probabilistic design of a pile foundation

By

Zhi Yang Fan

To obtain the degree of Master of Science

Section Flood Risk,

Faculty of Civil Engineering and Geosciences

Delft University of Technology,

to be defended publicly on June 20, 2022

Student number: 4477413

Thesis committee:	Prof. dr. K.G. Gavin,	TU Delft, Chair
	Dr. ir. O. Morales Napoles,	TU Delft
	Dr. ir. R.C. Lanzafame,	TU Delft
	Ir. K.J. Duffy,	TU Delft, Daily supervisor

Cover photo: Amaliahaven quay wall under construction. Source: Port of Rotterdam

An electronic version of this thesis is available at https://repository.tudelft.nl/

TU Delft

Preface

The spatial variability of soil properties and the heterogeneity of soils in general are aspects of the geotechnical design that cannot be ignored. When I first started this thesis, I thought that it was quite straightforward to detrend the cone resistance data and compute the vertical scale of fluctuation. Unfortunately, I did not take into account the pleasure of manually identifying the Pleistocene sand layer in every CPT which I had to do it again whenever I corrected my methods. Furthermore, it was quite an adjustment in mindset when detrending where you normally just mindlessly fit a line through your data but in this case you had to be reminded that the trend line had a physical meaning. Which meant that your mathematical best fit was not necessarily the physically correct one. In the end, through trial and error I managed to finish this thesis.

Finally, I would like to express my thanks to my supervisor Kevin Duffy for his guidance and support. I would like to thank the other members of my committee Ken Gavin, Oswaldo Morales Napoles and Robert Lanzafame for their comments and input in writing this report.

Zhi Yang Fan
March 2022

Abstract

The Port of Rotterdam (PoR) is the largest port in Europe and in order to maintain its status, it would need to expand. For the expansion, an extensive survey of the subsurface is needed for the construction of new port areas and its geotechnical structures. As part of designing the geotechnical structures, the subsurface is often modelled as multiple homogeneous soil layers. However the soil properties are in reality heterogeneous and spatially variable. The spatial variability of a soil property is characterized by a mean, a standard deviation and the scale of fluctuation. The scale of fluctuation is the distance over which a soil property is significantly correlated and it is limited to the soil layer of that soil property. Therefore the change in the geological layering of the soil because of external depositional factors such as river, sea and wind can influence the scales of fluctuations and the resulting geotechnical design.

The objective of this thesis is to look at the spatial variability in the vertical direction of the Pleistocene sand from the Kreftenheye and Boxtel Formation in the Port of Rotterdam and see if the river Meuse has any influence on the spatial variability in the vertical direction. An additional question is asked if the spatial variability has any influence on the computation of the pile base capacity for a single foundation pile and what are the implications of the answer to that question. To answer these questions, four sites in the Maasvlakte, Botlek and Pernis were selected and the cone penetration tests (CPTs) taken at the twelve sites were used for this thesis. An empirical method which uses CPT data to identify soil layers was used to identify the Pleistocene sand layer in the CPT data. The first part of the thesis uses the cone resistance data of the CPTs to estimate the spatial variability of the sites.

The second part of the thesis focuses on the additional research question by using random field theory. Per site, the mean, standard deviation and vertical scale of fluctuation θ_v were used to generate simulations of cone resistance data. For each combination of standard deviation and θ_v 500 simulations were carried out. For each simulation the pile base capacity was computed with two CPT-based averaging methods, Koppejan method and LCPC method. The coefficient of variation of pile base capacity is used to measure the uncertainty of the computed pile base capacity.

The results show that the range θ_v values are: 0.26 – 2 m in the Maasvlakte, 0.24 – 1.76 m in the Botlek and 0.14 – 1.18 m in Pernis. In terms of the mean θ_v, you see a gradual increase from the upstream area (Pernis) to the downstream area (Maasvlakte). The increase is from 0.27 – 0.63 m in Pernis to 0.64 – 0.80 m in Botlek to 0.84 – 1.86 m in Maasvlakte. However, it is not clear if this is due to the Meuse or due to the existence of sublayers in the geological formation or due to some other factor. Further investigation is needed before a conclusive answer can be given. The answer for the second part is that as long θ_v is significantly larger than the pile diameter D $(\theta_v \geq 4D)$, it does not influence the uncertainty of the computed pile base capacity. However, the mean and standard deviation of cone resistance does influence the uncertainty of the computed pile base capacities. Finally, it is observed that spatial variability does not play a role in the uncertainty of the computed pile base capacity if the coefficient of variation of the cone resistance $c_v(q_c)$ is small $(c_v(q_c) \leq 0.15)$. The implication for the uncertainty of the computed pile base capacity and therefore the pile design is that one can afford to have a less accurate description of the spatial variability from using fewer CPTs if $\theta_v \geq 4D$. The same holds true if $c_v(q_c) \leq 0.15$.

Contents

List of Figures

List of Tables

List of symbols

Parameter	Unit	Description
a	-	Net area ratio
A_c	mm^2	Area of the cone
A_s	mm^2	Surface area of the friction sleeve
$c_v(\dots)$	-	Coefficient of variability
d	mm	diameter load cell support
d_c	mm	Cone diameter
D	mm	Cone or pile diameter
f_s	MPa	Friction sleeve
F_r	-	Normalized friction ratio
F_s	N	Total force acting on friction sleeve
H_d	m	Development distance
H_s	m	Sensing distance
I_B	-	Bartlett's limit
I_c	-	Soil Behavior Type Index
k_c	-	End bearing capacity factor
n	-	Variable stress exponent
p_a	kPa	Atmospheric pressure
P_f	-	Probability of failure
q_b	MPa	Unit bearing capacity
q_c	MPa	Cone resistance
q_t	MPa	Corrected cone resistance
Q_b	kN	Pile base capacity
Q_c	N	Total force acting on cone
Q_s	kN	Total shaft capacity
Q_t or Q_{tn}	-	Normalized cone resistance
Q_T	kN	Total pile capacity
R	-	Resistance variable
R^2	-	Coefficient of determination
R_f	-	Friction ratio
S	-	Load variable
u_2	MPa	Pore pressure
Z	-	Limit state
ε	-	Residuals
γ	kN/m^3	Soil unit weight
γ_w	kN/m^3	Unit weight water
μ	-	Mean
σ	-	Standard deviation
σ'_{vo}	MPa	Effective vertical stress
σ_{vo}	MPa	Total vertical stress
τ	m	Separation distance
θ	m	Scale of fluctuation
θ_h	m	Horizontal scale of fluctuation
θ_v	m	Vertical scale of fluctuation

List of abbreviations

Abbreviation	Description
AAOP	Anthropogenic deposits
ACF	Autocorrelation function
ACFM	Autocorrelation fitting method
ANAWA	Naaldwijk Formation, Walcheren Member
BRO	Dutch: *Basisregistratie Ondergrond*
CPT	Cone penetration test
CPTu	Cone penetration test + pore pressure measurement
DGM	Digital Geological Model
DINO	Dutch: *Data en Informatie van de Nederlandse Ondergrond*
EC	Echteld Formation
GDN	Dutch: *Geologische Dienst Nederland*
GEF	Geotechnical Exchange Format
GWT	Groundwater table
HVI	Horizontal variability index
KRBXDE	Kreftenheye and Boxtel Formation, Delwijnen Member
KRWY	Kreftenheye Formation, Wijchen Bed
KTT	Kendall tau test
LN	Lognormal distribution
LAS	Local average subdivision
LSF	Limit state function
MC	Monte Carlo approach
MLE	Maximum likelihood estimation
N	Normal distribution
NAP	Dutch: *Normaal Amsterdams Peil*
NAWO	Naaldwijk Formation, Wormer Member
NIBA	Nieuwkoop Formation, Basisveen Bed
OLS	Ordinary least squares
PoR	Port of Rotterdam
PZWA	Peize and Waalre Formation
SBT	Soil Behavior Type
SBT_n	Normalized Soil Behavior Type
SF	Scale of fluctuation
SPT	Standard penetration test
SVF	Semivariogram function
SVFM	Semivariogram fitting method
SVR	Site variability rating
TNO	Dutch: *Nederlandse Organisatie voor toegepast-natuurwetenschappelijk onderzoek*

1. Introduction

1.1. Background

The Port of Rotterdam (PoR) is known as the largest seaport in Europe and it is an important transit hub for global and European cargo transport. In 2019 with a market share of 36.4%, it was by far the largest port of in Europe in terms of the total throughput in the Hamburg-Le Havre range as the port of Antwerp was only second with a market share of 18.4% as stated in the highlights of the annual report of the Port of Rotterdam Authority (2019).

The current position of the largest seaport in Europe is due to the continued expansion and development along the Nieuwe Maas and Nieuwe Waterweg. Along with that expansion and development came the construction of the Europoort area in the 1960s and the Maasvlakte area in the 1970s. The Maasvlakte 2 was the most recent civil engineering project that expanded the Maasvlakte and it opened in 2013.

The construction of these port areas require i.e. quay walls and its foundations to be built and that requires a comprehensive understanding of the subsurface. The usual method for retrieving data about the subsoil is by performing a preliminary site investigation using a cone penetration test (CPT). Cone penetration tests (CPTs) are the most commonly used method for initial geotechnical tests at a site. The CPT data is crucial for calculating the bearing capacity of the soil, determining the soil layers and estimating the soil parameters. With data one can calculate whether the soil is strong enough to resist static loads like self-weight of a structure and dynamic loads like the wave load.

In order to maintain its leading position as the largest seaport of Europe, the PoR will continue to expand and develop seaward by either expanding the Maasvlakte or by creating entire new port areas. However, there is not many CPT data close to the coast or at sea as most CPT soundings were done on land or in rivers. Thus one has to characterize the subsurface soil properties at the construction site by using the CPT data at discrete points in the area. One can only do so by characterizing the spatial variability of the soil and use that information to estimate the soil properties within the construction site.

The problem of estimating the soil properties within the construction site with only CPT data at discrete points, is also present in existing design methods. Thus the spatial variability of the soil derived from CPT soundings and the resulting probabilistic design calculations must be taken into account for existing design methods.

This thesis will describe the spatial variability of the soil in the PoR and evaluate the role it plays in the design methods by incorporating the spatial variability in the probabilistic calculation of a foundation pile’s base capacity.

1.2. Problem Definition

After years of continued expansion and development along the Nieuwe Maas and Nieuwe Waterweg, numerous CPTs have been completed in the Port of Rotterdam to support the design and assessment of numerous structures, such as foundation piles or quay walls. The number of CPTs done in the Port of Rotterdam is in the thousands as DINOloket, a public database of CPTs, says that the Maasvlakte alone contains roughly 3500 CPTs.

This large test database can be used to characterize uncertainty in subsurface soil properties, which can then be applied to the design of various geotechnical and hydraulic structures or to evaluate existing design methods. The information and evaluation of design methods will be important when the Port of Rotterdam decides to expand by building more offshore constructions like the Maasvlakte 2.

This thesis will look at three areas: Maasvlakte, Botlek and Pernis. Per area, four specific sites will be investigated. This results in a total of 155 CPTs being used for this thesis. 59 CPTs in the Maasvlakte, 26 CPTs in the Pernis and 70 CPTs in the Botlek. The individual CPTs and their depths are summarized in the appendices. The scope of the thesis will give more information about the criteria that were used to select the CPTs.

1.3. Research Questions

The objective of the thesis is to first describe the spatial variability of the soil in the Port of Rotterdam. Secondly, it is to see whether the presence of a river has a significant influence when one wants to describe the spatial variability of the soil. To be more specific, it is to see whether one can expect a higher or lower spatial variability in port areas close to the sea like the Maasvlakte compared to port areas located in the river like Pernis and Botlek.

The importance of these matters are demonstrated by looking at the design situation of a quay wall supported by foundation piles. The foundation pile is loaded with an axial load that has a certain distribution and one has to calculate the pile base capacity of the foundation pile and the probability of failure for that foundation file. Based on the research objectives, the following research questions have been formulated:

- Which method/model can be used to quantify the spatial variability of the soil in the Kreftenheye and Boxtel Formation, Delwijnen Member in the Port of Rotterdam?
- Does the river Meuse have an influence on the spatial variability of the soil? If so, how significant is that influence?
- How large is the influence of the spatial variability on the pile base capacity of a single foundation pile? And how does it affect the probabilistic design of the foundation pile?

1.4. Scope of the thesis

The thesis is about characterizing the spatial variability of the soil at the PoR and how it impacts the design of a single foundation pile. In order to answer the research questions, the scope of the thesis is defined as follows:

- The Maasvlakte, Botlek and Pernis are the geographical areas in which the research questions will be answered. The Maasvlakte is a relatively new area and part of the expansion of the Port of Rotterdam. In the future, either the Maasvlakte will be expanded or new areas around it will be created and the characterization of the spatial variability in that area will be useful. Furthermore, it will serve as the area in which the river Meuse has no influence on the spatial variability whereas the Botlek and Pernis will function as areas in which the influence of the river Meuse is fully present in the spatial variability.
- The 155 CPTs that will be used in this thesis to characterize the spatial variability, fulfilled the following conditions:
    1. The CPT must be least be carried out to a minimum depth of -40 m NAP. For foundation piles in the west of the Netherlands, the base of the foundation pile is usually around -25 to -30 m NAP as it is around that depth that the Pleistocene sand layer with high cone resistances is found. The foundation pile usually relies on that sand layer for its bearing capacity.
    2. The CPT must have been carried out in 1982 or in later years. This is because before 1982 there were no Dutch standards for the CPT equipment nor were there standards for the tests themselves.
    3. All CPTs in the Maasvlakte need to include the pore pressure u_2 in their measurements so that the number of available CPTs is limited to reasonable limits. The mechanical CPTs in the Maasvlakte must be carried out following

the 2009 Dutch standard, *NEN-EN-ISO 22476-12:2009: Geotechnical investigation and testing – Field testing – Part 12: Mechanical cone penetration test (CPTM)*. For electronic CPTs, they must be carried following the 1996 Dutch standard, *NEN 5140: Geo-engineering - Establishing the cone resistance and the local cohesive strength of sediment - Electrical cone penetration testing method (1996, first edition).*

- Only the pile base capacity will be calculated for the bearing capacity of the foundation pile. In formulae, the total pile capacity can be split into two components: (1) the pile base capacity and (2) the pile shaft capacity. In the west of the Netherlands, there is typically soft clay and peat layers up to a depth of -20 m NAP while the base of the foundation pile is somewhere around -25 to -30 m NAP. The soft clay and peat layers can cause negative skin friction which will reduce the pile shaft capacity in reality. Thus, the real bearing capacity will be much lower than calculated one and it will therefore mostly rely on the pile base capacity.
- CPT-based averaging techniques such as the Koppejan and LCPC method will be used to calculate the pile base capacity.
- The focus will be on the Pleistocene sand layer that belong to the geological formation Kreftenheye and Boxtel Formation, Delwijnen Member. This geological formation mainly consists of fluvial deposits so the influence of the river Meuse is seen more clearly and the soil in the Port of Rotterdam at -25 to -30 m NAP belongs to that geological formation.
- This thesis will only discuss the spatial variability in the vertical direction.

1.5. Outline of the thesis

The first research question is discussed in Chapter 2 with a literature review. It will give a general explanation about CPTs and how it can be used to estimate the different soil types in the subsoil and it will also describe the soil heterogeneity and the spatial variability of soils. There will also be some background about the types of geological formations that can be found in the PoR and what the calculation methods are for determining the bearing capacity of a foundation pile as well as some knowledge about the probabilistic design method.

Chapter 3 will present the methodology that will be used for this research and there will be some elaborations for the choices that were made for this research.

Chapter 4 will answer the other research questions by presenting the results using the methodology explained in Chapter 3. The calculated spatial variability values will be compared to each other and there will be comparisons between the different areas so as to answer the second research question. The results will be used together with random field theory to answer the third and fourth research questions.

The final chapter, Chapter 5, will contain the conclusion of the research as well as some recommendations.

2. Literature Review

This chapter presents a general introduction to CPT, Soil Behavior Type (SBT) and Soil Behavior Type Index (I_C), the concept of soil heterogeneity and spatial variability and how said variability can be quantified. It also includes the calculation methods for the pile base capacity of a foundation pile and some information about the geology in the PoR. A brief review of random field theory will also be given as that will be necessary for answering the last research question.

2.1. Cone Penetration Test

In geotechnical engineering, information about the subsoil is required to make a geotechnical design. The information is obtained by investigating the site itself through in-situ tests or through laboratory tests. Through those tests, the soil parameters that characterize the subsoil can be accurately estimated. Usually an in-situ test is performed as it does not disturb the soil as much as a laboratory test would have.

Among the in-situ test methods, the cone penetration test (CPT) and the standard penetration test (SPT) are the most well-known ones. The SPT is executed by driving a tube into the soil and it registers the number of blows needed to hammer the tube 1 foot into the soil as the N-value. From the N-value the characteristics of the soil are derived using empirical formulae.

The CPT method is the main in-situ test method in the Netherlands as it is a more suitable method for the Dutch subsurface than the SPT method. It is executed by pushing a tube with a cone at the front and a friction sleeve behind it, into the ground at a constant rate and continuous measurements are made of the cone resistance q_c and the sleeve resistance f_s. Figure 2.1 displays a CPT cone with a friction sleeve which is the thicker part at the middle of the tube. The reliability of the cone resistance measurements depend on the type of cone used, mechanical or electronic, and on the zone of influence of the cone resistance.

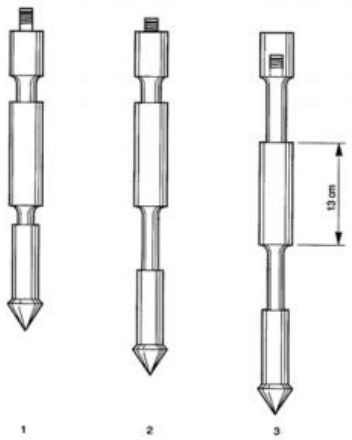

Figure 2.1: Begemann type cone with friction sleeve. Source: Robertson and Cabal (2015)

History of CPT cones

The first CPT cone in 1932 were mechanical as the inner push rods were used to push the cone into the soil and measurements were taken of how much force was needed to push the cone. From that you only got the cone resistance as your output parameter. In later years the geometry of the cone was improved to prevent soil from entering the gap between the casing and inner push rods and a friction sleeve was added to measure the sleeve resistance.

In 1965, Fugro developed an electric cone whose design later became the blueprint for modern cones. The cone resistance was measured at the cone tip and they were transmitted

through a cable. This meant that there was “continuous testing with continuous rate of penetration without the need for alternate movements of different parts of the penetrometer and no undesirable soil movements influencing the cone resistance” (Robertson & Cabal, 2015, p. 9) and “simpler and more reliable electrical measurement of cone resistance and sleeve friction resistance” (Robertson & Cabal, 2015, p. 9). Meaning that with an electric cone, one could measure at the same location twice and in both instances you would get the same data.

In 1974, the CPTu was introduced in which next to the q_c and the f_s the pore pressure would be measured as well. The cone penetrometers (piezocones) would have a pore pressure filter installed close to the cone and the recommended position for the filter is the u_2 location which is just above the base of the cone. Hence why pore pressure is usually noted in formulae and measurements as u_2. With the pore pressure filters the q_c can be corrected for pore pressure effects which is especially important in soft clays. More information about CPT can be found in the CPT Guide of Robertson and Cabal (2015).

Zone of influence of the cone resistance

The cone resistance is influenced by the soil ahead and behind the cone tip. This is because of the influence of adjacent soil layers and that influence is characterized by the sensing distance H_s and the development distance H_d. The sensing and development distances are usually expressed as a function of the cone or pile diameter.

When a cone penetrometer transitions from a weak layer to a strong layer, there is a transition zone in which the cone starts to deviate from its steady-state q_c. That transition starts as the cone penetrometer senses the strong layer before it touches the interface of the two layers and it ends when the cone has reached a steady-state q_c in the strong layer.

The sensing distance H_s is the vertical distance between the start of the transition zone and the interface. The development distance H_d is the vertical distance between the end of the transition zone and the interface. This explanation is illustrated in Figure 2.2. As such, the identification of the transition zones from one soil layer to another are not only important for correctly identifying the soil layers but it is also important for getting a reliable and representative cone resistance value for the given soil layers. There will be an under- or overestimation of the soil strength if the transition zones are not taken into account.

Tehrani et al. (2018) looked at the influence of the layer interface on the cone penetration resistance in layered sands. Using a model cone penetrometer with a diameter d_c = 31.75 mm, it estimated the sensing and development distances for different combinations of two-layered sands with different relative densities. The results of their experiments are summarized in Table 2.1. The table expresses the sensing and development distances as a ratio of the cone diameter. The significance of the results are that if you were to switch the two layered sands you cannot simply switch the sensing and development distances. Furthermore, there is no clear relationship between the transition from weak to strong and the sensing and development distances. So one cannot make use of a rule of thumb to roughly estimate the sensing and development distances.

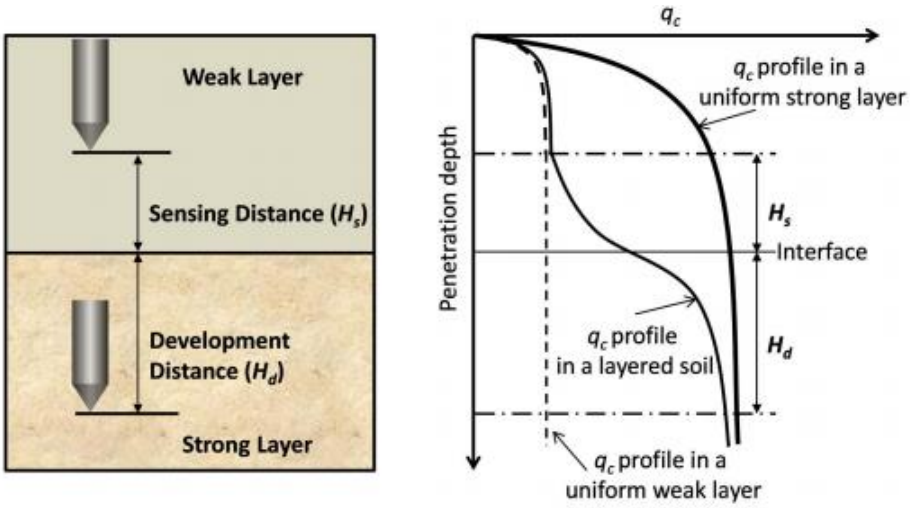

Figure 2.2: Sensing and development distance. Source: Tehrani et al. (2018)

Test	Sensing depth $\frac{H_s}{d_c}$	Development depth $\frac{H_d}{d_c}$
Loose over dense	2.8-3.0	3.8-3.9
Dense over loose	5.1	2.2-2.4
Medium dense over dense	4.7	4.2
Dense over medium dense	2.5	5.4

Table 2.1: Summary of test results of Tehrani et al. (2018) (adapted). Source: Tehrani et al. (2018)

Ahmadi and Robertson (2005) looked at the effect that thin layers have on the q_c measurements. Using a cone penetrometer with a diameter d_c = 31.75 mm, their setup was a thin sand layer in a clay deposit. As part of their research they also performed an analysis on two-layered soil with (1) loose sand over dense sand, (2) dense over loose sand, (3) clay on medium dense sand and (4) medium dense sand on clay. Loose sand has a relative density of D_r = 30% and dense sand has a relative density of D_r = 90%. The medium dense sand has a relative density D_r = 50%. The results of the two-layered soil analysis is summarized in Table 2.2.

Ahmadi and Robertson (2005) note that the depth where the cone senses the layer interface can easily be identified by the deviation from the constant q_c line in a layer. However there are cases where the change is gradual due to the layers properties having a small difference. This would make it harder to identify the depth at which the cone senses the layer interface and one would have to rely on their own judgement to estimate the sensing distance.

Test	Sensing depth $\frac{H_s}{d_c}$	Development depth $\frac{H_d}{d_c}$
Loose over dense	4.2 (0.15 m)	10 (0.35 m)
Dense over loose	18 (0.65 m)	8.4 (0.30 m)
Sand on clay	10 (0.35 m)	1.7 (0.05 m)
Clay on sand	1.7 (0.05 m)	6 (0.20 m)

Table 2.2: Summary of two-layered soil analysis of Ahmadi and Robertson (2005) (adapted). Source: Ahmadi and Robertson (2005)

For the thin sand layer in a clay deposit, the result was that if it were a dense sand layer a minimum thickness of 1.05 m (28 cone diameters) is needed to reach the fully mobilized cone tip resistance. For a loose sand layer, a minimum thickness of 0.15 m (4 cone diameters) is needed to reach the fully mobilized cone tip resistance.

As one can see, there is no theoretical or empirically derived equation to estimate the sensing and development distances. Any estimation would either have been derived

empirically from lab experiments or it has been taken from existing literature wherein the situation matches the setup described in the literature.

2.2. Soil Behavior Type and Index

It is know by geotechnical engineers that CPT data can be used in order to estimate the soil layers and generate a soil profile with a soil type classification system. This is typically done by linking the soil type with the cone parameters: q_c and the friction ratio $R_f \left(= \frac{f_s}{q_c}\right)$. The prediction of soil type using CPT data is what is known as Soil Behavior Type (SBT) and the relationship between cone parameters and soil type are summarized in a SBT classification chart as shown in Figure 2.3.

However, it must be stressed that one should not expect these charts to provide with an accurate prediction of the soil type based on grain distribution or any other physical properties but rather it serves as guide to the different soil behavior types using the soil's mechanical properties as stated by Robertson (1990).

The early charts such as the one in Figure 2.3 are simplified versions which uses q_c and R_f. Without simplification, the chart would use the corrected cone resistance q_t instead of q_c as the pore pressure u_2 had to be taken into account. This is especially true for clay and peat layers. For sand layers one can assume that $q_t = q_c$. The corrected cone resistance would be calculated as:

$$q_t = q_c + (1 - a) * u_2 \quad \textbf{(2.1)}$$

where a is the net area ratio which is determined as the ratio over the load cell support diameter and the cone diameter as shown in Figure 2.4.

Charts such as the one in Figure 2.3 were done without taking into account "that q_c, f_s and u_2 all intend increase with increasing overburden stress" (Robertson, 1990, p. 154). Due to this, some error can be expected in classifying the soils using a SBT chart for CPT profiles at large depths. To solve this problem the CPT data was normalized to take into account the influence of the overburden stress. Robertson (1990) came with the first normalized SBT (SBT_n) chart shown in Figure 2.5. The chart was then divided into 9 SBT_n zones and each describe a soil type: (1) sensitive fine-grained; (2) clay – organic soil, (3) clays: clay to silty clay; (4) silt mixtures: clayey silt to silty clay; (5) sand mixtures: silty sand to sandy silt; (6) sands: clean sands to silty sands; (7) dense sand to gravelly sand; (8) stiff sand to clayey sand; and (9) stiff fine-grained.

In order to simplify the usage of that SBT_n chart, a Soil Behavior Type Index (I_C) was introduced by Jefferies and Davies (1993). The I_C is a function of the normalized cone resistance Q_t and the normalized friction ratio F_r. On Robertson (1990) $Q_t - F_r$ chart, the I_C is the radius of concentric circles that would represent the boundaries of the SBT_n zones as shown in Figure 2.5. By calculating the I_C value, one can make a simple determination to which soil type the I_C value belongs to.

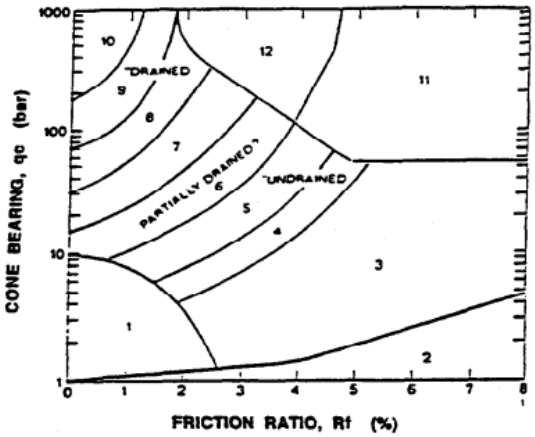

ZONE	SOIL BEHAVIOUR TYPE
1	sensitive fine grained
2	organic material
3	clay
4	silty clay to clay
5	clayey silt to silty clay
6	sandy silt to clayey silt
7	silty sand to sandy silt
8	sand to silty sand
9	sand
10	gravelly sand to sand
11	very stiff fine grained (*)
12	sand to clayey sand (*)

(*) overconsolidated or cemented

Figure 2.3: Simplified SBT chart for standard electric friction cone. Source: Robertson et al. (1986).

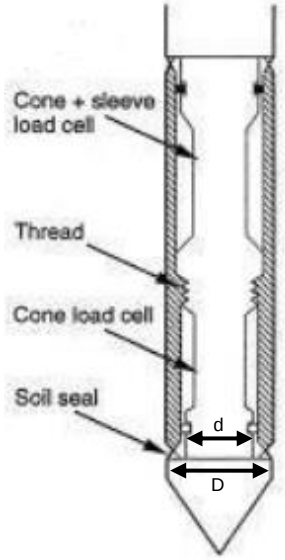

Figure 2.4: Piezo-friction-cone penetrometer where the net area ratio equals d/D. Source: Robertson and Cabal (2015)

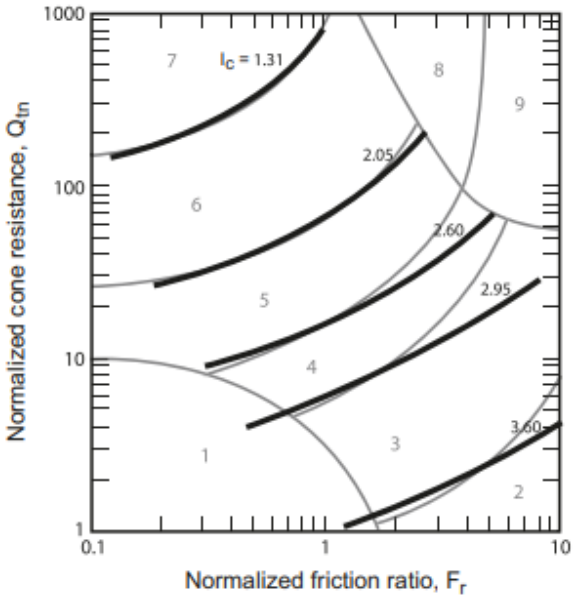

Figure 2.5: I_C (thick lines) on the normalized SBT_n $Q_t - F_r$ chart from Robertson (1990). Source: Robertson (2009)

A more recent investigation about SBT and SBT_n chart is from Robertson (2009) in which a variable stress exponent n is introduced. As with any normalized SBT_n chart, the soil unit weight γ and the groundwater table (GWT) need to be known in order to calculate the vertical total stress σ_{v0} and vertical effective stress σ'_{vo}. The stresses are necessary for computing the normalized cone resistance.

As we have only CPT data which contains the mechanical properties of the soil and not the physical properties, an estimation has to be made for the soil unit weight. There are several formulas and tables for making such estimations. The soil unit weight estimation from Lunne et al. (1997) was for the non-normalized SBT chart of Robertson et al. (1986). Mayne (2006) had a formula for estimating the dry soil unit weight but that was dependent on the measurements of the shear velocity and it required some iterations. Robertson and Cabal (2010) came up with a formula to estimate the soil unit weight from the CPT data. The formula itself is the result of combining correlations from previous studies and simplifying it into a simplified correlation between soil unit weight and CPT measurements. Next to the formula of Robertson and Cabal (2010), a soil unit weight estimation formula for specifically clay and peat was created by Lengkeek et al. (2018).

The soil unit weight estimation equation of Robertson and Cabal (2010) is shown below:

$$\frac{\gamma}{\gamma_w} = 0.27 * \left[\log(R_f)\right] + 0.36 * \left[\log\left(\frac{q_t}{p_a}\right)\right] + 1.236 \quad \textbf{(2.2)}$$

where:

γ = soil unit weight

γ_w = unit weight of water (same unit as γ)

p_a = atmospheric pressure (same unit as q_t) = 100 kPa

With an estimation about γ and knowing or assuming the GWT, one can determine the vertical total and effective stresses. The normalized cone resistance Q_{tn}, normalized friction ratio F_r and the Soil Behavior Type Index I_C are calculated using equations 2.3-2.5:

$$Q_{tn} = \left(\frac{q_t - \sigma_{vo}}{p_a}\right) * \left(\frac{p_a}{\sigma'_{vo}}\right)^n \quad \textbf{(2.3)}$$

$$F_r = 100 * \left(\frac{f_s}{q_t - \sigma_{vo}}\right) \quad \textbf{(2.4)}$$

$$I_C = \sqrt{[3.47 - \log(Q_{tn})]^2 + [\log(F_r) + 1.22]^2} \quad \textbf{(2.5)}$$

where n is the variable stress exponent.

From equation 2.3-2.5 and the contours of I_C in Figure 2.5, one can see that the I_C is sensitive to changes in q_t and any problems in accuracy of the I_C is mainly controlled by the accuracy in q_t. In order to solve this, Zhang et al. (2002) introduced a variable stress component. Various studies have been done about the appropriate stress normalization and it turns out that for clean sand regions in the SBT_n chart $n \approx 0.5$ and for clay regions $n \approx 1$. However, that is a general rule and the variable stress exponent can vary widely depending on the type of soil and the vertical stresses. Based on these considerations, a formula was created that would allow a variation of the variable stress exponent. The variable stress component can be estimated using the formula:

$$n = 0.381 * I_C + 0.05 * \left(\frac{\sigma'_{vo}}{p_a}\right) - 0.15 \quad \textbf{(2.6)}$$

where $n \leq 1$.

As one can see, the variable stress component is a function of I_C which is a function of Q_{tn} and that parameter is again dependent on the variable stress component. So in order to determine the soil type, a number of iterations will be needed.

For an accurate depiction of the soil profile, borehole measurements are preferred as they give the *measured* soil profile and not an estimation. This would mean that the generated soil profile might not necessarily match with the measured soil profile from a borehole measurement. Also, the SBT_n method only identifies the soil type (e.g. sand) however it does not give more information about the soil type itself (e.g. loose or dense sand). As such you can have distinct regions of high and somewhat lower cone resistances in a sand layer but the SBT_n method will classify both as sand. The distinct regions would only be observed by looking at the cone resistance data or by computing the relative density. Nevertheless, it is still the most reliable method that is used to estimate the soil layers from a CPT soundings.

As for accurately determining the layer top and layer bottom, it is influenced by the sensing and development distance. Robertson (2009) notes that earlier investigations show that the sensing and development distance can be up to 15 cone diameters. The earlier investigations also determined that the size of this zone of influence decreases with increasing stresses. In order to identify the transition zone from sand to clay and vice-versa, the rate of change of I_C can be used. Robertson (2009) suggests that the cone transitions from a sand-like to clay-like soil or vice-versa when the I_C is changing rapidly and when it is crossing the boundary defined by I_C = 2.6. By removing the identified transition zones, one would get an accurate depiction of the soil layer.

2.3. Probabilistic design method

The purpose of probabilistic design is according to Jonkman et al. (2015) to create a design with an acceptable risk level in an optimal way. So one would usually come up with a safety level or a target value for reliability as a requirement for the design of a structure.

Thus, the first step in probabilistic design would be to derive the target value for reliability which is expressed as a failure probability or reliability index β. The target value depends on the reference period of the structure and whether it needs to be distributed over a system of

multiple elements with multiple failure mechanisms. The failure probability or reliability index is calculated in a reliability analysis. Regardless whether it is fully deterministic, semi-probabilistic or fully probabilistic, the reliability analysis uses the limit state Z and the limit state function $g(\underline{X})$ which are defined as:

$$Z = R - S \tag{2.7}$$

$$g(\underline{X}) = Z \tag{2.8}$$

where:

R = resistance variable

S = load variable

$g(\underline{X})$ = limit state function

$\underline{X}$ = vector which contains n basic variables (e.g. load, resistance, model uncertainty)

The limit state is the condition in which the structure can no longer perform and fulfill its requirements. From the limit state function the design point can be found which is the point where failure is most probable, thus where $g(\underline{X}) = 0$ with the highest probability density.

For pile designs, characteristic values and partial safety factors are used for the reliability analysis. For example, the Koppejan method, which is used in Dutch pile designs, uses partial factors that are dependent on the material, the construction method and the pile geometry.

Eurocode 7 which is the European standard for geotechnical designs makes use of characteristic values for the soil parameters in order to take into account the spatial variability of the soil. However, no particular guidance is given in how to calculate those characteristic values. As such, several approaches have been proposed. For example, Hicks and Samy (2002b) showed how the characteristic values could be computed by using a random finite element method (RFEM), a reliability based approach which can be classified as a level III method and Varkey et al. (2020) made a comparison between the simpler approaches and the RFEM approach for characteristic values of shear strength properties for dike stability.

As for level III methods, many papers have been written about probabilistic models for spatial variability (e.g. Cami et al., 2020; Fenton, 1999; Nadim, 2015; Nie et al., 2015) and where the RFEM approach, a level III method was used in a reliability analysis as part of their research (e.g. Hicks, 2014; Hicks & Samy, 2002a, 2002b; Varkey et al., 2020).

This chapter will briefly explain Level III methods which are fully probabilistic methods. Information about the other reliability methods can be found in Appendix A.

Level III methods (general probabilistic methods)

The level III methods are numerical methods where the variables are modelled by their joint distribution functions. In level III methods, the variables do not need to be normally distributed but as the methods are fully probabilistic, the computation effort of these methods increases. The level III methods evaluate the integral:

$$P_f = \int_{g(\underline{X})<0} f_X(\underline{x}) d\underline{x} \tag{2.9}$$

where $f_X(\underline{x})$ is the joint probability density function of the basic variables. The integral is solved by calculating exactly through i.e. (numerical) integration or Monte Carlo simulations.

More often than not, the Monte Carlo simulations are chosen. The choice of the Monte Carlo (MC) approach is often based on practical considerations as numerical integrations become more intensive if there are more than 2 stochastic variables involved in the calculations. The MC approach is simply generating a random sample for each stochastic variable from their respective probability distributions and record whether the structure fails or not. This simulation is repeated N times and at the end you have a counter N_f which counts the number of times the structure has failed in the N simulations. From that, the estimated probability of failure $\hat{P}_f$ is defined as:

$$\hat{P}_f = \frac{N_f}{N} = \frac{1}{N}\sum_{j=1}^{N} I\left[g\left(\underline{X}\right) < 0\right] \quad \textbf{(2.10)}$$

where $I[...]$ is an indicator function which gives 1 if the argument in the function is true and 0 when it is false.

The use of level III methods are realized by using probabilistic models to characterize the basic variables. A finite element model of the problem (e.g. a dike for slope stability) is created and based on the probabilistic models a random field is generated and projected onto the finite element mesh of the finite element model. After which MC simulations can be performed with each simulation generating a new random field.

2.4. Soil variability

For the design of a hydraulic or geotechnical structure, the subsurface plays an important role for foundation calculations or for failure mechanisms like slope stability, erosion, piping and micro-stability. Typically the subsurface is modelled as different homogeneous soil layers stacked on top of each other and within the soil layer the soil properties are considered to be constant. However in reality the soil properties within the subsoil are often heterogeneous and spatially variable. The characterization of the variability of soil properties is necessary in order to create a model which reflects the real subsoil. However, there is never enough data for a model to perfectly reflect reality as a model is by definition a simplified form of reality. As such the characterization of soil variability also brings out the soil uncertainty.

The level of soil variability that is included in a design depends on the approach. The deterministic approach does not include soil variability which leads to a single representative value of a soil property. The uncertainty-based approach includes the soil variability which means that the soil uncertainty is quantified as well. This leads to a more realistic subsoil model and the analysis leads to the performance of a geotechnical structure in terms of probabilities of failure. This approach would lead to a more economical design.

The terms “soil variability” and “soil uncertainty” are often used interchangeably and the two concepts are closely related to each other. However, they are not the same thing. *Variability* is defined as “an observable manifestation of heterogeneity of one or more physical parameters and/or processes” (Uzielli et al., 2006, p. 3) and “*uncertainty* reflects the decision (or necessity) to recognize and address the observed variability in one or more soil properties of interest” (Uzielli et al., 2006, p. 3).

2.4.1. Soil heterogeneity

Soil heterogeneity is defined as “the spatial variability of soil properties” (Hicks, 2014) and depending on which scale you look at, it can be divided into three levels: “stratigraphic heterogeneity, lithological heterogeneity and inherent soil variability” (Uzielli et al., 2006).

At the large (regional) scale, there is the stratigraphic heterogeneity in which the subsoil is no longer seen as one homogenous layer but instead it is seen as a group of different geological soil layers like sand, clay and peat.

At the medium scale, there is the lithological heterogeneity which looks at the lithological classes present within a relatively uniform soil mass. An example of lithological heterogeneity is pockets of sand or silt within a clay layer. This is related to the weak and strong zones within a soil layer and it tells about the variability of soil properties within a single soil layer.

At the smallest scale, there is the inherent soil variability which is “the variation of properties from one spatial location to another inside a soil mass which could be regarded as being significantly homogeneous for geotechnical purposes” (Uzielli et al., 2006). In other words, this scale relates to the variability of the soil properties of a soil type like sand, clay or peat. The smallest scale in this case refers to the scale measurable by common geotechnical testing.

The soil heterogeneity is relevant for the engineering process regardless of the scale. The stratigraphic heterogeneity is important in the preliminary design phase for characterizing the subsoil; the lithological heterogeneity is important for modelling the soil variability of the soil layers and getting the design value of a parameter; the inherent soil variability can be analyzed in order to get the soil properties of a soil type and with that information a more economic design can be achieved.

For an uncertainty-based approach, the soil heterogeneity can be characterized by its statistics. The statistical parameters can be determined through a stochastic analysis and they are the mean μ, standard deviation σ and the scale of fluctuation θ. The first two parameters are the point statistics that describe the probability density function of a soil property while the last one is the spatial statistic that describes the correlation structure of the soil property and thus the fluctuations of the soil property around the mean. An example of a soil property $X(z)$ and its statistics is shown in Figure 2.6.

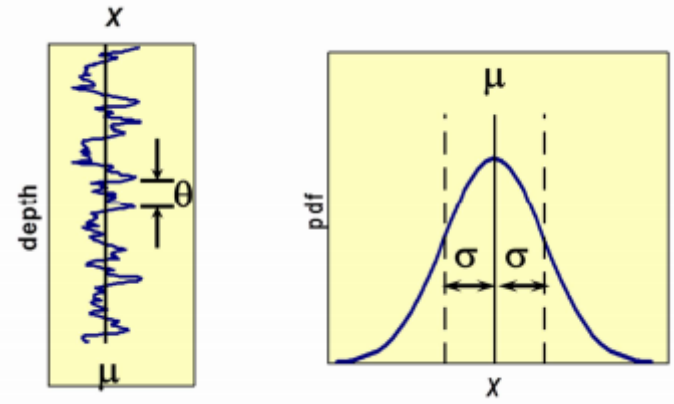

Figure 2.6: Soil property *X* as a function of depth (left) and its statistics (right) as a normal distribution with mean μ and standard deviation σ. Source: Hicks (2014)

2.4.2. Determining the point statistics

The point statistics of soil property $X(z)$ as a function of depth, can be determined through a stochastic analysis. For each soil layer, the trend in the soil data is being identified and then removed from the soil data. The detrended soil data is stationary and it can be considered to be a stationary random process. The point statistics can be determined as they are the mean of the trend $\mu(z)$ and the standard deviation of the trend $\sigma(z)$. From that a coefficient of

variation $c_v \left(= \frac{\sigma}{\mu}\right)$ can be calculated and the appropriate probability distribution model can be chosen.

The choice of the probability distribution is dependent on the person performing the stochastic analysis, the site itself and the soil property. The site is an important factor to take into account as the soil is spatially variable. Fitting the probability distribution for a soil property at the site does not mean that the soil around the site shares the same distribution or parameter values.

Thus there is no best fitted distribution for a soil property. However there have been investigations about choosing an appropriate distribution for soil properties. Popescu et al. (1998) investigated and saw that the soil strength in shallow layers had distributions that were positively skewed while in the deeper layers the distribution became more symmetrical. Corotis et al. (1975) tried to see whether it was possible to use only the lognormal (LN) distribution and normal (N) distribution for the soil properties and Lacasse and Nadim (1996) essentially made a review of the probability distribution choices that were made for some soil properties and the results are shown in Table 2.3.

Soil property	Soil type	Distribution
Cone resistance	Sand	LN
	Clay	N/LN
Undrained shear strength	Clay (triaxial tests)	LN
	Clay (index tests)	LN
	Clayey silt	N
Stress-normalized undrained shear strength	Clay	N/LN
Plastic limit	Clay	N
Submerged unit weight	All soils	N
Friction angle	Sand	N
Void ratio, Porosity	All soils	N
Overconsolidation ratio	Clay	N/LN

Table 2.3: Probability distributions for different soil properties. Source: Uzielli et al. (2006) (adapted from Lacasse and Nadim (1996))

The results shows that the soil properties were mainly modelled as a lognormal distribution or as a normal distribution. For the purpose of this research, only the lognormal and normal distribution will be taken into consideration for choosing a probability distribution of a soil property.

2.4.3. Spatial variability

The spatial variability is when a property shows different values when measured at different spatial locations. This spatial variability is a characteristic of all soil bodies and geotechnical parameters like soil strength, friction angle, cohesion and permeability are all spatially variable. This leads to uncertainties in the design of geotechnical structures. Currently, the practice is to get a characteristic value for the geotechnical parameter and use it for the design to get a single factor of safety.

In order to take into account the uncertainty, the spatial variability needs to be quantified. The most commonly used parameter to characterize the spatial variability is the scale of fluctuation (SF) that was introduced by Vanmarcke (1977). The scale of fluctuation is defined as the distance over which soil property values are significantly correlated and it is sometimes referred to as the spatial correlation distance. With this definition a lower SF means that a soil property is more spatially variable.

There is also another parameter to describe the spatial variability and that is the vertical variability index (VVI) and the horizontal variability index (HVI). Salgado et al. (2019)

proposed these parameters as part of a comprehensive methodology for site variability analysis using CPT data. The VVI "reflects variability in q_c, f_s, layering and other factors for each CPT sounding" (Salgado et al., 2019, p. 38) and thus looks at the whole soil profile. The HVI looks at how well correlated the q_c is across multiple CPT soundings and it only looks at a particular soil layer. Both parameters can be used to get a site variability rating (SVR) which is meant to be used as an easy-to-use indicator for site variability when one is planning a site investigation.

2.5. Computing the spatial variability

Vanmarcke (1977) introduced the scale of fluctuation as a way to determine the spatial variability of a geotechnical parameter. Vanmarcke (1983) defined the SF, θ, as an integral of the autocorrelation function $\rho(\tau)$ with τ being the separation distance, the distance between points i and j $(\tau = |z_i - z_j|)$.

$$\theta = \int_{-\infty}^{\infty} \rho(\tau)\, d\tau = 2\int_{0}^{\infty} \rho(\tau)\, d\tau \qquad \textbf{(2.11)}$$

where:

θ = scale of fluctuation

$\rho(\tau)$ = autocorrelation function (ACF)

τ = separation distance

However the autocorrelation function is dependent on the available data and in geotechnical engineering the quantity of data is often limited. With the limited data only a sample ACF $\hat{\rho}(\tau)$ can be calculated and an ACF model needs to be fitted to the sample ACF in order to use the formula of Vanmarcke (1983).

In practice, the SF can be estimated from CPT data and various approaches have been proposed for estimating the SF. Among the approaches are: the simplified method, the autocorrelation fitting method (ACFM) and the semivariogram fitting method (SVFM).

Simplified method

The simplified method was proposed by Vanmarcke (1977) as a rule of thumb estimation and it can also be called the zero-crossing method. The method fits a trend line to the CPT data and then takes note of the number of intersections between the CPT data and the trend line. It averages the crossing distances, the distance between intersections and estimates the SF from that average. More information can be found in the papers of Vanmarcke (1977) and Zhu et al. (2019) who investigated the validity of this estimation method.

Autocorrelation fitting method

The ACFM is fitting an autocorrelation model which is a one parameter model, to the sample autocorrelation function. It originates from random field theory and time series analysis and the ACFM uses the same constraints as for time series analysis. Chapter 2.5.1 will explain the ACFM a bit further.

Semivariogram fitting method

The SVFM is fitting a semivariogram model which is a three parameter model, to the sample semivariogram function (SVF) and it originates from geostatistics. In essence, it conveys the same information as the ACF for stationary processes but the SVF has less stringent conditions than the ACF. However Uzielli et al. (2006) warned that unlike the SVF the ACF had Bartlett's limits that could be used to determine the reliability of its model parameter.

Cami et al., 2020; Onyejekwe et al. (2016); Uzielli et al. (2006) can be used to find more information about the SVFM.

In literature these approaches have been proposed for the *vertical* scale of fluctuation. This is because most site investigation methods like CPT and SPT only look in the vertical direction. As such the data that is being used, results in an estimate of the vertical scale of fluctuation.

The horizontal scale of fluctuation θ_h is usually computed by using a group of closely spaced CPT profiles and then the ACFM is used to get the θ_h value. However, it is more difficult to get an accurate SF in the horizontal direction than in the vertical direction as the vertical ACF is dependent on measurements taken every few centimeters while the horizontal ACF is dependent on the separation distance between CPTs which is in the order of meters. Ching et al. (2018) investigated how to estimate the horizontal SF using a limited amount of CPT and more information about horizontal SF can be found there.

In order to give context to the estimated scales of fluctuation, a summary from Zhang et al. (2021) is used which summarizes the values found in earlier literature. The part of the summary which contains the values for sand using CPT and CPTu methods are shown in Table 2.4. The table shows that the reported vertical scale of fluctuation for sand is around 0.07 – 3 m and the reported horizontal scale of fluctuation is around 3 – 2000 m.

Reference	Scale of fluctuation (m)		Soil type
	Vertical θ_v	Horizontal θ_h	
Kok-Kwang & Kulhawy, 1999	0.2 – 0.5	3 – 80	Sand, clay
Uzielli et al., 2005	0.13 – 1.11	-	Sand, clay
Liu & Chen, 2010	1.72 – 2.53	66 - 1546	Sand, clay, silt
	0.18 – 1.94	62 – 2000	Sand, clay, silt
Eslami Kenarsari et al., 2013	0.36 – 2.44	-	Sand
Kim & Salgado, 2013	2.2 – 3.0	35 - 75	Sand
Bombasaro & Kasper, 2016	0.07 – 0.78	12.15 – 16.11	Sand, clay
Bouayad, 2017	0.32 – 1.32	-	Sand

Table 2.4: Adapted summary of scales of fluctuation reported in the literature. Source: Zhang et al. (2021)

2.5.1. Scale of fluctuation: autocorrelation fitting method

The ACFM uses the method of moments. The method of moments makes use of the empirical statistical moments of a dataset (e.g. the first statistical moment is the mean, the second moment is variance, etc.). They are empirically derived from the dataset without any assumptions and the empirical moments are equal to the theoretical moments. Thus one does not need to make any assumption about which probability distribution fits the data the best. However the dataset does need to be sufficiently large enough as small datasets will lead to a biased estimation of the statistical moments.

For a soil property $X(z)$ the measurements are taken at (constant) depth intervals so the corresponding CPT data is discrete. The soil property $X(z)$ is generally described by the equation below as the sum of a trend function $T(z)$ and a random fluctuation function $\varepsilon(z)$.

As the ACFM is derived from time series analysis, the assumption that the residuals need to be stationary must be fulfilled. As such, a test for stationarity needs to be performed. If the residuals are indeed stationary, one can use the stationary residuals in order to derive the point statistics and model the random fluctuation function that is described by a probability distribution.

$$X_i = X(z_i) = T(z_i) + \varepsilon(z_i), \qquad i = 1, \dots, N \tag{2.12}$$

where:
$X(z_i)$ = soil property at location z_i

$T(z_i)$ = trend function at location z_i

$\varepsilon(z_i)$ = random fluctuation function at location z_i

z_i = vertical depth

N = total number of datapoints

The ACF describes the spatial correlation structure of $\varepsilon(z)$ but due to the CPT data being limited in size, the real ACF cannot be calculated. As such one is dependent on the sample ACF $\hat{\rho}(\tau)$ which is an approximation of the real ACF based on the available information. There are two types of formulae from which to calculate the sample ACF. The sample ACF is usually defined as:

$$\hat{\rho}(\tau_k) = \frac{C(\tau_k)}{C(0)} \quad \textbf{(2.13)}$$

with $C(\tau_k)$ being the autocovariance function of $\varepsilon(z)$ at separation distance τ_k and $C(0)$ being the variance of $\varepsilon(z)$. Cami et al. (2020); Fenton (1999); Onyejekwe et al. (2016) use in their respective research the formula in which the variance is a biased estimator while Nie et al. (2015) use an unbiased estimator. The difference between an unbiased variance estimator and a biased variance estimator is that: (1) the unbiased estimator can have negative eigenvalues in the covariance and correlation matrix which can lead to negative variances and (2) according to Fenton (1999) the biased estimator has a slightly smaller expected error variance than the unbiased case.

For the discrete dataset the following formula was used in which the biased variance estimator is used:

$$\hat{\rho}(\tau_k) = \frac{\sum_{i=1}^{N-|k|}[\varepsilon(z_i) - \mu]\left[\varepsilon\left(z_{i+|k|}\right) - \mu\right]}{\sum_{i=1}^{N}[\varepsilon(z_i) - \mu]^2} \quad \textbf{(2.14)}$$

where:
$\hat{\rho}(\tau_k)$ = sample ACF

μ = mean of $\varepsilon(z)$

τ_k = separation distance $k\Delta z$ where Δz is the (constant) sampling interval

k = lag where $k = 1,2,3, \ldots$

For the ACFM the maximum number of lags is $k = \frac{N}{4}$ as “the data for calculating $\hat{\rho}(\tau)$ are considered insufficient for obtaining a reliable estimate of the SF when τ exceeds the distance of a quarter of the sampling space domain” (Nie et al., 2015).

The SF is determined by simply fitting the best theoretical autocorrelation model to the sample ACF as the SF is a constant in the ACF of that model. There are many autocorrelation models from which one can choose from such as the triangular model, exponential model and many more as shown in Table 2.5 and Figure 2.7. The choice of the best theoretical model is by fitting the numerous models to the sample ACF and then choose based on the ordinary least squares (OLS) approach.

Autocorrelation model	Correlation function as a function of separation distance τ
Single exponential (SNX)	$\rho(\tau) = \exp\left\{-\frac{2\lvert\tau\rvert}{\theta}\right\}$
Second-order Markov (SMK)	$\rho(\tau) = \left(1+\frac{4\lvert\tau\rvert}{\theta}\right)\exp\left\{-\frac{4\lvert\tau\rvert}{\theta}\right\}$
Third-order Markov (TMK)	$\rho(\tau) = \left(1+\frac{16\lvert\tau\rvert}{3\theta}+\frac{256}{27}\left(\frac{\lvert\tau\rvert}{\theta}\right)^2\right)\exp\left\{-\frac{16\lvert\tau\rvert}{3\theta}\right\}$
Squared exponential (SQX)	$\rho(\tau) = \exp\left\{-\pi\left(\frac{\lvert\tau\rvert}{\theta}\right)^2\right\}$
Spherical	$\rho(\tau) = \begin{cases}\frac{4}{3}-2\left\lvert\frac{\tau}{\theta}\right\rvert+\frac{2}{3}\left\lvert\frac{\tau}{\theta}\right\rvert^3, & \lvert\tau\rvert \le \theta \\ 0, & \text{otherwise}\end{cases}$
Cosine exponential (CSX)	$\rho(\tau) = \exp\left\{-\frac{\lvert\tau\rvert}{\theta}\right\}\cos\left\{-\frac{\lvert\tau\rvert}{\theta}\right\}$
Triangular	$\rho(\tau) = \begin{cases}1-\frac{\lvert\tau\rvert}{\theta}, & \lvert\tau\rvert \le \theta \\ 0, & \text{otherwise}\end{cases}$

Table 2.5: Theoretical autocorrelation models as a function of the separation distance τ. Source: Cami et al. (2020)

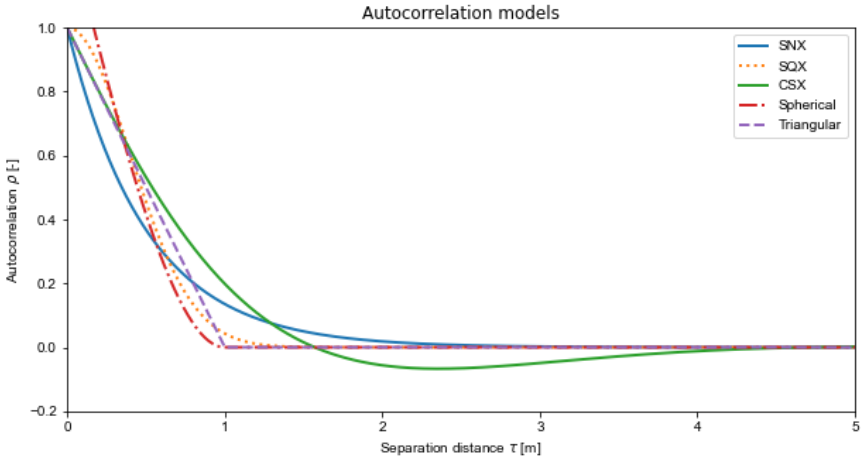

Figure 2.7: Autocorrelation models for a vertical scale of fluctuation of 1 m.

Another way to calculate the SF from the sample ACF is via the Bartlett's limit (I_B). Fenton (1999) has shown that the reliability of the sample ACF drops with increasing separation distance and that in short-scale processes wherein $\theta \ll \tau$ the sample ACF becomes a good estimator. The Bartlett's limit approach is not model dependent, it only requires the sample ACF and it focuses on the short scale process. The SF is equal to the separation distance at which the sample ACF intersects with the Bartlett's limit. The Bartlett's limit is defined as:

$$I_B = \frac{1.96}{\sqrt{N}} \tag{2.15}$$

where N is the total number of datapoints.

2.6. Random fields

In geotechnical engineering, the use of random fields and in particular stationary random fields, has been increasing over the years as a way to model the spatial variability of the subsoil and spatially variable properties in engineering systems in general.

There are many different algorithms to generate random fields and in the literature many papers can be found about this subject in which algorithms are being introduced, improved or evaluated (e.g. Abrahamsen et al., 2018; Fenton & Vanmarcke, 1990; Fenton, 1994; Li et al., 2019; Ravalec et al., 2000). This thesis will look at three algorithms that are commonly used to generate random fields:

1. Covariance matrix decomposition method (CMD).
2. Fast Fourier transform moving average method (FFT-MA).
3. Local average subdivision (LAS).

2.6.1. Covariance matrix decomposition

The covariance matrix decomposition method is a direct way to produce a random field with n locations in space and a known covariance matrix $\boldsymbol{C}$. For a standard normal random field $\boldsymbol{X}$, the following formulae are used to produce it:

$$\boldsymbol{C} = \boldsymbol{L}\boldsymbol{L}^{\mathrm{T}} \tag{2.16}$$

$$\boldsymbol{X} = \boldsymbol{L}\boldsymbol{W} \tag{2.17}$$

where $\boldsymbol{W} = n \times 1$ standard normal vector and $\boldsymbol{L} = n \times \mathrm{n}$ is the decomposition matrix that is obtained through the Cholesky decomposition or eigen-decomposition. An equiprobability transformation can be used to transform $\boldsymbol{X}$ into a non-normal random field.

The appeal of the covariance matrix decomposition lies in its simplicity and accuracy. However, Li et al. (2019), Fenton and Griffiths (2008) and Fenton (1994) note that the main drawback of this method is that it is only useful for small fields as the decomposition would be too time-consuming for large fields with large covariance matrices and it would be prone to round-off errors. Fenton and Griffiths (2008) elaborate that the round-off errors are a result of covariance matrices being often poorly conditioned and Li et al. (2019) told an example that a simulation of a 3D random field with $n = 20 \times 20 \times 40$ would use almost all memory space of a 16 GB RAM desktop computer. This is a result of the Cholesky decomposition and random field realization requiring O(n^3) and O(n^2) floating point operations. Ravalec et al. (2000) in particular note that the practical limit for the Cholesky decomposition is $n = 1000$. So the CMD can be considered to be only useful for 1D random fields and for very small 2D and 3D random fields.

2.6.2. Fast Fourier transform moving average

The fast Fourier transform moving average method (FFT-MA) is a combination of the fast Fourier transform (FFT) method with the moving average method.

The original moving average method was made with the intention to simulate random Gaussian fields with stationary covariances. The method was similar to the Cholesky decomposition but instead of decomposing a large covariance matrix, “the covariance function is expressed as a convolution product of the function g and its transpose” (Ravalec et al., 2000, p. 702). Ravalec et al. (2000) combined the moving average method with the FFT algorithm and as the computations are done with FFT algorithm, the simulations are fast and stable.

Because of the implied periodicity of the Fourier transform, the random field needs to be oversized from the desired N locations in space and sampling rate dx to size $N_1 = Ndx + \theta$ and sampling rate dx_1. After the computation, the additional points can be discarded. The reason for the equally spaced grids is that the FFT method “produces stochastic processes having any kind of stationary covariance function, but only for equal-spaced gridding”

(Ravalec et al., 2000, p. 702). Thus in order to use the FFT-MA method, the condition of an equally spaced grid is necessary.

The formulae for the generation of a 1D Gaussian random field $\boldsymbol{X}$ with N_1 locations in space, mean m and covariance function $\boldsymbol{C}$ are:

$$\boldsymbol{C} = g * g^{\mathrm{T}} \tag{2.18}$$

$$\boldsymbol{X} = m + g * z \tag{2.19}$$

$$S = \mathcal{F}(\boldsymbol{C}); G = \sqrt{dx_1 * S}; Z = \mathcal{F}(z); \tag{2.20}$$

$$g * z = \mathrm{Re}\left(\mathcal{F}^{-1}(G * Z)\right) \tag{2.21}$$

with z being a vector of N_1 uncorrelated normal deviates and $\mathcal{F}(\dots)$ and $\mathcal{F}^{-1}(\dots)$ being the Fourier and inverse Fourier transform.

For the covariance function $\boldsymbol{C}$, a covariance sequence such as the one in Figure 2.8 needs to be constructed so that the discrete power spectrum S can be real and even.

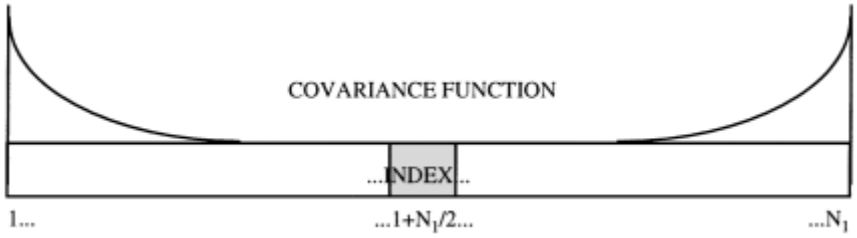

Figure 2.8: Sketch of the covariance sequence for a 1D case. Source: Ravalec et al. (2000)

Thus, the conclusion that Ravalec et al. (2000) made was that the FFT-MA is fast for unconditional realizations and that random numbers such as the normal deviates can be uncoupled from parameters such as the scale of fluctuation. In other words, one can use the same realization of normal deviates for different scales of fluctuation. As for the oversizing of the random field, Abrahamsen et al. (2018) investigated how large the oversized field needs to be and they developed a method to determine that.

2.6.3. Local average subdivision

The local average subdivision is a method introduced by Fenton and Vanmarcke (1990) that would allow engineering properties to be represented as local averages while also allowing to incorporate real data or change the resolutions within the sub-regions. The method also had the advantage of being ideal for finite element modeling.

The LAS makes use of a top-down approach, as shown in Figure 2.9 for the construction of the one-dimensional local average process. At stage 0, the normally distributed global average Z_1^0 is generated with mean zero and variance obtained from local averaging theory. For stage 1, the domain of interest D is subdivided into two cells with two normally distributed values Z_1^1 and Z_2^1. The average of the pair must preserve the parent value so:

$$Z_1^0 = \frac{1}{2}(Z_1^1 + Z_2^1) \tag{2.22}$$

This way the global average remains constant throughout the subdivision and upwards averaging is preserved.

For each subdivision, only one cell value needs to be computed while the other cell is meant to preserve upwards averaging. The computation of the cell value is determined by

the parent cell and its neighbors. As an example, Z_4^3 is the weighted average of Z_2^2, Z_3^2, Z_1^2 and random noise ε and Z_3^3 is calculated such that upwards averaging is preserved so the formulae used are:

$$Z_4^3 = \alpha_1 Z_1^2 + \alpha_2 Z_2^2 + \alpha_3 Z_3^2 + \varepsilon \quad \textbf{(2.23)}$$

$$Z_3^3 = 2Z_2^2 - Z_4^3 \quad \textbf{(2.24)}$$

with α_1, α_2 and α_3 being the weights for the parent cell and its neighbors.

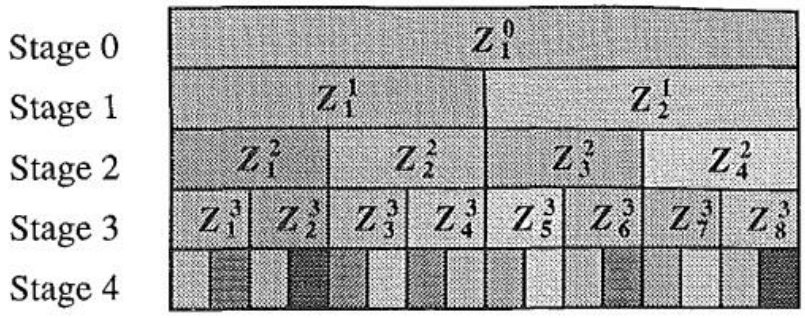

Figure 2.9: Top-down approach for the construction of a 1D local average subdivision process. Source: Fenton and Vanmarcke (1990)

2.7. Pile behavior

A common structure in ports are quay walls. A quay wall is an earth retaining structure at which ships can berth. The quay wall is supported by foundation piles and a spatial variability assessment and a pile load assessment are necessary for the optimal design of those foundation piles. The spatial variability assessment is necessary for the probabilistic design of foundation piles using the Monte Carlo approach. With the spatial variability being known, q_c profiles are simulated from which pile capacities are computed. The pile load assessment measures the pile capacity and it is necessary for comparing the computed pile capacity with the measured pile capacity. Using the comparison the computed pile capacity can be calibrated with an α factor.

The pile capacity is the capacity of the soil to resist the load from the foundation pile that is applied to the soil. The pile capacity Q_T is the sum of the pile shaft capacity Q_s and the pile base capacity Q_b. The pile shaft capacity Q_s is the maximum friction force between the soil and the pile shaft. Factors like negative skin friction that negatively impact the pile shaft capacity, are not taken into account. The pile base capacity Q_b is the maximum resistance force of the soil against the pile tip.

The Dutch pile design method computes the pile shaft capacity by integrating q_c over the length of the pile and multiply it with the circumference of the pile and the reduction factor α_s. The pile base capacity is computed by first calculating the average q_c around the pile tip with a CPT-based averaging technique and then multiply it with a reduction factors α_p. The CPT-based averaging technique in the Dutch standard for geotechnical design NEN-EN 1997-1 is the Koppejan method from Van Mierlo and Koppejan (1952) but there are also other averaging techniques with their own reduction factors like the LCPC method from Bustamante and Gianeselli (1982) and de Boorder (2019) with his alternative method.

For the pile base capacity, the location of the pile tip in a multi-layered soil is important due to the sensing and development distances that can affect the reliability of the measured q_c values of a CPT.

Besides the averaging technique, the spatial variability and the c_v of the soil property also influence the pile design. Cai et al. (2021) have shown that the ratio between θ_h and the pile diameter, and c_v of the soil property influence the accuracy of pile capacity estimations when using a single CPT at the center of the pile. Jaksa et al. (1996) have shown that the spatial variability has a considerable influence on the pile design but using the LCPC method has substantially lowered the influence of the spatial variability on the pile design.

Koppejan method

The Koppejan method is a CPT-based method using an averaging technique to calculate the average cone resistance around the pile tip $q_{c,avg}$. It was developed in the 1950s by Koppejan as one of the earliest CPT-based methods and it is widely used in the Netherlands.

Koppejan assumed that the failure planes around the pile tip would be as in Prandtl's theory and have the shape of a logarithmic spiral as seen in Figure 2.10(a). The spiral is used to determine the influence zone that would affect the pile capacity. Koppejan believed the influence zone to be 0.7-4D below the pile tip to 8D above the pile tip. For the equation below, Koppejan made several assumptions:

- The logarithmic spiral is divided in three parts (I, II, III) as shown in Figure 2.10(b).
- The combined contributions of part I and II to q_b equal the contribution of part III.
- Parts II and III follow the minimum path rule as the failure planes follow the path of least resistance.

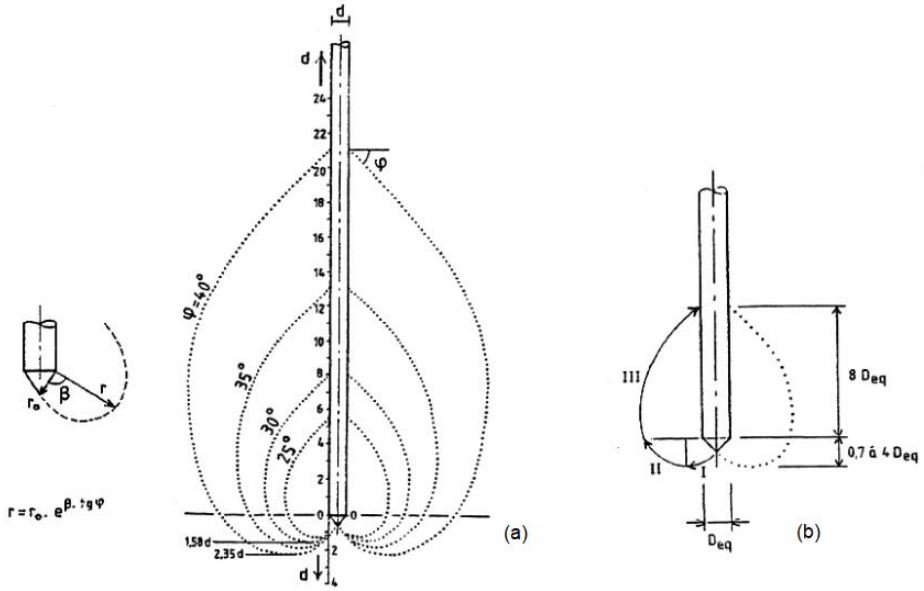

Figure 2.10: (a) Logarithmic spirals as failure planes when pile tip fails and (b) the schematization of the three parts of the logarithmic spiral. Source: Tol (2006)

$$q_{c,avg} = \frac{1}{2}\left(\frac{q_{c,I,avg} + q_{c,II,avg}}{2} + q_{c,III,avg}\right) \quad \textbf{(2.25)}$$

where:

$q_{c,I,avg}$ = the arithmetic average of the q_c values below the pile tip over a depth which may vary between 0.7D and 4D

$q_{c,II,avg}$ = the arithmetic average of the q_c values below the pile tip following a minimum path rule below the pile tip over the same depth of 0.7 to 4D.

$q_{c,III,avg}$ = the arithmetic average of the q_c values following a minimum path rule recorded above the pile tip over a height of 8D.

The Normcommissie-351-006-Geotechniek (2019) set the upper limit of the unit bearing capacity $q_b(= \alpha_p * q_{c,avg})$ at 15 MPa. Tol (2006) mentioned this as a result of experimental loads done in the Netherlands and measuring the unit bearing capacity only up to 15 MPa. This upper limit was for all cohesionless soils like sand and gravel. Another thing that was added, were the reduction factors α_p, β and s that needed to be multiplied to $q_{c,avg}$. The pile reduction factor α_p is 0.7 for driven piles in sand, the pile base reduction factor β is 1 if the pile base has the same diameter as the pile shaft and the β reduces for a wider pile base. The shape factor s equals 1 if the pile is square or circular and it reduces for more rectangular pile bases.

Due to the minimum path rule, the Koppejan gives out a conservative estimate and it is also quite sensitive to any low q_c measurements in its influence zone. Also it gives a constant α_p value regardless whether it is an open-ended or closed-ended pile which is quite significant for the eventual calculations of the pile base capacity.

LCPC method

As an alternative to the Koppejan method, there is also the LCPC method or French method for calculating the $q_{c,avg}$. First, the q_c values from the zone, 1.5D above and 1.5D below the pile tip, are used and the mean value $q_{c,mean}$ is calculated. Then, the values below $0.7q_{c,mean}$ and above $1.3q_{c,mean}$ are filtered out. The $q_{c,avg}$ is then calculated as the mean of the remaining q_c values. The explanation is illustrated in Figure 2.11.

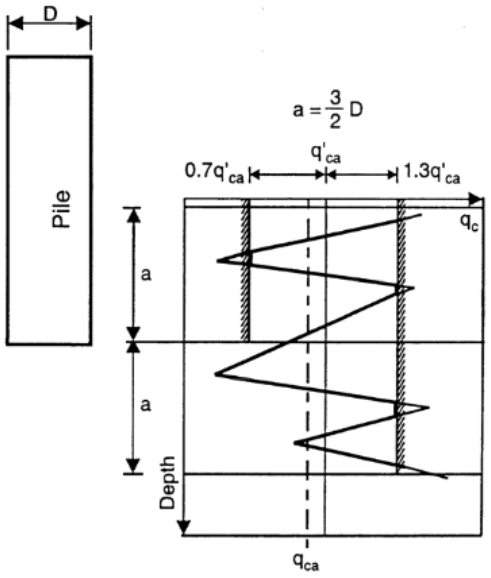

Figure 2.11: Calculation of the average cone resistance around the pile tip $q_{c,mean}$ according to the LCPC method. Source: Robertson and Cabal (2015)

This method is not as sensitive to extreme measurement values as the Koppejan method if the q_c profile has a high coefficient of variation or a high vertical scale of fluctuation. In a study of CPT-based methods, Rollins et al. (1999) compared four different methods (including the LCPC method) to axial pile load test results. Unlike the original from Bustamante and Gianeselli (1982), the zone of influence was extended to 4D above and below the pile tip. The result was that the calculated end bearing capacity of the LCPC method came closest to the measured end bearing capacity. The estimations were within 11% of the measured capacity while the other methods overestimated it by 60 to 80%. The LCPC method also had the lowest standard error of the methods.

In a more recent study of Amirmojahedi and Abu-Farsakh (2019), a comparison was made between 18 different CPT-based methods and the ultimate load capacity of 80 concrete square piles. Using different evaluation methods, the LCPC is ranked in the top three and was ranked overall to be the best method compared to the other CPT-based methods.

de Boorder method

The de Boorder method is an averaging method which gives two weights to every q_c value in the averaging domain. The weights aspect was adapted from the Boulanger-de Jong method while the averaging domain aspect was adapted from the Koppejan and LCPC method.

The first weight is on the distance from the pile tip with the weight decreasing as one moves away from the pile tip. This makes the q_c values near the pile tip have a stronger influence on the $q_{c,avg}$ than the q_c values further away from the pile tip. The second weight is the q_c stiffness ratio from the Boulanger-de Jong method and the stiffness ratio is the q_c at the pile tip $q_{c,tip}$ divided by the q_c. de Boorder (2019) included the stiffness ratio because in the Boulanger-de Jong method it showed promising results in dealing with the sensing and development distances. More information about the weights and the averaging technique can be found in de Boorder (2019).

2.8. Geology in the Port of Rotterdam

Through the scale of fluctuation and I_C, one can simulate a CPT profile and estimate the soil layers from that simulation. However, one cannot measure the soil uncertainty from just the scale of fluctuation and soil layers. Other factors such as geological formations have to be taken into account as they affect the spatial variability of the soil and can help explain why within a single soil layer, the soil uncertainty can vary greatly or vary not at all. Viviescas et al. (2022) looked at the spatial variability of two geological formations using SPT N-values. The geological formations were mudflows which are formed from ancient landslides and residual soils which are formed from the weathering of in situ rock. Their conclusion was that residual soils had a lower spatial variability than mudflows because the weathering process occurred in situ with the formation. The mudflows had a higher spatial variability because of the mixing of soils with different degrees of weathering.

For the purpose of hydraulic and geotechnical structures, one only needs to focus on the shallow subsurface. The shallow subsurface is defined by Stafleu et al. (2012) as the subsurface up to a depth of 500 meters and Figure 2.12 describes the formations in the shallow subsurface in the Netherlands. In terms of geological time scale the shallow subsurface would refer to the subsurface belonging to the Quaternary and Neogene periods. This thesis will focus on a specific sand layer from the Pleistocene era and the geological formations that belong to that soil layer.

Geological layers in the Port of Rotterdam

From DINOloket, a website that maintains a database containing the geological data for shallow and deep geology in the Netherlands, one can get an cross-section of the estimated subsurface in the Port of Rotterdam using the GeoTOP subsurface model of Stafleu et al. (2012). The GeoTOP model is chosen as it provides the most information for the shallow subsurface and the foundations for hydraulic and geotechnical structures fall under the domain of the shallow subsurface. Information about DINOloket and other subsurface models can be found in Appendix B. Figure 2.13 shows the cross-section of the estimated subsurface in the PoR. The cross-section runs from the Maasvlakte to the Pernis and it follows the path of the Nieuwe Waterweg.

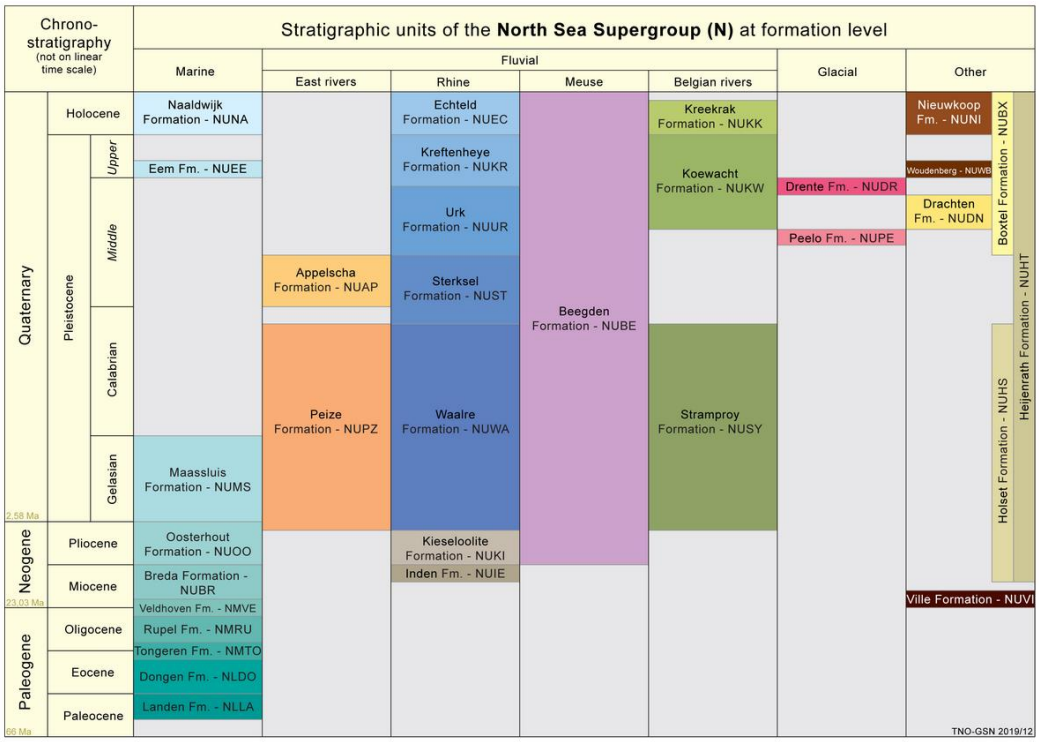

Figure 2.12: Diagram of all the formations of the Netherlands in the shallow subsurface. Source: Stafleu et al. (2012)

From Figure 2.13, one can see that there are 8 geological units in the Port of Rotterdam. The 8 geological units are:

- Anthropogenic deposits (AAOP)
- Naaldwijk Formation – Walcheren Member (ANAWA)
- Naaldwijk Formation – Wormer Member (NAWO)
- Echteld Formation (EC)
- Nieuwkoop Formation – Basisveen Bed (NIBA)
- Kreftenheye Formation – Wijchen Bed (KRWY)
- Kreftenheye and Boxtel Formation – Delwijnen Member (KRBXDE)
- Peize and Waalre Formation (PZWA).

This thesis will mainly focus on KRBXDE as it is the geological formation that is part of the Pleistocene sand that this thesis is looking at and it is the first thick sand layer that one encounters. For quay walls that are supported by foundation piles, the soft clay and peat layers can cause negative skin friction which will reduce the pile shaft capacity. Thus, the real pile capacity will be much lower than calculated one and it will therefore mostly rely on the pile base capacity. The base of the foundation pile will usually be around -25 to -30 m NAP as it is around that depth that the Pleistocene sand layer with high cone resistances and thus higher pile base capacities can be found. Information about the other formations can be found in Appendix B.

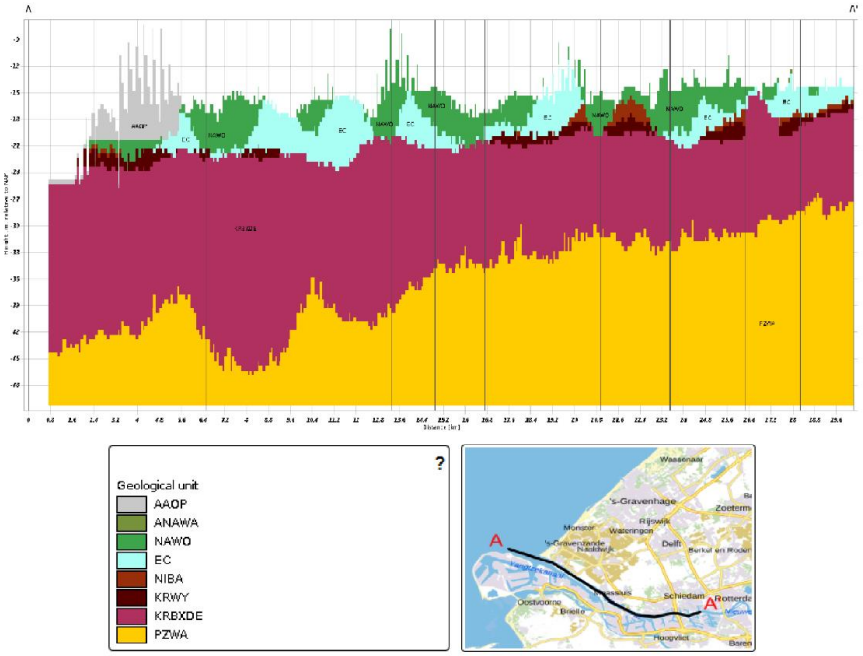

Figure 2.13: Cross-section of the estimated subsurface in the Port of Rotterdam using GeoTop model. Source: DINOloket

Kreftenheye and Boxtel Formation, Delwijnen Member

The Kreftenheye formation is from the late Pleistocene to early Holocene period and it is formed by the sediment deposits of the braided and meandering rivers like the Rhine and its precursors. So it falls under the fluvial domain. The formation consists of very fine to very coarse sands (63 – 2000 µm), fine to very coarse gravel (2 – 63 mm) and locally there can be some very thin peat layers.

The Boxtel Formation is from the Middle Pleistocene to Holocene period and it is formed from aeolian (drift sand, land- and river dunes) and fluvial deposits. It can be seen that the Boxtel Formation partially belongs to the fluvial domain. The formation consists of very fine to very coarse sand (105 – 420 µm), low to very sandy gravel, loam and thin peat. Dependent on its geographical location, the Boxtel Formation can be subdivided into: the Kootwijk Member, the Singraven Member, the Delwijnen Member, the Wierden Member, the Liempde Member, the Schimmert Member, the Tilligte Member and the Best Member.

Schokker et al. (2005) describe the Delwijnen Member contains the deposits of river dunes which are classified as part of the Kreftenheye Formation. As such the Delwijnen Member needs to be named with the Kreftenheye Formation. The Delwijnen Member consist of very fine to very coarse sand, thin loam layers and fine gravel.

2.9. Conclusion literature review

The first conclusion that can be made from the literature review is that there is not much if not any publicly available research on spatial variability across the Port of Rotterdam nor is there much research on spatial variability in the context of designing or evaluating present structures across the port. There are papers on spatial variability on offshore sites and in river estuaries but so far the author has yet to find a paper that investigated the spatial variability in a port area.

CPT data is often used to describe the spatial variability of soil properties of a specific soil layer. However in a multi-layered soil profile one has to take into account the transition zone between two soil layers which consists of the sensing distance and the development distance. Tehrani et al. (2018) investigated the effect of a layer interface on CPTs in layered sand. Based on their results, the sensing and development distances are of the order of 2.2–5.4 cone diameters. However, there is no theoretical or empirically derived equation to estimate the sensing and development distances. Any estimation would either have been derived empirically from lab experiments or it has to be taken from existing literature wherein the situation matches the setup described in the literature. When estimating soil layers with the SBT_n method, Robertson (2009) suggests to identify the transition zone by the rate of change of I_C and that the transition from a sand-like to clay-like soil or vice-versa happens when the I_C is changing rapidly and when it is crossing the boundary defined by I_C = 2.6.

As part of the SBT_n method the soil unit weight needs to be computed and that is mainly done with the formula of Robertson and Cabal (2010) which is derived for clays and sand having a saturated unit weight of at least 15 kN/m^3. Lengkeek et al. (2018) created an alternative formula for organic soils and peat. Their soil unit weight estimation formula can be used for the organic soils and peat that are found in Holocene sedimentary deposits in the Netherlands. However more assessments need to be carried out before the Lengkeek et al. (2018) formula is a viable option in Dutch geotechnical design methods.

The spatial variability can be characterized by the spatial statistic scale of fluctuation θ of a soil property. Both the autocorrelation method and the semivariogram method are used in spatial variability analysis but not many papers can be found which compares the performance of the two methods. One comparison was from Onyejekwe et al. (2016) using 7 CPTs and their result was that the semivariogram method gave a higher scale of fluctuation than the autocorrelation method but they could not explain if this was due to the methods or some statistical error. Literature seems to be fine with either methods as they are frequently used but according to Uzielli et al. (2006) the semivariogram model parameters are a bit more uncertain than the autocorrelation model parameters because unlike the autocorrelation method the semivariogram method has no parameter that could be used to determine the reliability of its model parameters.

In literature typical scale of fluctuation values for soil types can be found but there is little to no research on how the geology affects the spatial variability. Viviescas et al. (2022) researched that subject and concluded that the horizontal scale of fluctuation is influenced by the geology while the vertical scale of fluctuation is mainly influenced by vertical stresses but more research is needed. Also there is not much research on the spatial variability of geological members. This thesis partly goes into that subject as it investigates the spatial variability of sand belonging to the KRBXDE geological unit.

The predicted pile base capacity is influenced by the scale of fluctuation. Papers like Jaksa et al. (1996) and Cai et al. (2021) investigated that but they mainly looked at the influence of the horizontal scale of fluctuation when predicting the pile base capacity using

CPTs around the pile site. There is little to no research on the influence of the vertical scale of fluctuation when predicting the pile base capacity. This thesis investigates that influence.

The influence of the scale of fluctuation on the predicted pile base capacity comes from its on CPT-based averaging techniques (e.g. Koppejan, LCPC and de Boorder). There are many papers about the performance of averaging techniques except for the de Boorder which is a relatively new technique. There are few papers that look at the influence of spatial variability on the averaging techniques. Particularly, there are little to no research on the influence of spatial variability on the Koppejan and de Boorder methods.

The Koppejan method with a zone of influence 8 pile diameters (8D) above the pile tip to 0.7D-4D below the pile tip, makes use of the minimum path rule to give conservative estimates of the average cone resistance at the pile base. When given the hypothetical CPT profile of low scale of fluctuation with a high variance the minimum path rule reduces the influence of spatial variability. This is because once a low q_c value is found at depth z the high q_c values above that depth z are ignored due to the minimum path rule. Thus reducing the influence of variability of the soil above depth z. There is also the upper limit of the unit bearing capacity q_b at 15 MPa which reduces the variability of the predicted pile base capacity.

The LCPC method uses the influence zone of 1.5D above the pile tip to 1.5D below the pile tip. The q_c values from two zones, 1.5D above and 1.5D below the pile tip, are used and the mean cone resistance value is calculated. Then, the values below 0.7 and above 1.3 of the mean cone resistance in both zones, are filtered out. The average cone resistance is the mean of the remaining q_c values over the influence zone. When given the same hypothetical CPT profile of low scale of fluctuation with a high variance the LCPC method will give a higher average cone resistance than the Koppejan method. Like the Koppejan method the influence of spatial variability is reduced in the LCPC method by eliminating the q_c values below 0.7 and above 1.3 of the mean cone resistance.

Overall, the literature review shows that there is not much literature about the spatial variability in a port area. The scale of fluctuation is often discussed as part of evaluating its computation methods or the scale of fluctuation is discussed as in how the horizontal scale of fluctuation influences pile design. However, there is little to no literature on how geology influences the scale of fluctuation neither is there much literature about how the vertical scale of fluctuation influences pile design.

3. Methodology

This chapter will outline the methodology used in this thesis. Figure 3.1 presents a flow chart of the methodology.

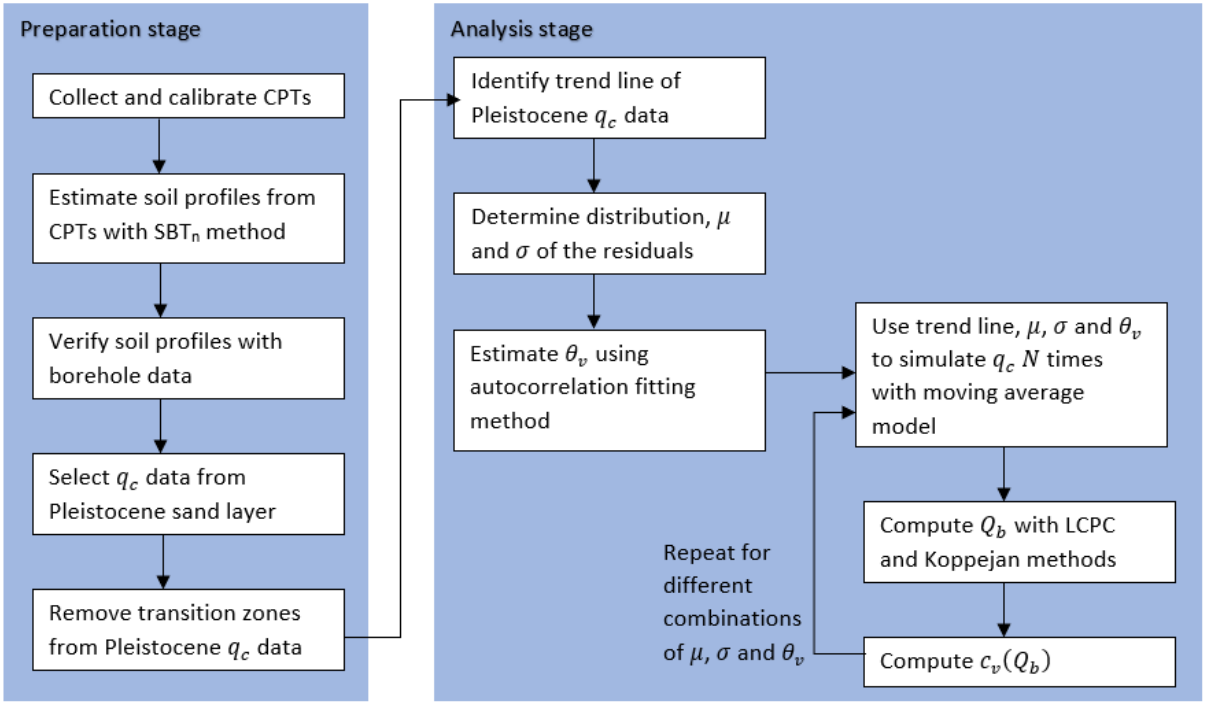

Figure 3.1: Flow chart of the methodology

3.1. Preparation stage

3.1.1. Data collection

The areas that will be looked at in this thesis are the shaded regions in Figure 3.2 where the Maasvlakte is light brown, the Botlek is dark green and Pernis is light blue. These areas are chosen to show the spatial variability along the river and because it takes too much time to analyze every single CPT across the Port of Rotterdam. Furthermore, these areas are important locations for the construction of quay walls. For this thesis, only CPT measurements in these shaded regions will be used. The CPT data is collected from DINOloket and more specifically the CPT data will come from “Geotechnical cone penetration test (BRO)”.

Figure 3.2: Geographical areas selected for the thesis in shaded colors: Maasvlakte (light brown), Botlek (dark green) and Pernis (light blue).

In each of the three areas, a few filters are set so that the CPT datasets are somewhat comparable with each other. For the Maasvlakte, the CPT needs to have: (1) a starting year of 1982 or later, (2) u_2 pore pressure measurements, (3) a minimum depth of -40 m NAP and (4) followed *NEN 5140* or *NEN-EN-ISO 22476-12:2009*. For both the Botlek and Pernis, the CPT needs to have: (1) a starting year of 1982 or later and (2) reached a minimum depth of -40 m NAP.

The extra criteria for the Maasvlakte exist due to several reasons. The primary reason is to keep the number of CPT datasets within reasonable limits. The second reason is that the Maasvlakte is a relatively young area and more modern CPT equipment was used for the soil measurements. Thus, a large number of datasets would also have pore pressure measurements which is useful information for estimating the soil layers. Also, the “young” datasets would have the norms written down in their reports which would help to see which CPTs are mechanical or electronic. The reason that Botlek and Pernis do not have that criterium is because there would be too few datasets that fulfilled that criterium.

For each area, four specific sites are being investigated which are encircled in red in Figure 3.3 and the CPTs that are going to be used are the brown markers within the red circles. The size of the sites were determined with the criteria that the distance between CPTs are at most 1 km. Furthermore, the CPTs needed to share a similar stress history. So for example site M3 is along a quay wall and CPTs along that quay wall were used. Table 3.1 shows the number of CPTs that will be used at each site.

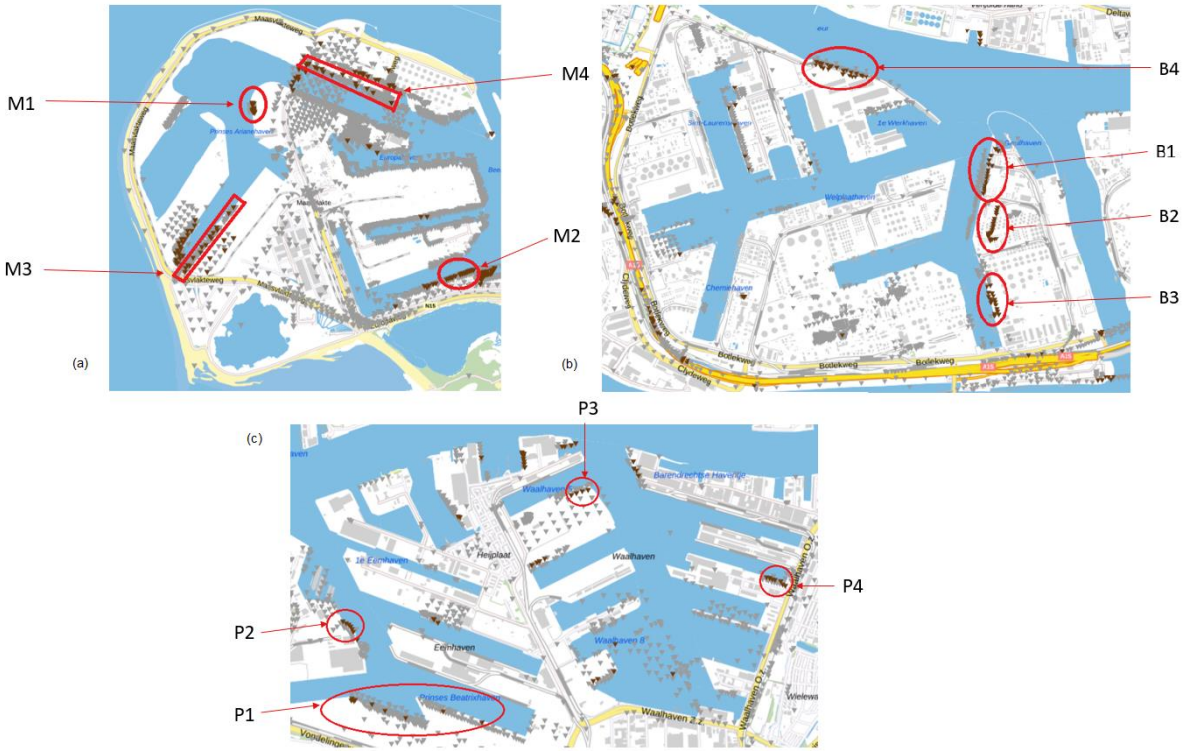

Figure 3.3: The investigated sites encircled in red and the individual CPTs as brown markers in (a) Maasvlakte, (b) Botlek and (c) Pernis.

Site	# of CPTs		
	Maasvlakte (M)	Botlek (B)	Pernis (P)
1	12	14	8
2	19	19	7
3	15	16	4
4	13	21	7

Table 3.1: Number of CPTs used at the sites

3.1.2. Data calibration

The CPT data contain measurements of the penetration length, cone resistance, friction resistance, the RD coordinates of the CPT which is the Dutch coordinate system and the corrected depth measured below a fixed surface which is the ground level.

In the CPT data, there can be missing values and those “no value” measurements are defined as 999.999 for the cone resistance and 9.999 for the friction resistance. The cone resistance and friction resistance measurements at a particular depth will be removed from the dataset if either the cone resistance at that depth has a value of 999.999 or 0 or if the friction resistance has a value of 9.999 or 0.

After that, the friction ratio is computed and for over-exaggerative friction ratio values which are values larger than 10%, the friction ratio is assumed to have no value. The measurements associated with friction ratio larger than 10% will be removed from the dataset.

If there are no pore pressure measurements in the CPT data, then the subsequent calculations will assume that the pore pressure is constantly zero. In the case that there are pore pressure measurements but with some containing missing values (being denoted as 99.999), the missing values are then assumed to be zero.

3.1.3. Soil profile generation

The calculation steps for the estimated soil profile are shown in Figure 3.4. Using a CPT from the dataset as an example, the result is shown in Figure 3.5

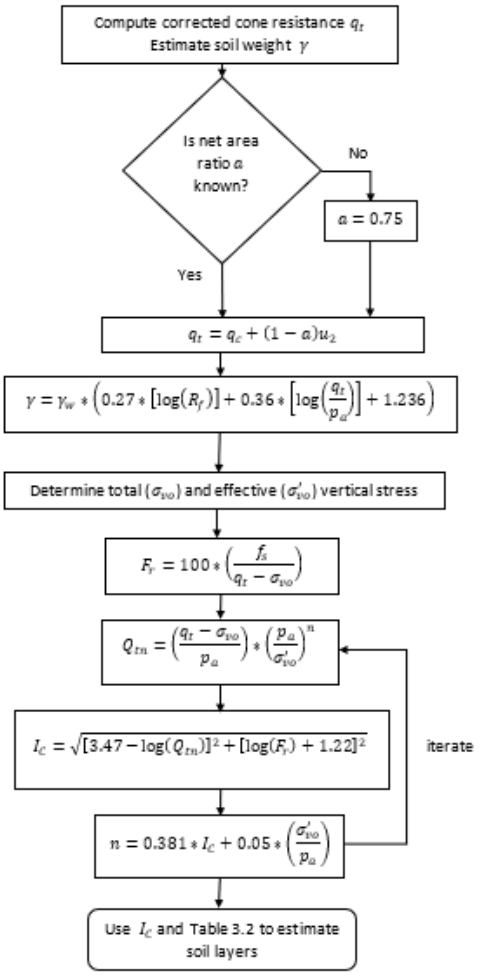

Figure 3.4: Calculation method for estimating the soil profile.

During the calculation process several assumptions were used:

- The atmospheric pressure p_a is assumed to be 100 kPa or 0.1 MPa and the unit weight of water γ_w is assumed to be 10 kN/m^3.
- At the first depth measurement of the CPT profile the total vertical stress is assumed to be zero.
- The GWT is the depth at which the first non-zero u_2 value was measured. If there are no pore pressure measurements, the GWT is assumed to be the last depth value above 0 m NAP. If the CPT profile starts below 0 m NAP, the GWT is assumed to be the first measured depth of the CPT profile.
- For the first iteration $n = 1$, Q_{tn} and I_C are computed and a new value for n is determined given that $n \leq 1$. If $n > 1$ then $n = 1$. The iterations stop when the difference between the n value of the current iteration and previous iteration is less than 0.01. From the final n value, the Q_{tn} and I_C are computed and this process is done at every depth measurement.

From the generated soil profile, the KRBXDE sand layer that is starting around -20 to -25 m NAP as seen in Figure 2.13, is selected and the q_c data in that layer will be used in the analysis stage. In cases where the KRBXDE layer goes beyond -40 m NAP, this thesis will only use the q_c data up to a depth of -40 m NAP. The base of foundation piles are placed usually around -20 m NAP to -35 m NAP. One would only investigate up to these depths and deeper cone resistance data would be considered unnecessary for these practical reasons.

First the sand layer is identified with the SBT_n zones. It is assumed that the sand layer falls under SBT_n zones 5, 6 and 7. The upper boundary (top of the layer) and lower boundary (bottom of the layer) of the sand are initially estimated at the depths where the SBT_n zone changes from zone 5 to zone 4 and vice versa as long as SBT_n zone 4 is a thick layer. If SBT_n zone 4 is a thin layer, it will be considered to be part of the sand layer. The initial estimated upper boundary and lower boundary of the sand layer include the transition zones that were discussed earlier in the literature review. In the analysis stage,

After that, a comparison is made with the estimated soil profiles from CPTs and the measured soil profiles from borehole data to verify whether the layer boundaries correspond to the correct type of soil and the correct geological formation. More generally the comparison is used to verify the estimation of soil profiles from CPT data. Also, any sub layers that may be observed within the sand layer will be included as part of the q_c data.

SBT_n zone	I_C	description
1	N/A	Sensitive, fine grained
2	> 3.60	Organic soils: clay
3	2.95 – 3.60	Clays: silty clay to clay
4	2.60 – 2.95	Silt mixtures: clayey silt to silty clay
5	2.05 – 2.60	Sand mixtures: silty sand to sandy silt
6	1.31 – 2.05	Sands: clean sand to silty sand
7	< 1.31	Gravelly sand to dense sand
8	N/A	Very stiff sand to clayey sand
9	N/A	Very stiff fine grained

Table 3.2: SBT_n zones and their respective index (I_C) values. Source: Robertson and Cabal (2015)

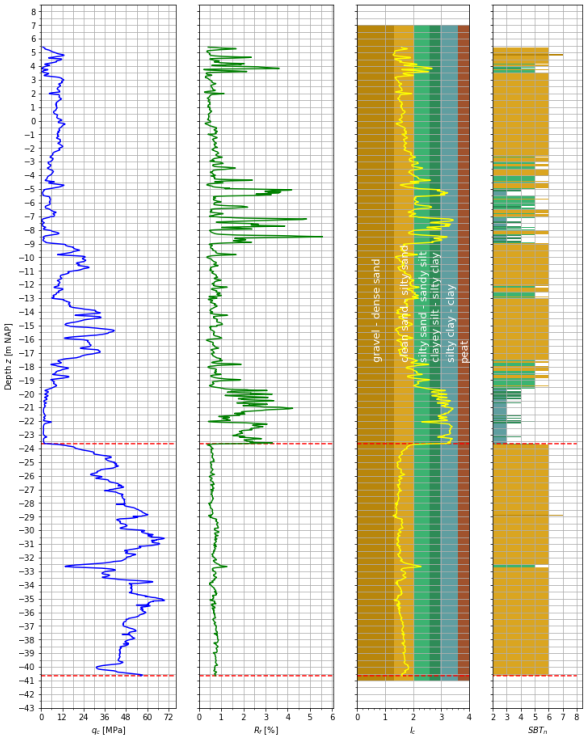

Figure 3.5: Pleistocene sand layer boundaries with cone resistance, friction ratio, SBT_n index and soil profile plotted over depth of CPT000000130993 (Maasvlakte).

3.2. Analysis stage

The autocorrelation fitting method for the vertical scale of fluctuation will be used to describe the vertical spatial variability of the Pleistocene sand layer. This method is chosen because one fits a one parameter model and it is a direct method in getting the vertical scale of fluctuation. For the spatial variability, the q_c data will be used. Normally, it would be better to use the q_t data as the pore pressure is taken into account. However, this thesis focuses on the Pleistocene sand layer and it is generally agreed upon that for sandy layers $q_c \approx q_t$. Hence, the q_c data will be used in the spatial variability analysis.

3.2.1. Vertical scale of fluctuation

For the vertical scale of fluctuation, the q_c data will be detrended and the autocorrelation fitting method that was discussed in the literature review will be used. The calculations only involve the Pleistocene sand layer.

Detrending the CPT data

The CPTs at each site are combined together to get an average trend for the site. The reason for this is because detrending the CPTs individually could lead to different trends to be identified which would lead to the partial removal of information about the spatial variability and it displays the large uncertainty of the trend identification. This is especially true in cases where CPTs are very close to each other. However, the large uncertainty can be reduced or better quantified if one were to combine the different CPTs to get the average trend.

The combined q_c data will be used to fit the average trendline $T(z)$ through it. The trendline parameters are determined with the ordinary least-squares method and the trendline is limited to a constant line, a linear first degree polynomial or a quadratic second degree polynomial. With regression analysis, the best trendline will be chosen based on the adjusted coefficient of determination, Akaike Information Criterion (AIC) and Bayesian Information Criterion (BIC). After detrending the q_c data of each individual CPT by

subtracting it from the average trendline, the residuals $\varepsilon(z)$ are left which will be used to compute the vertical scale of fluctuation for the individual CPTs. The residuals should either follow a lognormal or normal distribution with mean zero. A quantile-quantile plot is used to compare the residuals with the (log)normal distribution. The coefficient of determination is used to judge which distribution has the theoretical quantiles that best describe the quantiles of the residuals. An example of the detrending with $T(z)$ and $\varepsilon(z)$ is shown in the figure below.

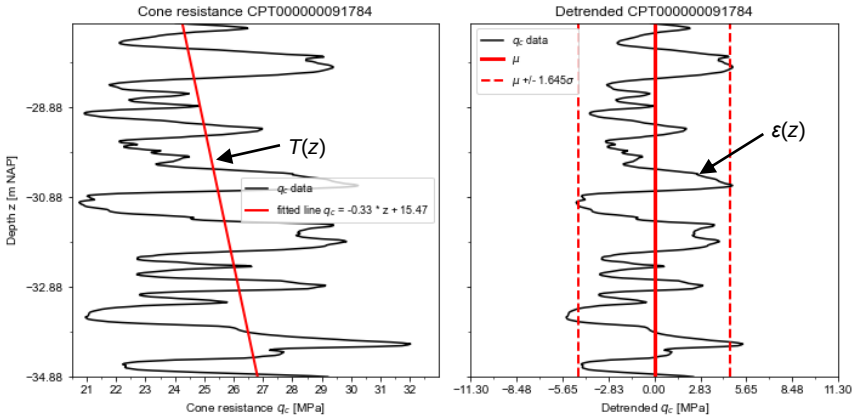

Figure 3.6: Example of detrending a CPT.

Autocorrelation fitting method

The autocorrelation fitting method is essentially fitting an autocorrelation model to the sample ACF. The sample ACF for a given separation distance $\tau_k = k\Delta z$ where μ is the mean of the residuals, is computed with the formula below:

$$\hat{\rho}(\tau_k) = \frac{\sum_{i=1}^{N-|k|}[\varepsilon(z_i) - \mu]\left[\varepsilon\left(z_{i+|k|}\right) - \mu\right]}{\sum_{i=1}^{N}[\varepsilon(z_i) - \mu]^2} \quad \textbf{(3.1)}$$

This equation is straightforward and uses the fact that the spacing distance Δz is constant. However that is not always the case and this thesis uses a more robust method to compute the sample ACF for every separation distance.

Given a vector of depth measurements $\mathbf{z} = \{z_0, z_1, z_2, \dots, z_N\}$ and residuals $\boldsymbol{\varepsilon} = \{\varepsilon(z_0)\varepsilon(z_1), \varepsilon(z_2), \dots, \varepsilon(z_N)\}$, square matrices $\mathbf{Z}$ and $\mathbf{E}$ are created with size (N, N). The column j represents the depth measurement z_j and the row i represents the depth measurement z_i. The location $\mathbf{Z}(i,j)$ is the separation distance between z_i and z_j and it is rounded off to the nearest centimeter. Similarly the correlation matrix $\mathbf{E}$ is created using the same conditions as for $\mathbf{Z}$. The column j represents $\varepsilon\left(z_j\right)$ and the row i represents $\varepsilon(z_i)$. The location $\mathbf{E}(i,j)$ represents the correlation of $\varepsilon(z_i)$ and $\varepsilon\left(z_j\right)$ with the variance σ^2 being computed as $\sigma^2 = \sum_{i=1}^{N}[\varepsilon(z_i) - \mu]^2$.

$$\mathbf{Z}(i,j) = z_i - z_j \quad \textbf{(3.2)}$$

$$\mathbf{E}(i,j) = \frac{1}{\sigma^2}\left[[\varepsilon(z_i) - \mu] * \left[\varepsilon\left(z_j\right) - \mu\right]\right] \quad \textbf{(3.3)}$$

Next, the measured separation distances $\boldsymbol{\tau} = \{\tau_0, \tau_1, \tau_2, \dots, \tau_m\}$ are identified which are the unique values of the $\mathbf{Z}$ matrix. For a separation distance τ_s, one needs to find the indices of $\mathbf{Z}(i,j) = \tau_s$. The found indices are then used to find the corresponding $\mathbf{E}$ matrix values and those $\mathbf{E}$ matrix values are summed up to get the sample autocorrelation function $\hat{\rho}(\tau_s)$ at separation distance τ_s.

In this case, only sample ACF at separation distances that are the multiples of Δz = 2 cm or multiples of Δz = 5 cm, are used for model fitting. The spacing distance Δz = 2 cm is chosen because that was the chosen depth interval for CPT measurements and the spacing distance of Δz = 5 cm is chosen if the 2 cm is too small to get an accurate fit.

Five different autocorrelation models are fitted to the sample ACF with the models having the vertical scale of fluctuation as its only parameter. The five different models are: (1) the single exponential model (SNX), (2) the squared exponential model (SQX), (3) the cosine exponential (CSX), (4) the spherical model and (5) the triangular model. The formulae for the models can be found in Table 2.5 and the autocorrelation models are shown in Figure 2.7.

This choice of models is based on the fact that according to Cami et al. (2020) these five models are the most frequently used models. For a CPT, the best model is chosen based on the criteria of the lowest residual sum of squares and whether the estimated vertical SF is in line with the vertical SF values from other CPTs at the same site.

3.2.2. Influence of the spatial variability on pile design

The spatial variability and the coefficient of variation of the cone resistance $c_v(q_c)$ influence the pile design. In order to see how large their influence are a hypothetical situation is sketched where the base of the foundation pile with pile diameter D lies in the KRBXDE sand layer and the pile base capacity needs to be computed. The pile base will be at a depth where the zone of influence around the pile base is captured in the sand layer. Averaging methods are necessary for computing the pile base capacity thus this section in particular assesses the effects of averaging methods given that the spatial variability is known. The relationship between spatial variability and averaging methods were discussed in the literature review.

For each site, the fast Fourier transform moving average method algorithm is used to simulate 1D q_c data with the trendline, $c_v(q_c)$ and θ_v as input parameters. The FFT-MA algorithm is chosen because it is easier to program than the local average subdivision algorithm and it is not as computationally intensive as the covariance decomposition algorithm.

In the case that the simulated $q_c < 2$ MPa the q_c value is set at 2 MPa and in the case that the simulated $q_c > 100$ MPa the q_c value is set at 100 MPa. N simulations are performed and for each simulation the Koppejan and LCPC method are used to compute the pile base capacity and from the N pile base capacities the coefficient of variation of the pile base capacity $c_v(Q_b)$ is computed as well.

In order to see the influence the $c_v(q_c)$ and θ_v on the pile design, $c_v(Q_b)$ is computed for different values of $c_v(q_c)$ and θ_v. From that for each site, plots are made of $c_v(q_c)$ against $c_v(Q_b)$ given that θ_v is constant. Similarly, plots of θ_v against $c_v(Q_b)$ are made given that $c_v(q_c)$ is constant.

4. Results and discussion

This chapter will mainly present the results from the analysis stage of the methodology and at the end will hold a discussion about the results. Information about the CPTs and results from the preparation stage like the borehole verification step can be found in Appendix C. More results from the analysis stage which includes figures and tables about the sites and individual CPTs can be found in Appendix D.

4.1. Results soil layer identification

In order to validate the estimated soil profile, a comparison was made between the measured soil profile from a borehole measurement and the estimated soil profiles that are within 500 m of the borehole. Table 4.1 summarizes the mean difference between the estimated and measured upper Pleistocene sand layer boundaries for all the sites. The tables and figures for the individual sites can be found in Appendix C. There will be differences in the boundaries of the sand layer as the borehole and CPTs are not at the exact location and those layer boundaries can change over a few 100 meters as seen in Figure 2.13. These "errors" are usually in the order of 10 cm to 1 m and it can be considered to be an acceptable error for this thesis as it mainly focuses on the Pleistocene sand whose layer thickness is in the order of several meters.

Site	Mean difference estimated and measured [m]	Site	Mean difference estimated and measured [m]	Site	Mean difference estimated and measured [m]
M1	+1.56	B1	-2.31	P1	-1.67
M2	-0.12	B2	+1.51	P2	-0.75
M3	-0.76	B3	-1.40	P3	+1.06
M4	+0.29	B4	-1.50	P4	-0.07

Table 4.1: Mean difference between the estimated and measured upper Pleistocene sand layer boundaries.

4.2. Results trend removal

The trendlines for the individual sites and the distribution of the residuals can be found in the tables and figures in Appendix D.

Maasvlakte

Figure 4.1 shows the results of the trend removal for every site in the Maasvlakte. The figure shows that three sites can be modelled as a linear trend while the other one is a constant trend. Site M2 has two different trend lines as all the CPTs across the site share the same picture of two distinct sublayers. As such, site M2 CPTs were divided into two subgroups and for each subgroup the trend removal and vertical scales of fluctuation will be computed accordingly.

After the trend removal, the residuals of a site should follow either a normal or lognormal distribution. Figure 4.2 shows that the residuals follow a normal distribution for all sites.

Additionally, the coefficient of variation of the cone resistance was computed for every individual CPT. This was done by dividing the cone resistance by the trend line and taking the standard deviation from that ratio. The results are summarized in Table 4.2 and it shows that the range of $c_v(q_c)$ are roughly the same across the four sites. Also the mean of $c_v(q_c)$ for the four sites do not differ that much from each other.

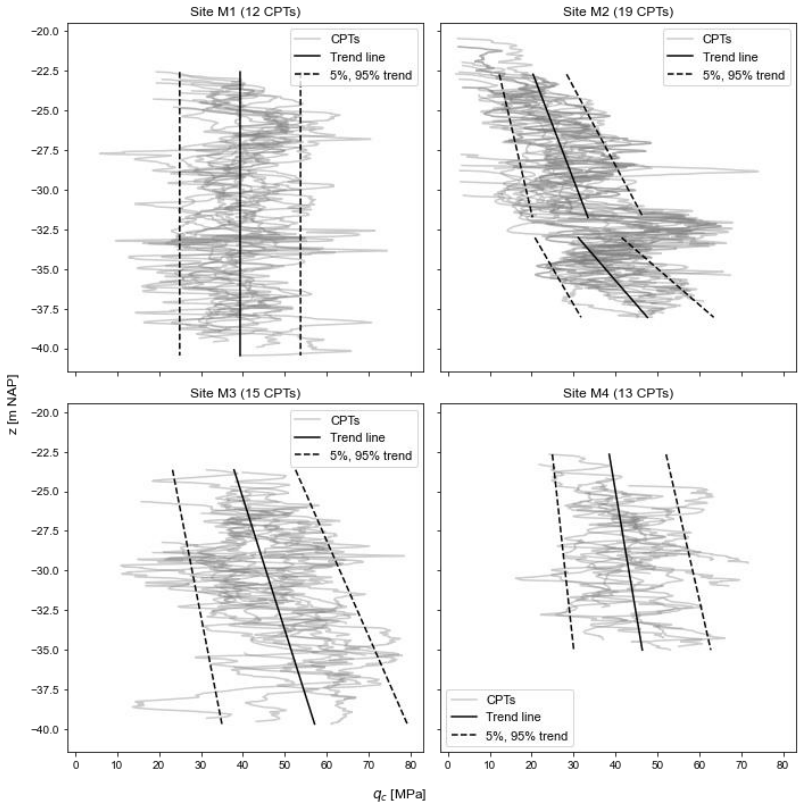

Figure 4.1: Trend lines of the Maasvlakte sites.

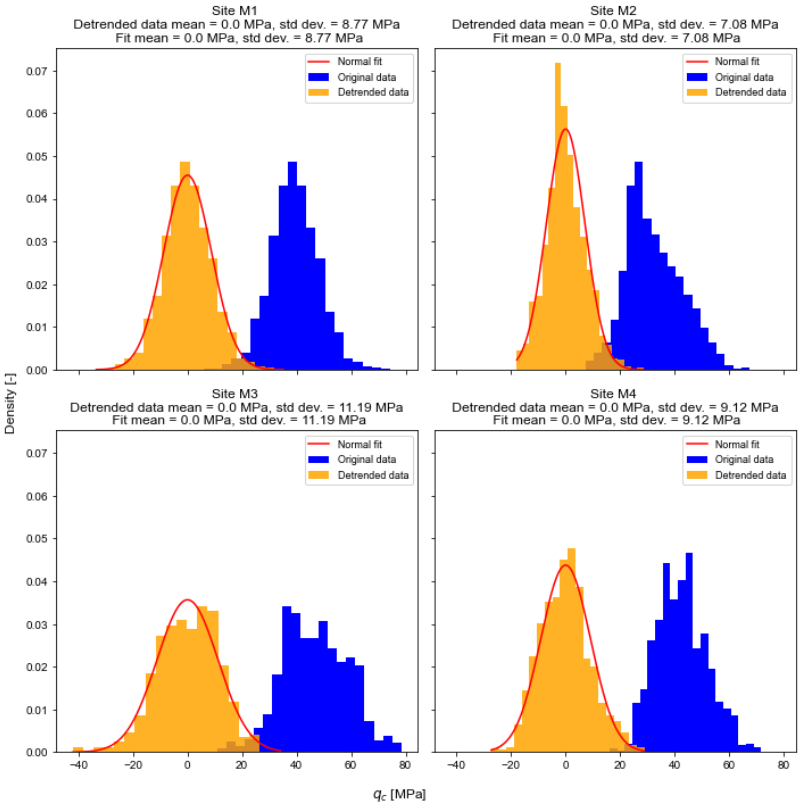

Figure 4.2: Histogram of the detrended cone resistance data and fitted distributions in the Maasvlakte.

	$c_v(q_c)$	
Site	Range (min. – max.) [-]	Mean [-]
M1	0.11 – 0.29	0.21
M2	0.05 – 0.32	0.17
M3	0.10 – 0.32	0.19
M4	0.08 – 0.25	0.17

Table 4.2: coefficient of variation of cone resistance for the Maasvlakte sites.

Botlek

Figure 4.3 shows the results of the trend removal for every site in the Botlek. The results shows that the trends at all four sites can be modeled as a linear trend. The cone resistance at the Botlek sites are less than the cone resistance at the Maasvlakte sites at the same depth interval. The Maasvlakte sites have a cone resistance of 20 – 40 MPa at -22.5 m NAP while the Botlek sites have a cone resistance of 20 – 25 MPa at the same depth. The residuals at two sites follow a normal and the other two sites have a lognormal distribution as seen in Figure 4.4. Sites B1 and B2 have a normal distribution while B3 and B4 have a lognormal distribution.

The coefficients of variation of the cone resistance for the Botlek sites are summarized in Table 4.3 and it shows that the range and mean of $c_v(q_c)$ are roughly the same for sites B1 and B2. The same holds true when looking at sites B3 and B4. Overall, the $c_v(q_c)$ of the Botlek sites are the same as the Maasvlakte sites with the mean $c_v(q_c)$ being slightly higher than the mean $c_v(q_c)$ of the Maasvlakte sites.

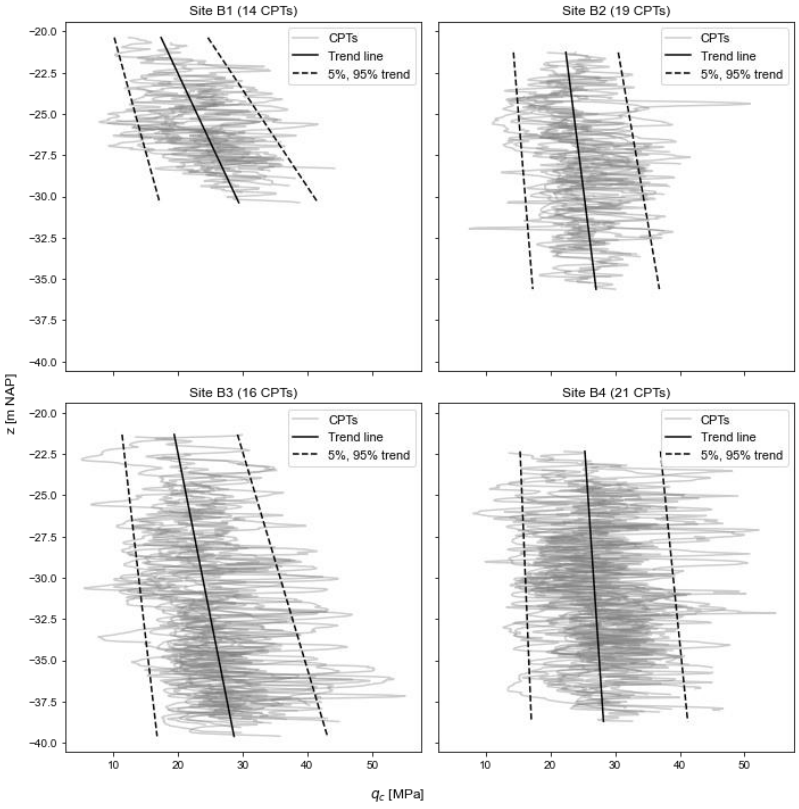

Figure 4.3: Trend lines of the Botlek sites.

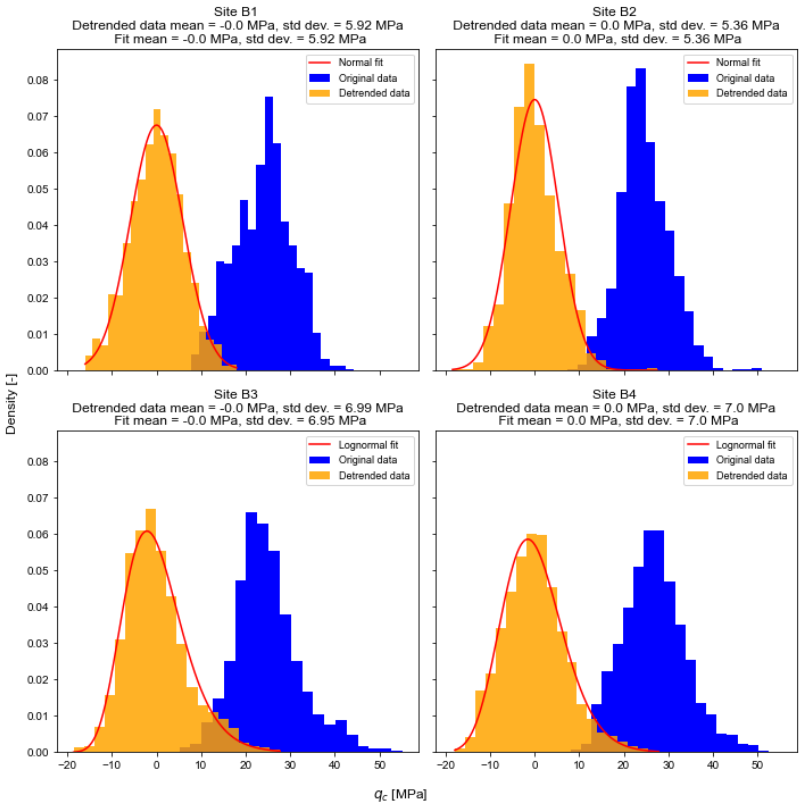

Figure 4.4: Histogram of the detrended cone resistance data and fitted distributions in the Botlek.

	$c_v(q_c)$	
Site	Range (min. – max.) [-]	Mean [-]
B1	0.08 – 0.30	0.20
B2	0.10 – 0.28	0.20
B3	0.11 – 0.33	0.25
B4	0.14 – 0.38	0.24

Table 4.3: coefficient of variation of cone resistance for the Botlek sites.

Pernis

Figure 4.5 shows the results of the trend removal for every site in Pernis. They show that two out of the four sites can be modelled as a linear trend while the other two are a constant trend. Figure 4.6 shows that the residuals at three sites follow a normal distribution while site P4 follows a lognormal distribution.

The coefficients of variation of the cone resistance for the Pernis sites are summarized in Table 4.4 and it shows that the range and mean of $c_v(q_c)$ are roughly the same for sites P1 and P2 with P1 having a slightly larger range. The range and mean of $c_v(q_c)$ are roughly the same when looking at sites P3 and P4.

	$c_v(q_c)$	
Site	Range (min. – max.) [-]	Mean [-]
P1	0.09 – 0.39	0.27
P2	0.15 – 0.38	0.27
P3	0.16 – 0.23	0.21
P4	0.16 – 0.26	0.20

Table 4.4: coefficient of variation of cone resistance for the Pernis sites.

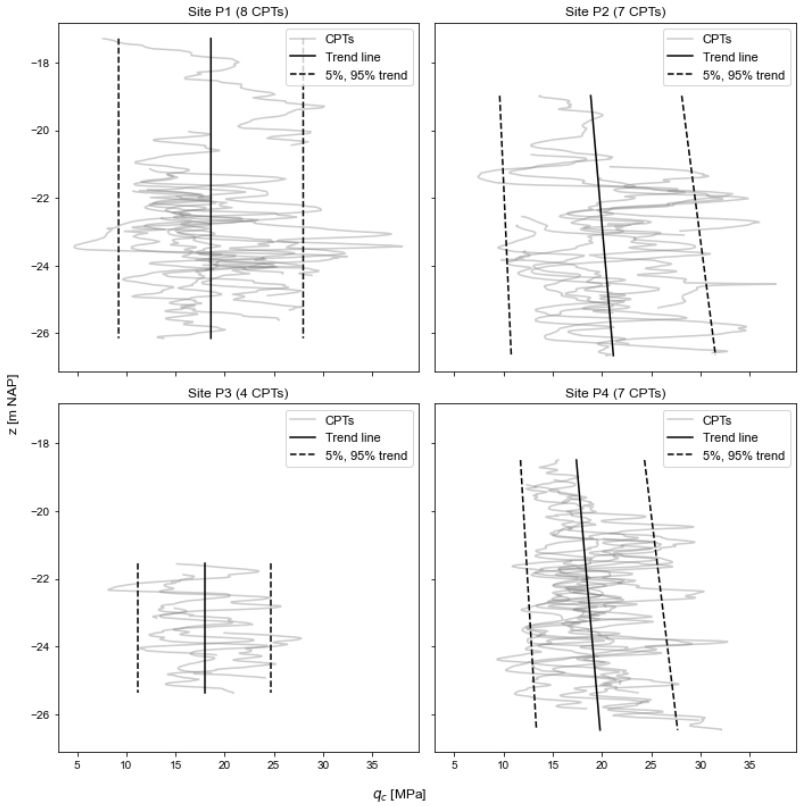

Figure 4.5: Trend lines of the Pernis sites.

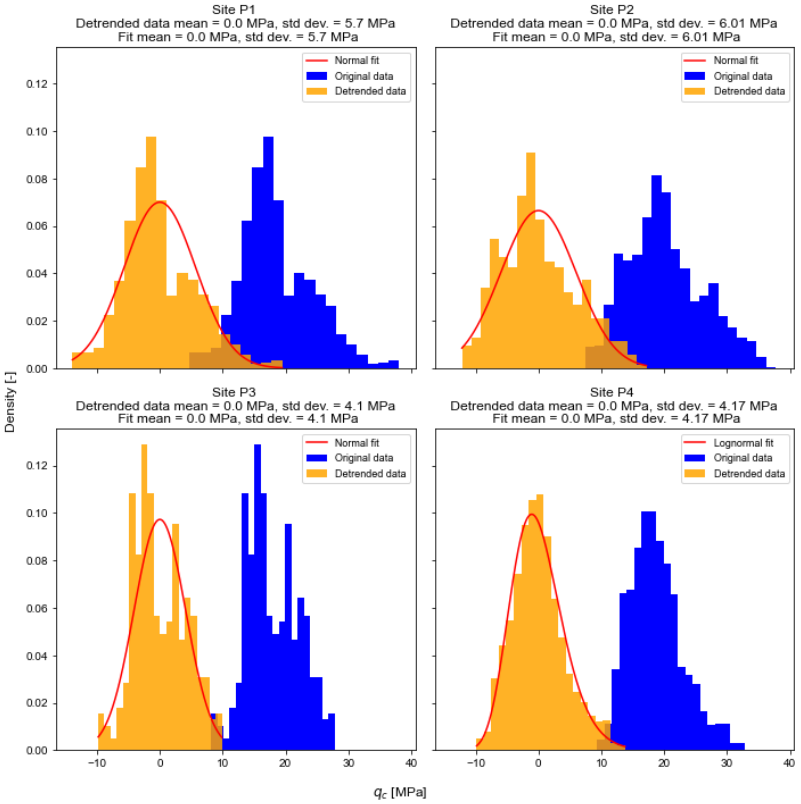

Figure 4.6: Histogram of the detrended cone resistance data and fitted distributions in Pernis.

4.3. Vertical scale of fluctuation

The results of the vertical scale of fluctuation of individual CPTs and sites can be found in the tables and figures in Appendix D.

Maasvlakte

Figure 4.7 displays a histogram of the vertical scales of fluctuation that were computed from the individual CPTs at the four sites. It can be seen that site M1 has a particular small range of θ_v values. Site M2 shows somewhat two clusters of θ_v values which are centered around the 0 – 1 m range and the 1.5 – 2 m range Site M3 has θ_v values that are somewhat uniformly distributed across the 0.5 – 3 m range. Site M4 has quite a lot θ_v values which around 1 m. Figure 4.8 shows the computed autocorrelations for the Maasvlakte sites together with the models for the mean vertical scale of fluctuation and the 5 and 95 percentiles that are acting as confidence intervals. The outlier in Figure 4.8 at site M4 comes from a sublayer and despite having a sample ACF which is somewhat irregular compared to other sample ACFs, it shows a vertical scale of fluctuation which is in line with the other θ_v values that were found at the site.

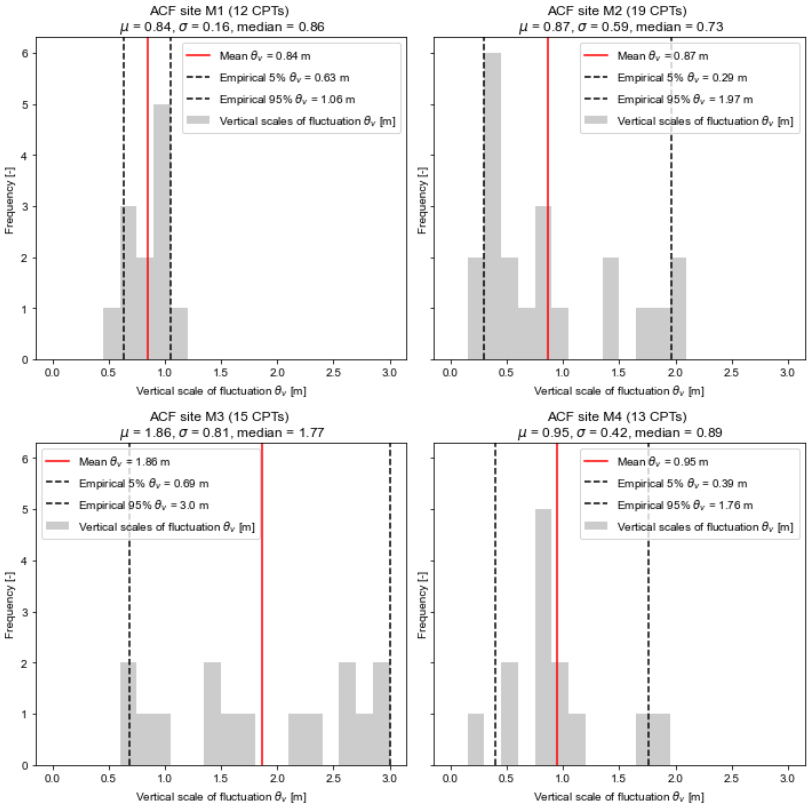

Figure 4.7: Vertical scales of fluctuation of individual CPTs per site in the Maasvlakte.

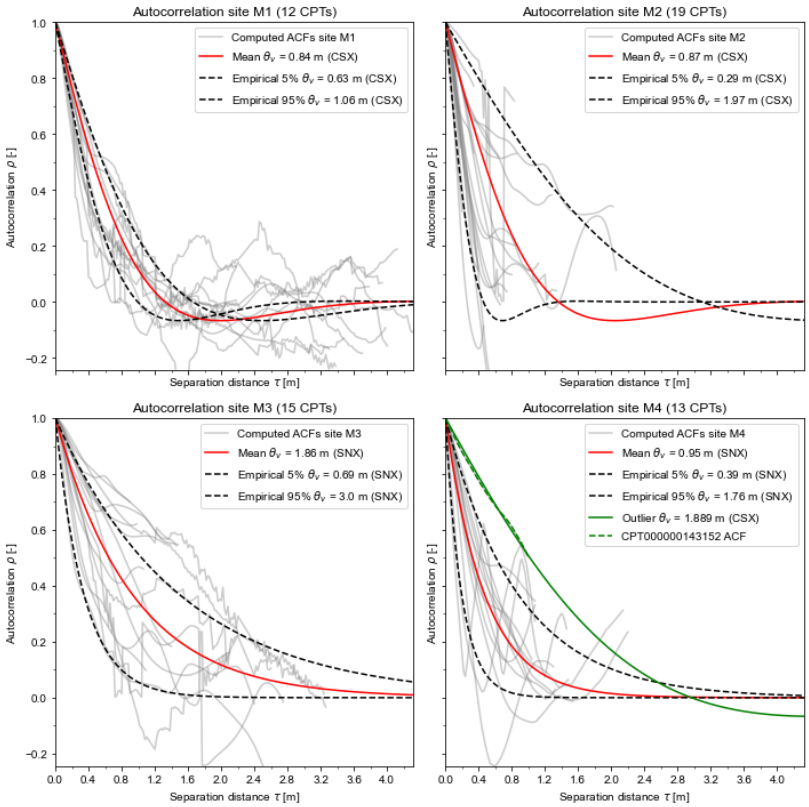

Figure 4.8: Autocorrelation plots of the Maasvlakte sites.

	θ_v				
Site	Range (min. – max.) [m]	Mean [m]	$c_v(\theta_v)$ [-]	5% [m]	95% [m]
M1	0.58 – 1.12	0.84	0.19	0.63	1.06
M2	0.26 – 1.98	0.87	0.68	0.29	1.97
M3	0.66 – 3.00	1.86	0.44	0.69	3.00
M4	0.29 – 1.89	0.95	0.45	0.39	1.76

Table 4.5: Summary of the estimated vertical scales of fluctuation at the Maasvlakte sites.

Table 4.5 is a summary of the statistics of the vertical scales of fluctuation at the Maasvlakte sites. It shows that sites M1, M2 and M4 share roughly the same mean but site M3 stands out with a mean of 1.88 m. The coefficient of variation shows that site M1 has a quite small dispersion of θ_v values. Thus one would not expect much variation of θ_v values at that site. Site M2 has the largest dispersion of θ_v values of all Maasvlakte sites while sites M3 and M4 have roughly the same dispersion of θ_v values.

Botlek

Figure 4.9 displays a histogram of the vertical scales of fluctuation that were computed from the individual CPTs at the four sites. It can be seen that sites B1, B2 and B3 share roughly the same range of θ_v values. Site B4 has quite a very small range of θ_v values compared to the other sites. Figure 4.10 shows the computed autocorrelations for the Botlek sites. The outlier in Figure 4.10 at site B3 is one that is part of the dataset as it has a CPT profile that agrees well with the average trendline and its sample ACF follows the other sample ACFs quite well.

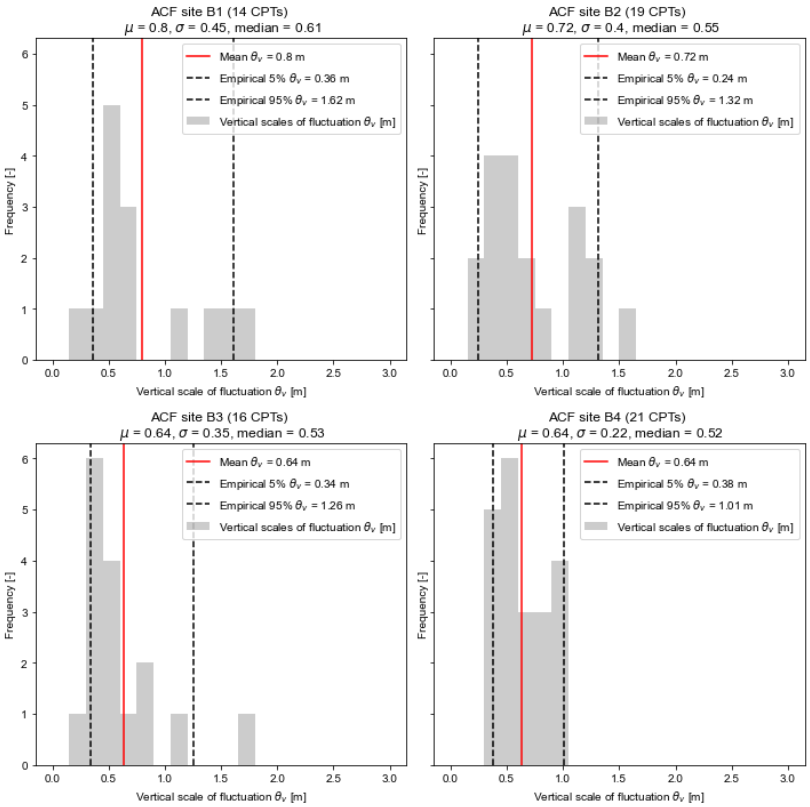

Figure 4.9: Vertical scales of fluctuation of individual CPTs per site in the Botlek.

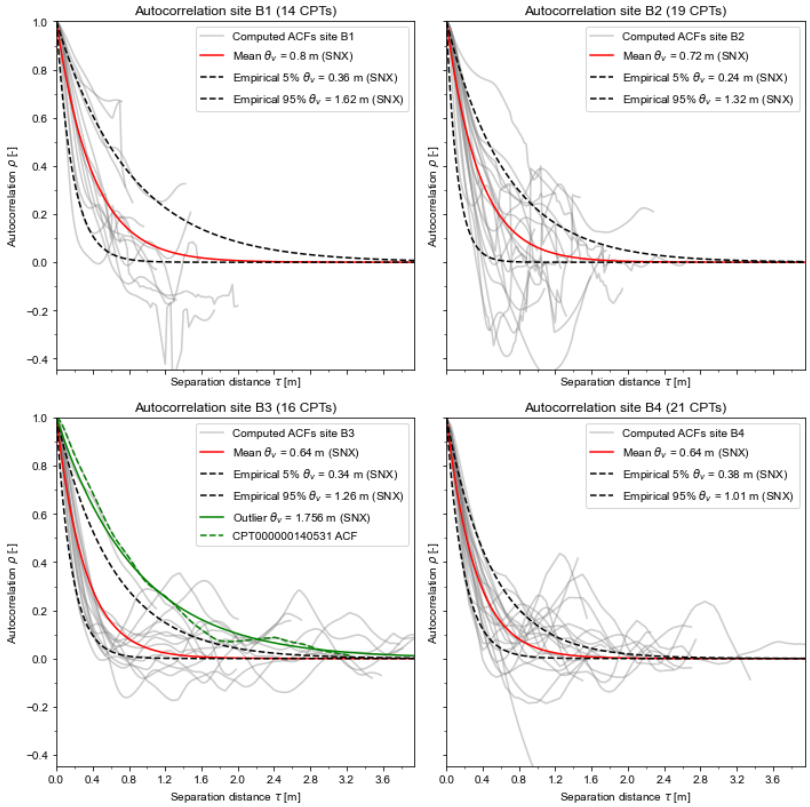

Figure 4.10: Autocorrelation plots of the Botlek sites.

	θ_v				
Site	Range (min. – max.) [m]	Mean [m]	$c_v(\theta_v)$ [-]	5% [m]	95% [m]
B1	0.25 – 1.70	0.80	0.56	0.36	1.62
B2	0.24 – 1.64	0.72	0.55	0.24	1.32
B3	0.27 – 1.76	0.64	0.55	0.34	1.26
B4	0.37 – 1.01	0.64	0.34	0.38	1.01

Table 4.6: Summary of the estimated vertical scales of fluctuation at the Botlek sites.

Table 4.6 is a summary of the statistics of the vertical scales of fluctuation at the Botlek sites. The coefficient of variation and the range show that sites B1, B2 and B3 share the same level of dispersion and range of θ_v values but site B4 has a considerably lower range and dispersion of θ_v values. The mean vertical scale of fluctuation shows that the Botlek sites are just as spatially variable as the Maasvlakte if not more. This is because a lower θ_v means that the cone resistance is more spatially variable.

Pernis

Figure 4.11 displays a histogram of the vertical scales of fluctuation that were computed from the individual CPTs at the four sites. It can be seen that sites P1, P2 and P4 share roughly the same range of θ_v values. Sites P1, P3 and P4 share a similarity as much of their θ_v values are concentrated around 0.5 m. Site P2 has it more uniformly distributed across the 0 – 1 m range. Figure 4.12 shows the computed autocorrelations for the Pernis sites.

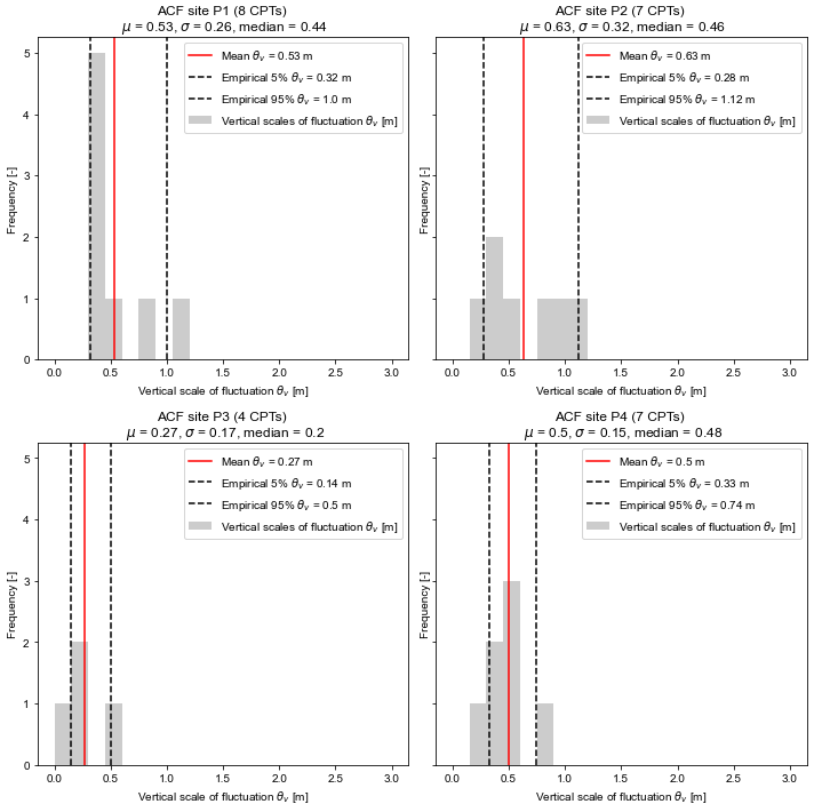

Figure 4.11: Vertical scales of fluctuation of individual CPTs per site in Pernis.

	θ_v				
Site	Range (min. – max.) [m]	Mean [m]	$c_v(\theta_v)$ [-]	5% [m]	95% [m]
P1	0.31 – 1.10	0.54	0.49	0.32	1.00
P2	0.24 – 1.18	0.63	0.51	0.28	1.12
P3	0.14 – 0.24	0.27	0.61	0.14	0.50
P4	0.29 – 0.82	0.50	0.30	0.33	0.74

Table 4.7: Summary of the estimated vertical scales of fluctuation in the Pernis groups.

Table 4.7 is a summary of the statistics of the vertical scales of fluctuation at the Pernis sites. Sites P1 and P2 share nearly the same statistics and one should be skeptical about the P3 statistics as it is the site with smallest number of CPTs. Site P4 has a smaller range and mean than P1 and P2 and the coefficient of variation shows that the P4 has a smaller dispersion of θ_v values than the other Pernis sites. Overall, Table 4.7 shows that the Pernis sites are the most spatially variable of all sites but it should be noted that the Pernis sites had far fewer CPTs than the Maasvlakte and Botlek sites.

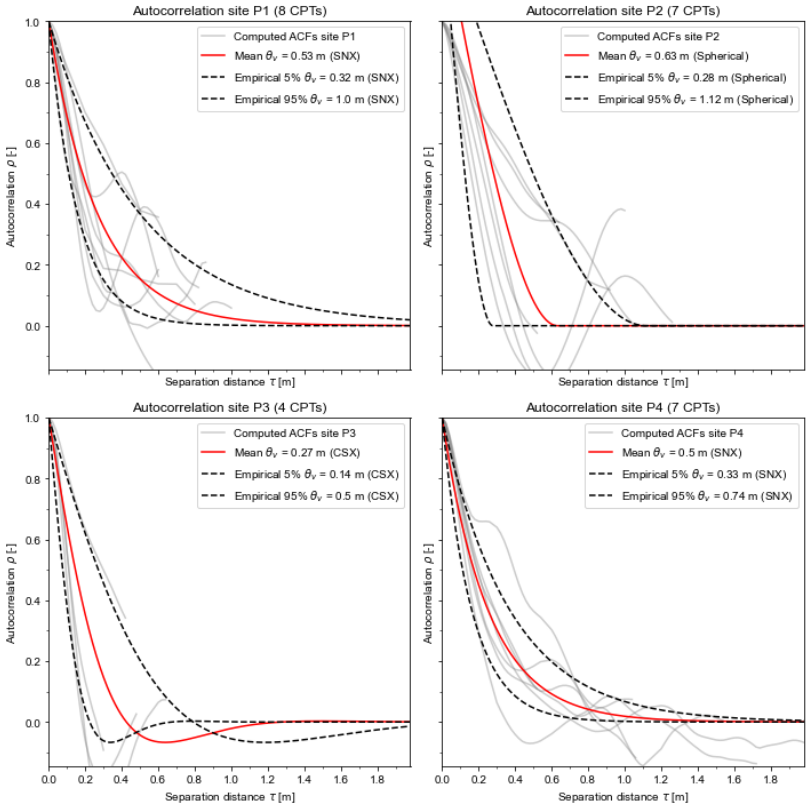

Figure 4.12: Autocorrelation plots of the Pernis sites.

4.4. Results influence spatial variability on pile design

For the hypothetical driven pile a diameter of 0.3 m was used and the q_c data was simulated for different $c_v(q_c)$ values of 0 – 0.45 and for θ_v values of 0 – 3 m. The pile base capacity was computed using the Dutch pile design method with two different averaging techniques: the LCPC method with end bearing capacity factor $k_c = 0.5$ and the Koppejan method with pile reduction factor $\alpha_p = 0.7$. For each combination of $c_v(q_c)$ and θ_v, 500 q_c data simulations were performed and for each simulation the pile base capacity was computed. The coefficient of variation of the pile base capacity $c_v(Q_b)$ was computed from those 500 simulations. An example q_c simulation using the site M1 statistics is shown in Figure 4.13.

This chapter will only show the results from two sites per area. The results for the other sites can be found in the tables and figures in Appendix D.

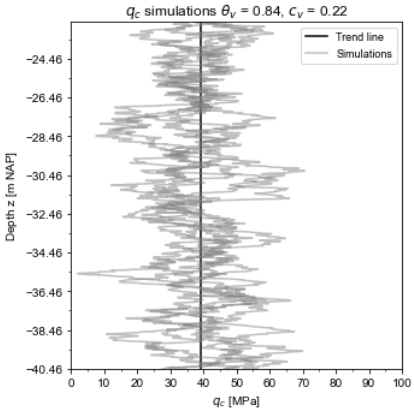

Figure 4.13: Example q_c simulation using the site M1 statistics.

Maasvlakte

Figure 4.14 and Figure 4.15 show the coefficients of variation of pile base capacity for different values of θ_v and $c_v(q_c)$ at sites M1 and M3. When focusing on the plots at the right, it seems that $c_v(Q_b)$ enters a steady-state for high values of θ_v/D. It shows that large vertical scales of fluctuation do not affect the $c_v(Q_b)$ much regardless of using the LCPC or Koppejan method. However, $c_v(q_c)$ seems to affect the $c_v(Q_b)$ much more than the vertical scales of fluctuation.

What is noticeable is that at $c_v(q_c) = 0.45$, the Koppejan method has a large dispersion in $c_v(Q_b)$ among different θ_v/D values. The LCPC method does not have that large dispersion and it shows a gradual increase in $c_v(Q_b)$ with increasing $c_v(q_c)$ but the increase in $c_v(Q_b)$ is not as steep as for the Koppejan method.

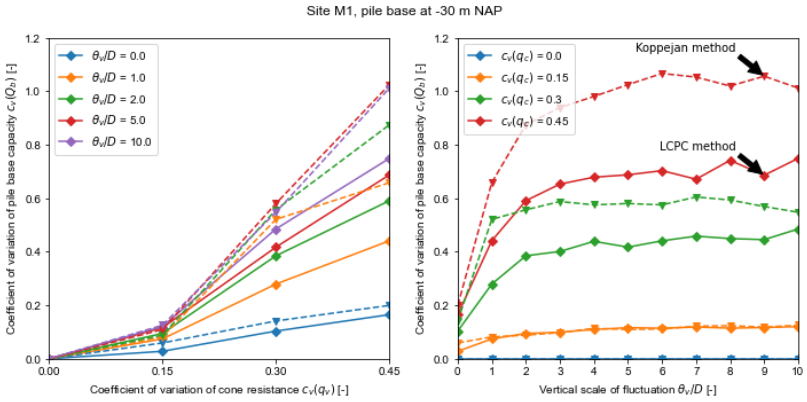

Figure 4.14: Site M1 coefficients of variation of pile base capacity.

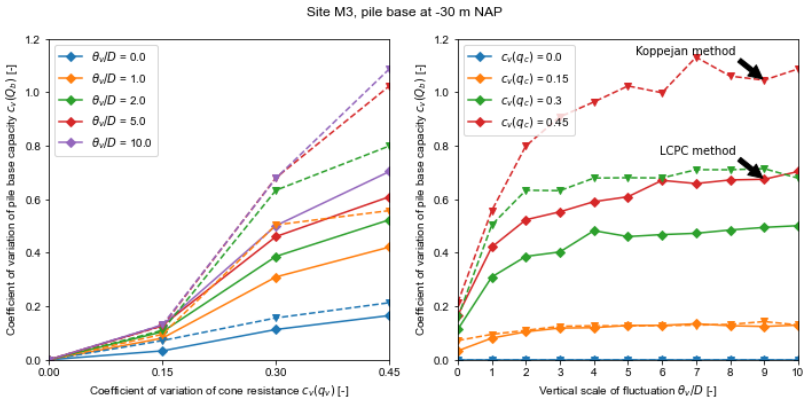

Figure 4.15: Site M3 coefficients of variation of pile base capacity.

Botlek

Figure 4.16 and Figure 4.17 show the coefficients of variation of pile base capacity for different values of θ_v and $c_v(q_c)$ at sites B1 and B3. The $c_v(Q_b)$ enters a steady-state for high values of θ_v/D and it seems that this occurrence is a characteristic of the averaging methods rather than being a characteristic of the sites. Also for the plots on the left, the $c_v(Q_b)$ closely follow the same path for different θ_v/D values. The effect of the vertical scale of fluctuation on $c_v(Q_b)$ is more damped in the LCPC method than in the Koppejan method.

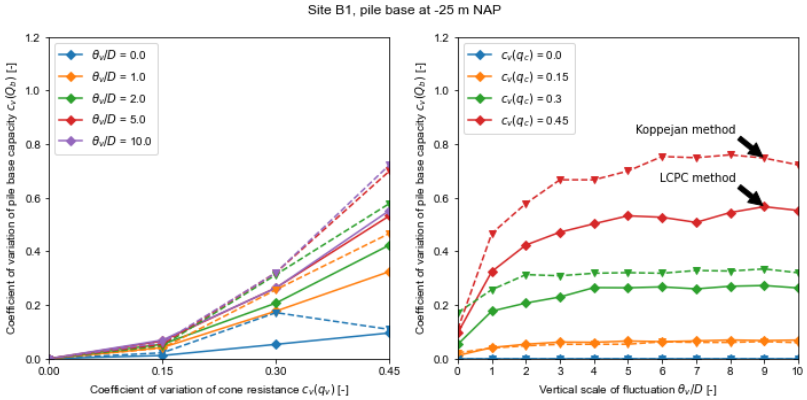

Figure 4.16: Site B1 coefficients of variation of pile base capacity.

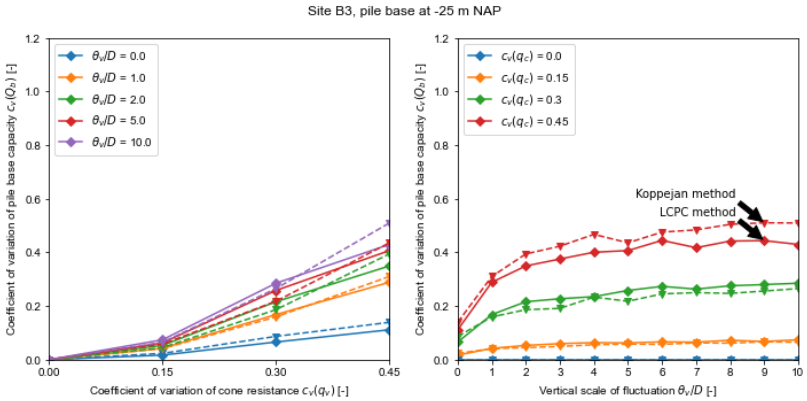

Figure 4.17: Site B3 coefficients of variation of pile base capacity.

Pernis

Figure 4.18 and Figure 4.19 show the coefficients of variation of pile base capacity for different values of θ_v and $c_v(q_c)$ at sites P1 and P3. Just like with the previous figure, the $c_v(Q_b)$ enters a steady-state for high values of θ_v/D and the effect of θ_v on $c_v(Q_b)$ is more damped in the LCPC method than in the Koppejan method.

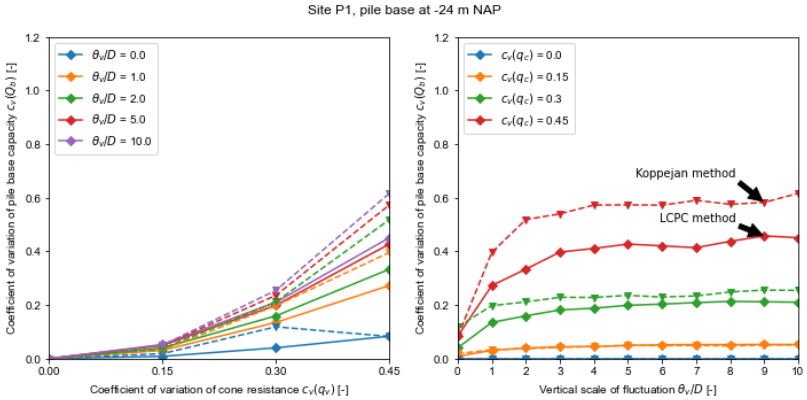

Figure 4.18: Site P1 coefficients of variation of pile base capacity.

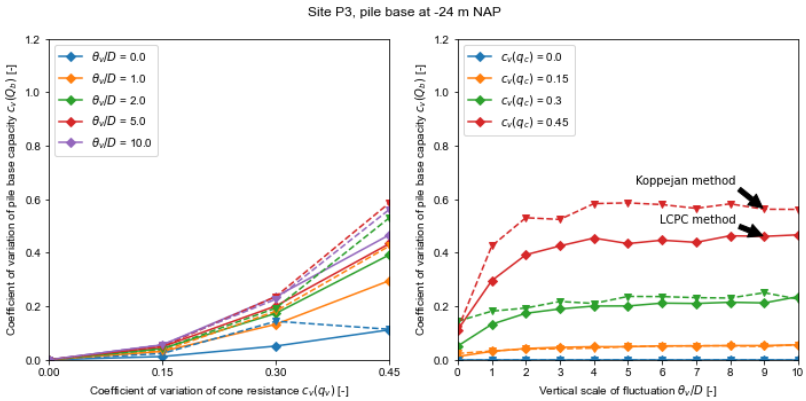

Figure 4.19: Site P3 coefficients of variation of pile base capacity.

4.5. Discussion

The results from the detrending and spatial variability across all sites are summarized in Table 4.8 – Table 4.10. As there are two clear sublayers at site M2, two mean q_c values are given as well in the table. The mean q_c of 26.69 MPa refers to the top sublayer while the other refers to the bottom sublayer. More information can be found in Appendix D.

	Mean q_c [MPa]		
Site	Maasvlakte	Botlek	Pernis
1	39.32	23.89	18.60
2	26.69/40.08	24.59	20.18
3	46.79	24.82	17.96
4	42.49	26.81	18.64

Table 4.8: Summary of the mean q_c across all sites.

	$c_v(q_c)$ [-]		
Site	Maasvlakte	Botlek	Pernis
1	0.11 – 0.29	0.08 – 0.30	0.09 – 0.39
2	0.05 – 0.32	0.10 – 0.28	0.15 – 0.38
3	0.10 – 0.32	0.11 – 0.33	0.16 – 0.23
4	0.08 – 0.25	0.14 – 0.38	0.16 – 0.26

Table 4.9: Summary of the coefficient of variation of q_c across all sites.

	θ_v [m]		
Site	Maasvlakte	Botlek	Pernis
1	0.58 – 1.12	0.25 – 1.70	0.31 – 1.10
2	0.26 – 1.98	0.24 – 1.64	0.24 – 1.18
3	0.66 – 3.00	0.27 – 1.76	0.14 – 0.24
4	0.29 – 1.89	0.37 – 1.01	0.29 – 0.82

Table 4.10: Summary of the vertical scale of fluctuation across all sites.

The detrending shows that the Maasvlakte, Botlek and Pernis sites have mean coefficients of variation of the cone resistance $c_v(q_c)$ of around 0.2 – 0.3. It means that the mean dispersion of CPT data does not vary much across sites. Of course, the $c_v(q_c)$ values vary across the sites but if a CPT has point statistics of $c_v(q_c) \leq 0.4$ it can be considered to be within expected range. The min/max range of $c_v(q_c)$ values do not change much across sites and across areas. Thus it seems that as far as $c_v(q_c)$ is concerned, it does not matter whether you are in the Maasvlakte, Botlek or Pernis. But the mean q_c in the Maasvlakte is higher than in the other areas and with similar $c_v(q_c)$ the standard deviation in the Maasvlakte will also be higher than in the other areas. This leads to a higher probability of the Maasvlakte being affected by the limiting factor of q_b at 15 MPa and that reduces the

coefficient of variation of pile base capacity in the Maasvlakte. This is not necessarily good as the reduced variability

The min/max range of the vertical scales of fluctuation in the Botlek do no differ much from the min/max range in the Maasvlakte with the exception of site M3. But when looking at the mean vertical scales of fluctuation, you see that the Maasvlakte is the least spatially variable followed by the Botlek and Pernis. Thus it seems that the vertical spatial variability increases as one moves inland and this gives the impression that the river Meuse has an influence on the vertical spatial variability. However, there is no clear evidence whether this impression is correct and more investigation is needed.

One possible explanation for the vertical spatial variability decreasing as one moves from Pernis to the Maasvlakte, is due to the geological formation. It can be that the Maasvlakte sand layer consists of the older layer of the Kreftenheye Formation with a small younger layer of the Boxtel Formation on top. The Botlek and Pernis would have a thick layer of the Boxtel Formation, Delwijnen Member which is slightly younger than the Kreftenheye Formation. It could be because of age that the younger Delwijnen Member causes the Botlek and Pernis to be more spatially variable. Or it could be that the fine-grained sand from the Delwijnen Member is transported in the river system through aggradation and degradation and that causes the Botlek and Pernis to be more spatially variable. As a recommendation, one could subdivide the geological formation into sublayers based on age and compute the spatial variability for the sublayers. The older sublayers at greater depths should have a larger grain size than the younger sublayers. The soil in the younger sublayers should then be more affected by sediment transport in the Rhine-Meuse river system as it is finer grained than the soil in the older sublayers. Thus relatively speaking, the younger sublayers should be more spatially variable than the older sublayers.

The effect the vertical spatial variability has on computing the pile base capacity is minimal compared to the influence of the coefficient of variation of cone resistance. It can be seen from Figure 4.14 – Figure 4.19 that an increase in the coefficient of variation of cone resistance affects the pile base capacities far more than an increase in the vertical scale of fluctuation. The influence of the coefficient of variation of cone resistance is particularly greater in the Koppejan method than in the LCPC method. This has to do with the way the Koppejan method computes the $q_{c,avg}$, which follows the minimum path rule dependent on the q_c profile, whereas the LCPC $q_{c,avg}$ takes the average q_c in its zone of influence and removes the influence of outliers to a certain extent. So, in the case of a high coefficient of variation of cone resistance, the Koppejan method will get vastly different q_c profiles with outliers that will lead to vastly different pile base capacities. The LCPC method dampens that effect by removing outliers that are 30% above or below the average cone resistance in its zone of influence. For small coefficients of variation $(c_v(q_c) \leq 0.15)$ the differences between the LCPC and Koppejan averaging methods are small and they become clearer for large coefficients of variation like 0.45.

5. Conclusions and Recommendations

The aim of this thesis was to describe the vertical spatial variability of a specific sand layer in the Port of Rotterdam and whether the river Meuse had an influence on the vertical spatial variability of that sand layer. Further research was done on the influence of the vertical spatial variability on pile base capacities. By using the results and discussion from the previous chapters, answers to the research questions can be given. The final section of this chapter will give several recommendations to improve this research and recommendations for future research into this topic.

5.1. Conclusions per research question

Which method/model can be used to quantify the spatial variability of the soil in the Kreftenheye and Boxtel Formation, Delwijnen Member in the Port of Rotterdam?

A soil property can be described by its point statistics and spatial statistic. The point statistics are described by the mean and standard deviation while the spatial statistic is described by the scale of fluctuation. The scale of fluctuation is the most frequently used parameter to describe the spatial variability and it can be either in vertical or horizontal directions. Before anything else, the soil layers need to identified as the spatial variability can be seen as a unique property of the soil type.

The most common methods to compute the scale of fluctuation are the simplified method, the autocorrelation fitting method (ACFM) and the semivariogram fitting method (SVFM). The first method should be seen as a rule of thumb method which is only useful for first impressions. The latter two methods are more suitable for a spatial variability analysis. Both ACFM and SVFM are valid methods and any choice between the two methods is dependent on the user's preference.

In this thesis, the SVFM was used as a reference method and it gave out similar vertical scale of fluctuation values as the autocorrelation method but that was dependent on which semivariogram model was chosen. It can happen that one semivariogram model will give a similar value to the autocorrelation method while another model would give an under- or overestimation. Another thing that has happened several times is that during the model fitting process, a vertical scale of fluctuation was computed that was outside of the expected range of 0 – 3 m. So with these points of concern with the SVFM, it is better to use the ACFM to describe the spatial variability in the Port of Rotterdam.

Does the river Meuse have an influence on the spatial variability of the soil? If so, how significant is that influence?

The vertical scales of fluctuation were computed at each site in the Maasvlakte, Botlek and Pernis. By looking at the mean vertical scales of fluctuation, the impression is created that the river Meuse does influence the vertical spatial variability but more investigation is needed to verify whether the Meuse is really responsible for that impression. For example, this impression can be due to sublayers within the Kreftenheye and Boxtel Formation where the Botlek and Pernis contain the younger sublayer of the geological formation and the Maasvlakte contains the older sublayer of the geological formation. Thus local differences within in the geological formation can lead to different scales of fluctuation and the question should be asked whether these sublayers should be included when computing the vertical scale of fluctuation.

The author believes that for designing structures (e.g. quay walls or pile foundations) sublayers should be included when computing the scale of fluctuation unless their scales of fluctuation are outside of the expected range. If it is in the context of geologist research and investigating the influence of geology on the scale of fluctuation, it might be useful to look at

the influence of each sublayer and compare them to the influence of the geological formation as a whole.

So more investigation is needed before one can say that the Meuse has a direct or indirect effect on the vertical spatial variability of soils in the Port of Rotterdam.

How large is the influence of the spatial variability on the pile base capacity of a single foundation pile? And how does it affect the probabilistic design of the foundation pile?

Using random field theory, simulations of the cone resistance data for each site was generated. The simulations required the mean, standard deviation and vertical scale of fluctuation as input parameters. From the simulations the pile base capacities were computed using the LCPC and Koppejan methods and in order to compare the results, the coefficients of variation of pile base capacities $c_v(Q_b)$ were used. Chapter 4.4 shows the results and it is seen that if the vertical scale of fluctuation is large enough it does not affect the $c_v(Q_b)$. The $c_v(Q_b)$ is affected by the vertical scale of fluctuation if it is much smaller than the pile diameter. However, it is the point statistics that have a much larger influence on $c_v(Q_b)$ than the vertical scale of fluctuation.

The Koppejan and LCPC methods give similar results for small values of coefficients of variation of cone resistance. It is only for large coefficients of variation of cone resistance that the Koppejan method shows a larger $c_v(Q_b)$ than the LCPC method. Meaning that the effect of the point statistics are somewhat dampened in the LCPC method compared to the Koppejan method.

For around $\frac{\theta_v}{D} \geq 4-5$, the spatial variability does not play a significant role in the uncertainty of the pile base capacity as that uncertainty becomes roughly constant. This means that for large values of θ_v/D one can afford to use less CPTs in their spatial variability analysis as the estimated vertical scale of fluctuation does not significantly influence the pile base capacity and the probabilistic design of the foundation pile.

For $c_v(q_c) \leq 0.15$, it can be said that the influence of spatial variability is negligible as the uncertainty of the pile base capacity quickly becomes constant. This means that any value of $\theta_v/D \geq 2$ can be used to simulate the cone resistance and it would give you the same uncertainty. This means that only for very small values of θ_v/D one would need to perform a spatial variability analysis and due to $c_v(q_c)$ being small the number of simulations to get a certain level of uncertainty should be small as well, thus saving time and energy.

5.2. Recommendations

The recommendations for improving the research or for future research are mentioned below:

- More CPTs are needed for the Pernis sites as current research uses far less CPTs than the Botlek and Maasvlakte sites. This makes it difficult to make any observations or conclusions due to a lack of cone resistance data. This problem can be solved by lessening the restrictions that were put on CPTs or by performing new tests at the sites.
- One should investigate whether the different vertical scales of fluctuation at the three areas are due to sublayers in a geological formation as an alternative explanation to the river Meuse research question. This is directed toward specific research of a geologist.
- The horizontal scale of fluctuation θ_h should be included in the spatial variability analysis. This research only looks in the vertical direction but an extension to the horizontal direction will give a better picture of the spatial variability at a site. One can measure the horizontal scale of fluctuation along a quay wall where the CPTs are

executed at fixed intervals of e.g. 50 meters. Preferably, the fixed intervals are less than $2\theta_h$.

- To answer the river Meuse research question more sites and more areas are needed. So expand the number of sites per area and add more areas like Europoort and areas that are eastwards of Pernis.
- One can investigate the variability of the vertical scales of fluctuation at sites that are along the river and compare them to sites in the port area. This comes from observing the difference in the coefficients of variation of vertical scales of fluctuation at the Botlek sites.

Bibliography

Abrahamsen, P., Kvernelv, V., & Barker, D. (2018). Simulation Of Gaussian Random Fields Using The Fast Fourier Transform (Fft). ECMOR XVI-16th European Conference on the Mathematics of Oil Recovery,

Ahmadi, M. M., & Robertson, P. K. (2005). Thin-layer effects on the CPT qc measurement. *Canadian Geotechnical Journal, 42*(5), 1302-1317.

Amirmojahedi, M., & Abu-Farsakh, M. (2019). Evaluation of 18 Direct CPT Methods for Estimating the Ultimate Pile Capacity of Driven Piles. *Transportation Research Record: Journal of the Transportation Research Board, 2673*(9), 127-141. https://doi.org/10.1177/0361198119833365

Bombasaro, E., & Kasper, T. (2016). Evaluation of spatial soil variability in the Pearl River Estuary using CPTU data. *Soils and Foundations, 56*(3), 496-505. https://doi.org/10.1016/j.sandf.2016.04.015

Bosch, J. (2003). Beschrijving lithostratigrafische eenheid. Formatie van Peize. *Nederlands Instituut voor Toegepaste Geowetenschappen TNO. Utrecht*.

Bouayad, D. (2017). Assessment of Sandy Soil Variability Based on CPT Data. *Procedia Engineering, 175*, 310-315. https://doi.org/10.1016/j.proeng.2017.01.033

Busschers, F., & Weerts, H. (2003). Beschrijving lithostratigrafische eenheid. Formatie van Kreftenheye. *Nederlands Instituut voor Toegepaste Geowetenschappen TNO. Utrecht*.

Bustamante, M., & Gianeselli, L. (1982). Pile bearing capacity prediction by means of static penetrometer CPT. Proceedings of the 2-nd European symposium on penetration testing,

Cai, Y., Bransby, F., Gaudin, C., & Uzielli, M. (2021). A framework for the design of vertically loaded piles in spatially variable soil. *Computers and Geotechnics, 134*, 104140. https://doi.org/10.1016/j.compgeo.2021.104140

Cami, B., Javankhoshdel, S., Phoon, K.-K., & Ching, J. (2020). Scale of fluctuation for spatially varying soils: Estimation methods and values. *ASCE-ASME Journal of Risk and Uncertainty in Engineering Systems, Part A: Civil Engineering, 6*(4), 03120002.

Ching, J., Wu, T.-J., Stuedlein, A. W., & Bong, T. (2018). Estimating horizontal scale of fluctuation with limited CPT soundings. *Geoscience Frontiers, 9*(6), 1597-1608.

Civieltechnisch Centrum Uitvoering Research en Regelgeving. (1999). *CUR Geotechnical Exchange Format for CPT-Data*. CUR.

Corotis, R. B., Azzouz, A. S., & Krizek, R. J. (1975). Statistical evaluation of soil index properties and constrained modulus. *[No source information available]*, 273-293.

de Boorder, M. (2019). Development of a new CPT averaging technique and review of existing CPT based methods for the calculation of total pile capacity.

Eslami Kenarsari, A., Jamshidi Chenari, R., & Eslami, A. (2013). Characterization of the correlation structure of residual CPT profiles in sand deposits. *International Journal of Civil Engineering, 11*(1), 29-37.

Fenton, G. A. (1999). Estimation for stochastic soil models. *Journal of Geotechnical and Geoenvironmental Engineering, 125*(6), 470-485.

Fenton, G. A., & Griffiths, D. V. (2008). *Risk assessment in geotechnical engineering*. John Wiley & Sons. http://catdir.loc.gov/catdir/enhancements/fy0811/2007044825-t.html http://catdir.loc.gov/catdir/enhancements/fy0811/2007044825-d.html http://swbplus.bsz-bw.de/bsz288497163cov.htm

Fenton, G. A., & Vanmarcke, E. H. (1990). Simulation of Random Fields via Local Average Subdivision. *Journal of Engineering Mechanics, 116*(8), 1733-1749. https://doi.org/10.1061/(ASCE)0733-9399(1990)116:8(1733)

Fenton, G. A. M. A. (1994). Error Evaluation of Three Random-Field Generators. *Journal of Engineering Mechanics, 120*(12), 2478-2497.

Gunnink, J., Maljers, D., Van Gessel, S., Menkovic, A., & Hummelman, H. (2013). Digital Geological Model (DGM): a 3D raster model of the subsurface of the Netherlands. *Netherlands Journal of Geosciences, 92*(1), 33-46.

Hicks, M. A. (2014). Application of the random finite element method. *ALERT Doctoral School*, 181.

Hicks, M. A., & Samy, K. (2002a). Influence of heterogeneity on undrained clay slope stability. *Quarterly Journal of Engineering Geology and Hydrogeology, 35*(1), 41-49.

Hicks, M. A., & Samy, K. (2002b). Reliability-based characteristic values: a stochastic approach to Eurocode 7. *Ground Engineering, 35*(12).

Hummelman, H., Maljers, D., Menkovic, A., Reindersma, R., Vernes, R., & Stafleu, J. (2019). Totstandkomingsrapport Hydrogeologisch Model (REGIS II). *TNO report, 11654*, 95.

Jaksa, M., Brooker, P., & Kaggwa, W. (1996). The influence of spatial variability on the design of pile foundations. Proceedings of the 7th Australia New Zealand Conference on Geomechanics, Adelaide,

Jefferies, M. G., & Davies, M. P. (1993). Use of CPTU to estimate equivalent SPT N 60. *Geotechnical Testing Journal, 16*(4), 458-468.

Jonkman, S. N., Steenbergen, R. D. J. M., Morales-Napoles, O., Vrouwenvelder, A. C. W. M., & Vrijling, J. K. (2015). *Probabilistic Design: risk and reliability analysis in Civil Engineering Lecture notes CIE4130*. TU Delft.

Kim, D. A. M. A., & Salgado, R. F. A. (2013). Reliability Analysis of Load and Resistance Factor Design of Slopes. *Journal of Geotechnical and Geoenvironmental Engineering, 140*(1), 57-73.

Kok-Kwang, P., & Kulhawy, F. H. (1999). Characterization of geotechnical variability. *Canadian Geotechnical Journal, 36*(Part 4), 612-624.

Kombrink, H., Doornenbal, J., Duin, E., Den Dulk, M., Ten Veen, J., & Witmans, N. (2012). New insights into the geological structure of the Netherlands; results of a detailed mapping project. *Netherlands Journal of Geosciences, 91*(4), 419-446.

Lacasse, S., & Nadim, F. (1996). Uncertainties in Characterising Soil Properties. Uncertainty in the Geologic Environment: from Theory to Practice,

Lengkeek, H., De Greef, J., & Joosten, S. (2018). CPT based unit weight estimation extended to soft organic soils and peat. Proceedings of the 4th international symposium on cone penetration testing (CPT'18),

Li, D.-Q., Xiao, T., Zhang, L.-M., & Cao, Z.-J. (2019). Stepwise covariance matrix decomposition for efficient simulation of multivariate large-scale three-dimensional random fields. *Applied Mathematical Modelling, 68*, 169-181. https://doi.org/10.1016/j.apm.2018.11.011

Liu, C. N., & Chen, C.-H. (2010). Spatial correlation structures of CPT data in a liquefaction site. *Engineering Geology, 111*(1-4), 43-50. https://doi.org/10.1016/j.enggeo.2009.12.002

Lunne, T., Robertson, P. K., & Powell, J. J. M. (1997). *Cone penetration testing in geotechnical practice* (1st ed. ed.). Blackie Academic & Professional.

Mayne, P. (2006). In-situ test calibrations for evaluating soil parameters. Characterisation and Engineering Properties of Natural Soils–Proceedings of the Second International Workshop on Characterisation and Engineering Properties of Natural Soils: Taylor & Francis,

Nadim, F. (2015). Accounting for uncertainty and variability in geotechnical characterization of offshore sites. Proc of the 5 th Int. Symp. Geotechnical Safety and Risk,

Nie, X., Zhang, T., Huang, H., Liu, Z., & Lacasse, S. (2015). Scale of fluctuation for geotechnical probabilistic analysis scale of fluctuation for geotechnical probabilistic analysis. Proc. of the 5th International Symposium on Geotechnical Safety and Risk,

Normcommissie-351-006-Geotechniek. (2019). *NEN-EN 1997-1 Eurocode 7: Geotechnical design - Part 1: General Rules*. Nederlandse Normalisatie-Instituut.

Onyejekwe, S., Kang, X., & Ge, L. (2016). Evaluation of the scale of fluctuation of geotechnical parameters by autocorrelation function and semivariogram function. *Engineering Geology, 214*, 43-49. https://doi.org/https://doi.org/10.1016/j.enggeo.2016.09.014

Popescu, R., Prevost, J. H., & Deodatis, G. (1998). Spatial variability of soil properties: two case studies. *Geotechnical special publication*(75 I), 568-579.

Port of Rotterdam Authority. (2019). *Port of Rotterdam. Highlights of the 2019 Annual Report*. Port of Rotterdam Authority. https://www.portofrotterdam.com/sites/default/files/annual-report-highlights-port-of-rotterdam-2019.pdf?token=bavka0aZ

Ravalec, M. l. L., Noetinger, B. t., & Hu, L. Y. (2000). The FFT Moving Average (FFT-MA) Generator: An Efficient Numerical Method for Generating and Conditioning Gaussian Simulations. *Mathematical Geology, 32*(6), 701-723. https://doi.org/10.1023/A:1007542406333

Robertson, P. K. (1990). Soil classification using the cone penetration test. *Canadian Geotechnical Journal, 27*(1), 151-158. https://doi.org/10.1139/t90-014

Robertson, P. K. (2009). Interpretation of cone penetration tests—a unified approach. *Canadian Geotechnical Journal, 46*(11), 1337-1355.

Robertson, P. K., & Cabal, K. (2010). Estimating soil unit weight from CPT. 2nd International Symposium on Cone Penetration Testing,

Robertson, P. K., & Cabal, K. (2015). *Guide to Cone Penetration Testing for Geotechnical Engineering, 6th Edition*. Gregg Drilling & Testing, Incorporated.

Robertson, P. K., Campanella, R. G., Gillespie, D., & Greig, J. (1986). Use of piezometer cone data. Use of in situ tests in geotechnical engineering,

Rollins, K. M., Miller, N. P., & Hemenway, D. (1999). Evaluation of Pile Capacity Prediction Methods Based on Cone Penetration Testing Using Results from I-15 Load Tests. *Transportation Research Record: Journal of the Transportation Research Board, 1675*(1), 40-50. https://doi.org/10.3141/1675-06

Salgado, R., Ganju, E., & Prezzi, M. (2019, 2019/01/01/). Site variability analysis using cone penetration test data. *Computers and Geotechnics, 105*, 37-50. https://doi.org/https://doi.org/10.1016/j.compgeo.2018.08.001

Schokker, J., de Lang, F., Weerts, H., den Otter, C., & Passchier, S. (2005). Beschrijving lithostratigrafische eenheid. Formatie van Boxtel. *Nederlands Instituut voor Toegepaste Geowetenschappen TNO. Utrecht*.

Stafleu, J., Maljers, D., Busschers, F., Gunnink, J., Schokker, J., Dambrink, R., Hummelman, H., & Schijf, M. (2012). GeoTop modellering. *TNO report, 10991*.

Tehrani, F., Arshad, M., Prezzi, M., & Salgado, R. (2018). Physical modeling of cone penetration in layered sand. *Journal of Geotechnical and Geoenvironmental Engineering, 144*(1). https://doi.org/10.1061/(ASCE)GT.1943-5606.0001809

TNO-GSN. (2021). *Walcheren Member*. TNO – Geological Survey of the Netherlands. Retrieved 21 April from http://www.dinoloket.nl/en/stratigraphic-nomenclature/walcheren-member

Tol, A. F. v. (2006). *Funderingstechnieken Collegedictaat CTB1410(67)*. TU Delft.

Uzielli, M., Lacasse, S., Nadim, F., & Phoon, K. K. (2006). Soil variability analysis for geotechnical practice. *Characterization and engineering properties of natural soils, 3*, 1653-1752.

Uzielli, M., Vannucchi, G., & Phoon, K. K. (2005). Random field characterisation of stress-normalised cone penetration testing parameters. *Geotechnique, 55*(1), 3-20. https://doi.org/10.1680/geot.2005.55.1.3

Van Mierlo, J., & Koppejan, A. (1952). Lengte en draagvermogen van heipalen. *Bouw, 3*, 1952.

Vanmarcke, E. H. (1977). Probabilistic modeling of soil profiles. *Journal of the Geotechnical Engineering Division, 103*(11), 1227-1246.

Vanmarcke, E. H. (1983). *Random Fields: Analysis and Synthesis*. MIT Press.

Varkey, D., Hicks, M., van den Eijnden, A. P., & Vardon, P. (2020). On characteristic values for calculating factors of safety for dyke stability. *Géotechnique Letters, 10*(2), 353-359.

Vernes, R., Van Doorn, T. H., Bierkens, M., Van Gessel, S., & De Heer, E. (2005). *Van gidslaag naar hydrogeologische eenheid: toelichting op de totstandkoming van de dataset REGIS II*. TNO.

Viviescas, J. C., Griffiths, D., & Osorio, J. P. (2022). Geological influence on the spatial variability of soils. *International Journal of Geotechnical Engineering, 16*(3), 382-390.

Weerts, H. (2003). Beschrijving lithostratigrafische eenheid. Formatie van Naaldwijk. *Nederlands Instituut voor Toegepaste Geowetenschappen TNO. Utrecht*.

Weerts, H., & Busschers, F. (2003a). Beschrijving lithostratigrafische eenheid. Formatie van Echteld. *Nederlands Instituut voor Toegepaste Geowetenschappen TNO. Utrecht*.

Weerts, H., & Busschers, F. (2003b). Beschrijving lithostratigrafische eenheid. Formatie van Nieuwkoop. *Nederlands Instituut voor Toegepaste Geowetenschappen TNO. Utrecht*.

Westerhoff, W., & Weerts, H. (2003). Beschrijving lithostratigrafische eenheid. Formatie van Waalre. *Nederlands Instituut voor Toegepaste Geowetenschappen TNO. Utrecht*.

Zhang, G., Robertson, P., & Brachman, R. W. (2002). Estimating liquefaction-induced ground settlements from CPT for level ground. *Canadian Geotechnical Journal, 39*(5), 1168-1180.

Zhang, J.-Z., Phoon, K. K., Zhang, D.-M., Huang, H.-W., & Tang, C. (2021). Novel approach to estimate vertical scale of fluctuation based on CPT data using convolutional neural networks. *Engineering Geology, 294*. https://doi.org/10.1016/j.enggeo.2021.106342

Zhu, Y.-X., Zheng, S., Cao, Z.-J., & Li, D.-Q. (2019). Revisiting the relationship between scale of fluctuation and mean cross distance. 13th International Conference on Applications of Statistics and Probability in Civil Engineering, ICASP 2019,

A. Reliability methods

The reliability methods follow a general format of a limit state Z and the limit state function equation below:

$$Z = R - S \tag{A.1}$$

$$g(\underline{X}) = Z = 0 \tag{A.2}$$

where:

R = resistance variable

S = load variable

$g(\underline{X})$ = limit state function

$\underline{X}$ = vector which contains n basic variables (e.g. load, resistance, model uncertainty)

The limit state is the condition in which the structure can no longer perform and fulfill its requirements. So the probability of failure P_f is usually seen as $P_f = P(Z < 0) = P(R < S)$. From the limit state function the design point can be found which is the point where failure is most probable, thus where $g(\underline{X}) = 0$ with the highest probability density.

Level 0 methods (deterministic methods)

The level 0 methods are deterministic methods in which one uses deterministic or nominal values for all the resistance and load variables. As such, the calculations become simple and the limit state function $g(\underline{X})$ can usually be solved analytically. If one were to repeat the calculations, the output value would not change. Thus, from the deterministic methods one receives a single factor of safety (FoS) as it is:

$$FoS = \frac{R_{nom}}{S_{nom}} \tag{A.3}$$

where R_{nom} is the nominal or deterministic value for the resistance variable and S_{nom} being the nominal or deterministic value for the load variable. However that single FoS does not tell anything about the probability of failure of a structure as it only gives information about the limit load, the maximum load that a structure can take before it fails.

Level I methods (semi-probabilistic methods)

The level 1 methods are semi-probabilistic as they recognize that the variables R and S are stochastic variables with probability distributions but characteristic values are used in the calculations and they correspond to a low percentile (e.g. 5%) in the resistance probability distributions and a high percentile (e.g. 95%) in the load probability distributions. Partial safety factors that are based on level II calculations, are used as well. The requirement for a safe design is then:

$$\frac{R_k}{\gamma_R} > \gamma_S S_k \tag{A.4}$$

where R_k, S_k are the characteristic resistance and load values and γ_R, γ_S being the partial safety factors. The partial safety factors are calculated from the probabilistic influence factors α which show the influence the variables have on the reliability, the design point values and the mean and standard deviation of the probability distributions.

Level II methods (simplified probabilistic methods)

The level II methods are approximation methods. In the level II methods, the load and resistance variables are stochastic with their mean and covariance matrix being used to determine the failure probability. The level II methods require the variables to be normally distributed or in the case of non-normally distributed variables, to transform them into normal distributions. From that, the limit state Z is also normally distributed and the failure probability can be determined by using the standard normal distribution:

$$P(Z < 0) = \Phi\left(\frac{0 - \mu_Z}{\sigma_Z}\right) = \Phi\left(-\frac{\mu_Z}{\sigma_Z}\right) = \Phi(-\beta) \quad \textbf{(A.5)}$$

where:

$\Phi(\dots)$ = cumulative distribution function (cdf) of a standard normal distribution

μ_Z = mean of Z

σ_Z = standard deviation of Z

β = reliability index

Using a technique called First Order Reliability Method (FORM), the joint probability density function of R and S is simplified and the limit state function is linearized to reduce the computation time. The limit state function is linearized in the design point and the FORM is an iterative method. In the case of a non-linear limit state function, the limit state function can be linearized using a Taylor expansion around the mean of each variable. From that, the probability of failure can be determined and more information about the FORM if the variables were non-normally distributed, a non-linear limit state function or variables that are dependent, can be found in the lecture notes of Jonkman et al. (2015).

B. Dutch subsurface

This appendix gives more background information about DINOloket, the subsurface models and the geological formations that are present in the Port of Rotterdam.

B.1. DINOloket and subsurface models

The Data and Information on the Dutch Subsurface (DINO) is a database containing the geological data for shallow and deep geology in the Netherlands. It consists not only of CPT data but also borehole data, groundwater data and vertical electrical soundings. The database is maintained by the Geological Survey of the Netherlands (GDN) which is an organization that is part of an independent research organization, the Netherlands Organization for Applied Scientific Research (TNO) and the DINO database can be accessed freely through the website *www.DINOloket.nl*. Currently the DINO database is being developed with the Subsurface Key Register (BRO) which is an initiative of the Dutch Interior Ministry to centralized the public data about the Dutch subsurface from the subsurface databases of various organizations.

Through DINOloket, one cannot only access the subsurface data but it can also look at the subsurface models. These subsurface models can give an estimate about the geological layers in the Netherlands. The subsurface models are:

- BRO DGM
- BRO REGIS II
- BRO GeoTop
- DGM – deep

BRO DGM

The BRO Digital Geological Model (DGM) is a 3D raster model for the shallow subsurface of the Netherlands which is the subsurface up to a depth of 500 meters. It was first introduced by Gunnink et al. (2013) as a model to determine the geological units of the subsurface using the lithostratigraphic classification of the Netherlands. The model and its geological units are limited to the Cenozoic era and more specifically the Neogene and Quaternary deposits in the Netherlands.

The model is created from onshore borehole data as a primary source with supplementary data as a secondary source for the creation of the 3D model. Among the supplementary data there is trend surfaces which is used to help the interpolation of borehole data with the range of forms that can be found in geological surfaces. The interpolation is done for the bottom surfaces also known as basal surfaces of a geological unit on 100 x 100 meter raster cells. This is done because “the basal surface is formed by geological processes uniquely related to the unit. Interpolation of the top surface of a unit is less suitable because the top is also the result of later geological processes, unrelated to the deposition of the unit.” (Gunnink et al., 2013, pp. 39-40). The interpolated basal surfaces are then stacked together in a stratigraphically consistent way to create horizontal layers and a 3D model of the subsurface.

The DGM is merely a regional scale model and it serves as the framework for future subsurface models such as REGIS II and GeoTop.

BRO REGIS II

BRO REGIS II is a hydrogeological model with DGM serving as its framework. It follows the same procedure as DGM. The difference from DGM is that it does not stop with the geological units but rather the geological units are then converted into hydrogeological units. A hydrogeological unit is defined as “a rock body that is based on petrography, texture or

structure exhibits uniform hydrogeological properties within a defined bandwidth" (Vernes et al., 2005, pp. 15-16). The hydrogeological properties in question are: hydraulic conductivity, transmissivity and hydraulic resistance. Like BRO DGM, BRO REGIS II is a layer model in which the hydrogeological units that share the same properties are stacked together in a horizontal layer and from that the 3D model is built.

According to Hummelman et al. (2019), BRO REGIS II is only applicable on provincial or municipal scale and it should serve as a framework for local hydrogeological models if it is supplemented with local borehole data, geometry and hydraulic parameters. The main purpose for BRO REGIS II is regional groundwater modelling and it is used as such in the Netherlands.

BRO GeoTop

Like BRO REGIS II, BRO GeoTop uses BRO DGM as a framework. BRO GeoTop uses a voxel model to create its 3D model. The procedure as explained by Stafleu et al. (2012) is similar to BRO DGM as it determines the geological units from borehole data. After that the top and base surfaces of the geological unit are constructed and then converted into voxels (cells). The voxels have the dimensions 100 x 100 x 0.5 meter with the 100 meters being horizontal and 0.5 meter being vertical. Each voxel contains not only the geological unit but also information about the lithological classes like sand, clay and silt. For determining the lithological class within a voxel, a stochastic simulation is performed and the lithological class with the highest probability is filled into the voxel. This type of modelling using voxels captures the heterogeneity and variation of the soil better than the layer models used in BRO REGIS II and BRO DGM.

The modelling of GeoTop requires several data sources such as borehole data and CPT soundings from the DINO database, DGM, REGIS II and other sources. The CPT soundings are used to derive the probabilities for the lithological classes. The DGM model is used for selecting the main geological units that are going used. Stafleu et al. (2012) give a more thorough explanation about the modelling.

Due to the quality check and filter on the borehole data and CPT soundings, the GeoTop model is valid for the Dutch onshore subsurface up to a depth of 50 meters NAP. As it tries to contain as much information as possible, the GeoTop model refines the BRO DGM and REGIS II models, making it a more detailed and more accurate model than the other Dutch subsurface models.

DGM – deep

BRO DGM, BRO REGIS II and BRO GeoTop are models which are limited to the shallow subsurface so they only look at the deposits from Cenozoic era. DGM – deep uses an entirely different model as it looks at the deposits from the Paleozoic, Mesozoic and Cenozoic eras. So DGM – deep as the name implies looks at the deep subsurface.

Kombrink et al. (2012) use the modelling workflow for oil and gas exploration, seismic data and offshore wells. The logs of the wells were chosen based on total depth, stratigraphic significance, spatial distribution and presence of digital well logs. The well logs were mainly used for the lithostratigraphic subdivision. The seismic data in time domain is used for interpreting the horizons and faults and converted into the depth domain with a velocity model. Kombrink et al. (2012) created this model mainly as part of an update on the Netherlands Continental Shelf.

B.2. Geological layers

Anthropogenic deposits

This layer consists of heterogeneous deposits and it is natural sediments applied as filling material like marine and fluvial sand used as filling sand.

Naaldwijk Formation, Walcheren Member
This formation is from the Holocene period and it is formed in a marine and lagoon environment. It consists of alternations of very fine to very coarse sand (105 – 420 µm), and calcareous formations of low to high silty clay. The Naaldwijk formation usually has clay layers with a few sand deposits and sand layers with a lot of clay deposits and the clay under the GWT is usually weak with the sand layers consisting of loose sand. Due to large regional differences in lithology, the Naaldwijk formation can be subdivided into four members: the Wormer Member, the Walcheren Member, the Zandvoort Member and the Schoorl Member.

Weerts (2003) describes that the Walcheren Member consists of fine to medium sands (105 – 210 µm), clayey to silty sands and medium to very silty clay and sandy clay. The Walcheren Member is usually restricted to the west of the Netherlands and it is formed in "estuarine or back-barrier tidal basin, established following breaching of a closed barrier coast, including channel (shelly sand), tidal flat and mudflat (sand and mud), and tidal marsh (mud and organics)" (TNO-GSN, 2021).

Dependent on its geographical location, it can be subdivided into: the Almere Bed, the Zuiderzee Bed, the IJsselmeer Bed and the IJe Bed.

Naaldwijk Formation, Wormer Member
Description about the Naaldwijk Formation can be read above. Weerts (2003) describes the lithology in the Wormer Member as very fine to medium fine calcareous sand (105 – 210 µm), and medium to very silty clay or sandy clay.

Echteld Formation
This formation is from the Holocene period and it is formed from the meandering fluvial deposits of the rivers Rhine and Meuse. This results in a sediment deposits in which sand deposits and clay deposits appear close to each other. According to Weerts and Busschers (2003a) this formation is known for its large internal lithological heterogeneity but within the heterogeneity the lithological units can be distinguished and it is fairly homogenous. The lithological units are sandy to low silty calcareous clay and very fine to very coarse sand (63 – 2000 µm).

Weerts and Busschers (2003a) comment that the regional lithological differences are the decreasing grain sizes and gravel content as one moves from east to west and the increasing thickness of the formation starting from the German border and moving to the west.

Nieuwkoop Formation, Basisveen Bed
This formation is from the Holocene period and locally it can be from Late Pleistocene and its lithological unit is peat. In other words, the Nieuwkoop formation is a peat layer and it is formed as a result of the rise of groundwater during the Holocene period. The rising groundwater combined with rain created a marsh and swamp environment in which peat is formed. The regional lithological differences was because "in the river plain, the peat is often clayey and it is highly fragmented due to fluvial erosion" (Weerts & Busschers, 2003b). The Nieuwkoop Formation can be subdivided into four different units: Griendtsveen Member, Flevomeer Bed, Hollandveen Member and Basisveen Bed.

The Basisveen Bed describes the peat that is between the top of the Pleistocene deposits and the base of the Naaldwijk Formation. So above the Basisveen Bed you have the Naaldwijk Formation and below the Basisveen Bed you have the Pleistocene deposits. The

Basisveen Bed can be found in the coastal and river plains in the western and northern Netherlands.

Kreftenheye Formation, Wijchen Bed
This formation is from the late Pleistocene to early Holocene period and it is formed by the sediment deposits of the braided and meandering rivers like the Rhine and its precursors. So it falls under the fluvial domain. The formation consists of very fine to very coarse sands (63 – 2000 µm), fine to very coarse gravel (2 – 63 mm) and locally there can be some very thin peat layers. Dependent on its geographical location, the Kreftenheye Formation can be subdivided into: the Wijchen Bed, the Ockenburg Member, the Zutphen Member, the Twello Member and the Well Member.

Busschers and Weerts (2003) explain that the Wijchen Bed consists of silty to sandy clay, non-calcareous. This clayey part can often be found on the top of Kreftenheye Formation and is the result of the clay and sand of the Echteld Formation or Naaldwijk Formation or the peat of the Nieuwkoop Formation being present above the Kreftenheye Formation.

Peize and Waalre Formation
The Peize Formation is from the late Pleistocene to early Pleistocene period and Westerhoff and Weerts (2003) describe it to be formed largely from fluvial deposits from the Baltic river system and the bottom of the formation contain non calcareous fine sands that are shallow marine deposits. The formation consists of very fine to very coarse sand (105 – 2000 µm), fine to medium coarse gravel (2 – 6 mm) and subordinate low to medium silty clay beds. Due to being in Southern Netherlands, the Peize Formation sits on top of the clay and sand of the Waalre Formation and the transition between the two formations is gradual. The distinction between the two formations is done on the basis of the sand color (white, light grey for Peize and light brown for Waalre), the lime content and the gravel composition.

The Waalre Formation is from the late Pliocene to early Pleistocene period and Bosch (2003) describes it to be formed from fluvial and estuarine deposits of the river Rhine. The formation consists of very fine to very coarse sand (63 – 2000 µm), very sandy to low silty clay which are horizontally layered and sporadic peat layers.

B.3. Geo Exchange Format files

The data of the CPTs are downloaded from DINOloket as Geo Exchange Format (GEF) files. More specifically, the CPT data is downloaded as GEF-CPT-Report. The GEF is the language structure used for storing and exchanging geotechnical information. The distinction between GEF and GEF-CPT-Report is that a GEF file contains data obtained from an arbitrary test on soil while the GEF-CPT-Report refers to the fact that it is a GEF file but it only contains data obtained from a CPT.

The Civieltechnisch Centrum Uitvoering Research en Regelgeving (1999) wrote a manual for writing a GEF-CPT-Report. Their format was made to become the new standard for GEF-CPT-Report and it is also used in the GEF files obtained from DINOloket. More information about the format of the GEF-CPT-Report can be found in the GEF-CPT manual of Civieltechnisch Centrum Uitvoering Research en Regelgeving (1999).

All the GEF-CPT-Report files contain measurements of the penetration length, cone resistance q_c, friction resistance f_s, the RD coordinates of the CPT which is the Dutch coordinate system and the corrected depth measured below a fixed surface which is the ground level.

The Dutch (RD) coordinate system differs from the latitude/longitude system as it is a distance based system and not measured in degrees but in meters. It is also known as the

Amersfoort projection as the central point of the RD coordinate system is the Onze-Lieve-Vrouwetoren, a church tower in Amersfoort which has the coordinates x = 155 km, y = 463 km. The RD coordinate system is the projection system code: EPSG 28992.

The corrected depth is the vertical length of the path that the cone penetrometer follows, so depth only has positive values with meters as its unit. Thus the corrected depth needs to be converted to a depth with respect to the national standard datum NAP. This is simply done by subtracting the depth values from the ground level elevation. The ground level elevation is also reported in the GEF-CPT-Report file. Figure B.1 shows the relationship between the cone penetration length, corrected depth and elevation.

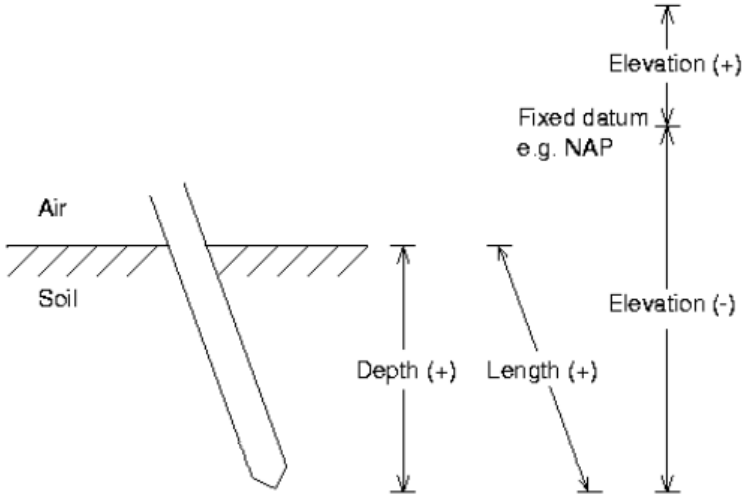

Figure B.1: Relation between cone penetration length, corrected depth and elevation. Source: Civieltechnisch Centrum Uitvoering Research en Regelgeving (1999)

C. Results preparation stage

This appendix contains the figures and tables of the intermediate steps of the spatial variability analysis for all groups and individual CPTs. The tables and figures are following the order that is prescribed in the methodology.

C.1. CPT data

This section summarizes the CPT data with their CPT ID, site ID and x and y coordinates. The x and y coordinates are in the Dutch coordinate system which is codified as EPSG 28992. The Maasvlakte site M2 had two sublayers and the CPTs are divided into the upper sublayer with site ID “2 (0)” and the lower sublayer with site ID “2 (1)”. Also it can be for site M2 that the same CPT is mentioned twice but different parts of the CPT profile is used due to the existence of the sublayers.

Maasvlakte

CPT ID	Site ID	x coordinate	y coordinate	CPT ID	Site ID	x coordinate	y coordinate
CPT000000130993	4	61241.82	444149.23	CPT000000156212	3	58734.8	440114.29
CPT000000132169	4	61416.66	444047.45	CPT000000156214	1	59857.09	443342.19
CPT000000132692	4	61385.51	444104.25	CPT000000156222	1	59858.76	443317.41
CPT000000132746	4	61044.96	444195.17	CPT000000156227	3	58575.54	439989.06
CPT000000132990	4	61288.53	444130.78	CPT000000156228	1	59870.65	443192.99
CPT000000134189	4	62506.35	443603.2	CPT000000156233	1	59867.68	443217.89
CPT000000140082	4	61114.17	444226.28	CPT000000156249	1	59900.63	443195.63
CPT000000140543	4	61836.69	443996.07	CPT000000156256	1	59857.13	443364
CPT000000142698	4	61602.44	443973.62	CPT000000156275	1	59898.01	443220.18
CPT000000143152	4	62373.71	443680.27	CPT000000156451	2 (0)	64602	439709
CPT000000146237	4	62124.62	443798.1	CPT000000156452	2 (1)	64443	439652
CPT000000147186	4	61078.15	444222.83	CPT000000156458	2 (1)	64534	439685
CPT000000147306	4	62132.1	443749.4	CPT000000156460	2 (1)	64419	439643
CPT000000155990	3	58414.45	439765.86	CPT000000156466	2 (1)	64672	439732
CPT000000156016	3	58502.01	439822.6	CPT000000156472	2 (0)	64396	439636
CPT000000156041	3	59016.78	440528.13	CPT000000156475	2 (0)	64488	439670
CPT000000156058	3	58969.19	440410.37	CPT000000156476	2 (1)	64078	439526
CPT000000156091	3	58450.71	439830.38	CPT000000156482	2 (1)	64511	439676
CPT000000156106	3	58398.06	439691.16	CPT000000156491	2 (0)	64373	439628
CPT000000156120	3	59351.69	440957.57	CPT000000156494	2 (0)	64464	439661
CPT000000156129	3	59093.6	440654.86	CPT000000156498	2 (1)	64625	439718
CPT000000156130	1	59902.77	443170.72	CPT000000156499	2 (1)	64268	439590
CPT000000156135	3	58856.75	440271.04	CPT000000156512	2 (0)	64579.53	439701
CPT000000156143	3	59460.85	441092.06	CPT000000156512	2 (1)	64579.53	439701
CPT000000156144	1	59872.22	443168.07	CPT000000156517	2 (1)	64557	439692
CPT000000156145	3	59107.22	440587.33	CPT000000156519	2 (1)	64127	439543
CPT000000156159	1	59873.85	443158.35	CPT000000156525	2 (0)	64222	439572
CPT000000156167	3	58759.87	440225.77	CPT000000156527	2 (1)	64658	439725
CPT000000156180	1	59896.26	443245.44	CPT000000156533	2 (0)	64173	439559
CPT000000156191	1	59905.33	443141.64	CPT000000156533	2 (1)	64173	439559
CPT000000156196	3	58940.53	440460.52				

Table C.1: CPTs used in the Maasvlakte.

Botlek

CPT ID	Site ID	x coordinate	y coordinate	CPT ID	Site ID	x coordinate	y coordinate
CPT000000087531	1	81056.14	433860.78	CPT000000140531	3	80988.27	432352.24
CPT000000087532	1	81029.61	433876.2	CPT000000140632	3	80964.95	432451.24
CPT000000091781	2	80958.49	433024.25	CPT000000140863	4	79433.59	434690.97
CPT000000091782	2	81007.43	433116.8	CPT000000141556	4	79690.11	434631.28
CPT000000091784	2	80964.2	433010.72	CPT000000141676	4	79642.93	434645.83
CPT000000091785	2	80994.57	433052.79	CPT000000141902	3	80947.6	432509.41

CPT000000091786	2	80999.6	433074.05	CPT000000142443	4	79451.16	434704.54
CPT000000091790	2	81035.16	433229.53	CPT000000142481	4	79403.27	434719.5
CPT000000091791	2	81043.98	433275.45	CPT000000143085	3	80982.07	432518.57
CPT000000091795	2	81003	433095.22	CPT000000143723	4	79594.43	434660.48
CPT000000091799	2	81039.34	433252.7	CPT000000145368	3	80981.71	432386.31
CPT000000091800	2	80975.24	432990.29	CPT000000145450	4	79414.55	434670.61
CPT000000091801	2	81050.42	433297.48	CPT000000145558	3	81051.47	432259.61
CPT000000091804	2	81020.2	433183.28	CPT000000145626	4	79786.4	434601.67
CPT000000091806	2	81016.25	433160.94	CPT000000145634	4	79431.1	434709.42
CPT000000091807	2	80981.19	433044.33	CPT000000145998	4	79737.8	434616.62
CPT000000091808	2	81012	433138.69	CPT000000146636	4	79498.95	434689.79
CPT000000091809	2	81040.04	432988.74	CPT000000146786	4	79365.68	434685.52
CPT000000091810	2	80980.62	432967.05	CPT000000146869	4	79355.48	434734.05
CPT000000091811	2	80997.62	432977.6	CPT000000146928	3	81010.48	432420.43
CPT000000091814	2	81018.96	432983.12	CPT000000147207	3	81020.53	432377.5
CPT000000097366	1	80997.85	433714.32	CPT000000147221	3	81025.59	432356.2
CPT000000130642	4	79296.9	434714.77	CPT000000147556	3	81001.49	432446.12
CPT000000130968	3	81018.39	432240.15	CPT000000147882	3	80963.15	432405.55
CPT000000130982	3	81032.06	432332.05	CPT000000156354	1	80972	433767
CPT000000131904	3	81057.94	432235.46	CPT000000156355	1	80926	433514
CPT000000132170	3	80993.82	432366.36	CPT000000156358	1	80920	433490
CPT000000132368	4	79679.8	434597.9	CPT000000156364	1	80940	433562
CPT000000132891	3	81045	432283.76	CPT000000156370	1	80935	433538
CPT000000133208	4	79746.31	434603.1	CPT000000156372	1	80944	433587
CPT000000133214	4	79558.05	434626.94	CPT000000156376	1	80961	433668
CPT000000133221	4	79344.94	434700.22	CPT000000156384	1	80966	433725
CPT000000133522	4	79653.53	434597.49	CPT000000156388	1	80988	433815
CPT000000133821	4	79631.72	434612.47	CPT000000156395	1	80951	433611
CPT000000133845	4	79560.28	434660.11	CPT000000156401	1	80955	433637

Table C.2: CPTs used in the Botlek.

Pernis

CPT ID	Site ID	x coordinate	y coordinate	CPT ID	Site ID	x coordinate	y coordinate
CPT000000130932	3	89364.37	434631.15	CPT000000144494	1	88114.27	432715.78
CPT000000130956	3	89220.62	434583	CPT000000144681	1	87328.96	432829.27
CPT000000133438	3	89268.54	434599.05	CPT000000145890	1	88452.62	432623.96
CPT000000140125	3	89316.45	434615.1	CPT000000145969	1	87354.25	432820.16
CPT000000140814	1	87319.86	432811.18	CPT000000150567	1	87499	432780
CPT000000141380	2	87278.75	433477.16	CPT000000150577	1	87614	432725
CPT000000141532	2	87245.99	433496.4	CPT000000155906	4	90935.93	433866.02
CPT000000141803	2	87370.76	433339.56	CPT000000155919	4	90983.2	433852.2
CPT000000142179	1	87341.6	432803.64	CPT000000155925	4	90959.9	433859.13
CPT000000142322	2	87326.48	433428.06	CPT000000155932	4	90911.86	433873.04
CPT000000143102	2	87338.33	433405.39	CPT000000155992	4	91047.55	433810.41
CPT000000143203	2	87315.65	433449.01	CPT000000156001	4	91072.82	433802.66
CPT000000143237	2	87299.99	433468.5	CPT000000156007	4	91031.9	433838.2

Table C.3: CPTs used in the Pernis.

C.2. Removing the transition zones of the Pleistocene sand layer

This section contains the tables for the refined boundaries of the Pleistocene sand layer. The refined upper and lower boundaries are found by removing the transition zones. If there is no transition zone at the bottom, the lower boundary will be at most -40 m NAP.

The reason for this choice is because the depth at which the base of foundation piles are placed are usually somewhere around -20 m NAP to -35 m NAP. So practically, one would only investigate up to these depth and deeper cone resistance data would be considered unnecessary for these practical reasons.

Maasvlakte

CPT ID	Site ID	Estimated layer top [m NAP]	Estimated layer bottom [m NAP]	CPT ID	Site ID	Estimated layer top [m NAP]	Estimated layer bottom [m NAP]
CPT000000130993	4	-23.66	-40.63	CPT000000156212	3	-27.187	-38.964
CPT000000132169	4	-22.78	-48.23	CPT000000156214	1	-22.424	-44.507
CPT000000132692	4	-23.33	-48.68	CPT000000156222	1	-22.248	-44.771
CPT000000132746	4	-23.47	-47.1	CPT000000156227	3	-24.076	-30.472
CPT000000132990	4	-23.58	-41.67	CPT000000156228	1	-24.2	-43.613
CPT000000134189	4	-22.23	-50.57	CPT000000156233	1	-24.614	-44.9
CPT000000140082	4	-35.13	-54.51	CPT000000156249	1	-23.239	-42.767
CPT000000140543	4	-27.94	-35.29	CPT000000156256	1	-22.456	-32.183
CPT000000142698	4	-21.22	-40.84	CPT000000156275	1	-22.955	-41.33
CPT000000143152	4	-20.47	-41.4	CPT000000156451	2 (0)	-19.401	-49.441
CPT000000146237	4	-21.47	-35.68	CPT000000156452	2 (1)	-27.776	-41.912
CPT000000147186	4	-23.09	-36.18	CPT000000156458	2 (1)	-22.177	-48.541
CPT000000147306	4	-23.26	-42.42	CPT000000156460	2 (1)	-22.698	-43.411
CPT000000155990	3	-28.784	-33.442	CPT000000156466	2 (1)	-30.357	-41.259
CPT000000156016	3	-25.531	-35.364	CPT000000156472	2 (0)	-23.898	-28.677
CPT000000156041	3	-23.428	-34.521	CPT000000156475	2 (0)	-22.082	-42.774
CPT000000156058	3	-24.458	-39.993	CPT000000156476	2 (1)	-23.031	-43.953
CPT000000156091	3	-25.161	-44.149	CPT000000156482	2 (1)	-21.965	-44.026
CPT000000156106	3	-23.711	-33.011	CPT000000156491	2 (0)	-22.642	-40.554
CPT000000156120	3	-23.838	-35.202	CPT000000156494	2 (0)	-22.207	-49.413
CPT000000156129	3	-25.404	-50.356	CPT000000156498	2 (1)	-29.502	-43.912
CPT000000156130	1	-23.531	-39.883	CPT000000156499	2 (1)	-28.459	-40.741
CPT000000156135	3	-28.103	-33.38	CPT000000156512	2 (0)	-20.986	-49.717
CPT000000156143	3	-23.751	-33.547	CPT000000156512	2 (1)	-20.986	-49.717
CPT000000156144	1	-17.601	-40.544	CPT000000156517	2 (1)	-20.467	-41.421
CPT000000156145	3	-22.558	-35.21	CPT000000156519	2 (1)	-22.581	-48.876
CPT000000156159	1	-19.526	-40.362	CPT000000156525	2 (0)	-22.571	-41.38
CPT000000156167	3	-34.887	-39.706	CPT000000156527	2 (1)	-28.796	-40.741
CPT000000156180	1	-18.119	-41.432	CPT000000156533	2 (0)	-23.554	-48.63
CPT000000156191	1	-17.014	-41.166	CPT000000156533	2 (1)	-23.554	-48.63
CPT000000156196	3	-23.604	-39.256				

Table C.4: Top and bottom of the Pleistocene sand layer in Maasvlakte before removing the transition zones.

CPT ID	Site ID	Definitive layer top [m NAP]	Definitive layer bottom [m NAP]	CPT ID	Site ID	Definitive layer top [m NAP]	Definitive layer bottom [m NAP]
CPT000000130993	4	-24.73	-30.99	CPT000000156212	3	-27.605	-37.279
CPT000000132169	4	-25.69	-34.36	CPT000000156214	1	-22.802	-38.998
CPT000000132692	4	-24.65	-29.37	CPT000000156222	1	-23.326	-39.395
CPT000000132746	4	-24.19	-29.54	CPT000000156227	3	-26.194	-30.212
CPT000000132990	4	-24.69	-30.07	CPT000000156228	1	-24.798	-38.154
CPT000000134189	4	-29.21	-33.67	CPT000000156233	1	-24.874	-38.521
CPT000000140082	4	-25.94	-30.2	CPT000000156249	1	-24.338	-38.377
CPT000000140543	4	-28.28	-34.26	CPT000000156256	1	-22.575	-32.084
CPT000000142698	4	-28.07	-32.34	CPT000000156275	1	-23.891	-39.161
CPT000000143152	4	-23.31	-27.43	CPT000000156451	2 (0)	-23.254	-28.519
CPT000000146237	4	-22.67	-27.15	CPT000000156452	2 (1)	-34.486	-38.074
CPT000000147186	4	-25.19	-34.81	CPT000000156458	2 (1)	-34.287	-37.357
CPT000000147306	4	-29.01	-35.03	CPT000000156460	2 (1)	-34.619	-37.96
CPT000000155990	3	-28.864	-33.362	CPT000000156466	2 (1)	-34.617	-35.466
CPT000000156016	3	-25.651	-35.364	CPT000000156472	2 (0)	-24.037	-26.726
CPT000000156041	3	-23.648	-34.161	CPT000000156475	2 (0)	-22.722	-30.913
CPT000000156058	3	-30.775	-39.333	CPT000000156476	2 (1)	-35.744	-37.196
CPT000000156091	3	-25.581	-36.139	CPT000000156482	2 (1)	-34.484	-37.793
CPT000000156106	3	-26.386	-32.332	CPT000000156491	2 (0)	-25.531	-31.009

CPT000000156120	3	-24.697	-30.431	CPT000000156494	2 (0)	-23.427	-31.776
CPT000000156129	3	-26.658	-39.701	CPT000000156498	2 (1)	-34.533	-35.415
CPT000000156130	1	-24.286	-33.797	CPT000000156499	2 (1)	-33.026	-35.874
CPT000000156135	3	-28.223	-31.961	CPT000000156512	2 (0)	-26.724	-30.322
CPT000000156143	3	-26.11	-32.148	CPT000000156512	2 (1)	-35.056	-36.772
CPT000000156144	1	-23.044	-40.484	CPT000000156517	2 (1)	-34.012	-35.974
CPT000000156145	3	-23.814	-34.932	CPT000000156519	2 (1)	-34.152	-35.86
CPT000000156159	1	-23.065	-38.004	CPT000000156525	2 (0)	-23.37	-27.997
CPT000000156167	3	-35.207	-39.546	CPT000000156527	2 (1)	-34.662	-38.07
CPT000000156180	1	-23.77	-39.627	CPT000000156533	2 (0)	-27.45	-30.204
CPT000000156191	1	-23.27	-39.952	CPT000000156533	2 (1)	-34.773	-36.228
CPT000000156196	3	-24.963	-38.121				

Table C.5: Top and bottom of the Pleistocene sand layer in Maasvlakte after removing the transition zones.

Botlek

CPT ID	Site ID	Estimated layer top [m NAP]	Estimated layer bottom [m NAP]	CPT ID	Site ID	Estimated layer top [m NAP]	Estimated layer bottom [m NAP]
CPT000000087531	1	-20.526	-29.079	CPT000000140531	3	-18.89	-40.77
CPT000000087532	1	-23.943	-28.987	CPT000000140632	3	-20.78	-40.26
CPT000000091781	2	-22.512	-35.786	CPT000000140863	4	-19.93	-39.62
CPT000000091782	2	-18.488	-35.339	CPT000000141556	4	-19.3	-39.1
CPT000000091784	2	-18.658	-35.794	CPT000000141676	4	-19.08	-41.1
CPT000000091785	2	-18.442	-31.72	CPT000000141902	3	-18.61	-40.56
CPT000000091786	2	-18.205	-31.806	CPT000000142443	4	-24.95	-40.86
CPT000000091790	2	-18.944	-35.903	CPT000000142481	4	-21.49	-40.89
CPT000000091791	2	-18.538	-35.904	CPT000000143085	3	-19.3	-39.16
CPT000000091795	2	-18.31	-29.92	CPT000000143723	4	-22.37	-41.11
CPT000000091799	2	-18.668	-35.894	CPT000000145368	3	-24.19	-39.99
CPT000000091800	2	-18.521	-24.891	CPT000000145450	4	-24.3	-38.24
CPT000000091801	2	-21.434	-35.872	CPT000000145558	3	-22.41	-40.46
CPT000000091804	2	-19.099	-35.412	CPT000000145626	4	-20.1	-40.02
CPT000000091806	2	-19.36	-35.282	CPT000000145634	4	-19.18	-39.98
CPT000000091807	2	-18.36	-31.886	CPT000000145998	4	-19	-32.66
CPT000000091808	2	-18.755	-35.287	CPT000000146636	4	-20.17	-41.15
CPT000000091809	2	-18.664	-35.792	CPT000000146786	4	-19.02	-34.46
CPT000000091810	2	-18.704	-35.637	CPT000000146869	4	-20.52	-41.22
CPT000000091811	2	-18.55	-35.696	CPT000000146928	3	-18.6	-40.1
CPT000000091814	2	-18.566	-35.648	CPT000000147207	3	-20.09	-40.54
CPT000000097366	1	-19.329	-29.646	CPT000000147221	3	-18.93	-40.66
CPT000000130642	4	-19.69	-40.13	CPT000000147556	3	-18.37	-40.69
CPT000000130968	3	-18.23	-40.56	CPT000000147882	3	-20.69	-40.86
CPT000000130982	3	-18.75	-40.39	CPT000000156354	1	-19.022	-29.353
CPT000000131904	3	-24.68	-39.97	CPT000000156355	1	-21.366	-33.62
CPT000000132170	3	-18.58	-40.36	CPT000000156358	1	-23.296	-29.873
CPT000000132368	4	-19.18	-33.9	CPT000000156364	1	-20.645	-34.479
CPT000000132891	3	-18.51	-40.48	CPT000000156370	1	-20.151	-34.158
CPT000000133208	4	-18.85	-32.65	CPT000000156372	1	-23.547	-29.562
CPT000000133214	4	-18.32	-39.91	CPT000000156376	1	-18.657	-29.46
CPT000000133221	4	-19.08	-36.85	CPT000000156384	1	-18.924	-29.432
CPT000000133522	4	-18.84	-37.48	CPT000000156388	1	-20.969	-29.147
CPT000000133821	4	-18.91	-41.11	CPT000000156395	1	-24.726	-29.392
CPT000000133845	4	-26.09	-39.86	CPT000000156401	1	-22.069	-29.337

Table C.6: Top and bottom of the Pleistocene sand layer in Botlek before removing the transition zones.

CPT ID	Site ID	Definitive layer top [m NAP]	Definitive layer bottom [m NAP]	CPT ID	Site ID	Definitive layer top [m NAP]	Definitive layer bottom [m NAP]
CPT000000087531	1	-21.545	-27.361	CPT000000140531	3	-25.95	-39.1
CPT000000087532	1	-25.718	-28.708	CPT000000140632	3	-32.4	-39.4

CPT000000091781	2	-24.567	-35.249	CPT000000140863	4	-29.12	-35.38
CPT000000091782	2	-22.827	-32.101	CPT000000141556	4	-29.11	-38.01
CPT000000091784	2	-27.003	-34.903	CPT000000141676	4	-26.66	-34.46
CPT000000091785	2	-21.273	-26.438	CPT000000141902	3	-22.65	-38.92
CPT000000091786	2	-21.998	-27.324	CPT000000142443	4	-30.83	-38.18
CPT000000091790	2	-25.935	-33.234	CPT000000142481	4	-28.61	-37.14
CPT000000091791	2	-31.831	-35.645	CPT000000143085	3	-30.2	-38.24
CPT000000091795	2	-24.498	-29.364	CPT000000143723	4	-27.6	-35.04
CPT000000091799	2	-28.064	-32.54	CPT000000145368	3	-28.06	-36.19
CPT000000091800	2	-21.29	-24.076	CPT000000145450	4	-26.85	-37.94
CPT000000091801	2	-25.424	-30.844	CPT000000145558	3	-27.86	-38.82
CPT000000091804	2	-23.384	-29.413	CPT000000145626	4	-24.13	-35.48
CPT000000091806	2	-29.056	-33.532	CPT000000145634	4	-23.47	-37.17
CPT000000091807	2	-23.952	-28.041	CPT000000145998	4	-22.44	-26.51
CPT000000091808	2	-22.73	-29.891	CPT000000146636	4	-23.67	-33.24
CPT000000091809	2	-23.923	-29.315	CPT000000146786	4	-24.31	-28.41
CPT000000091810	2	-27.646	-33.67	CPT000000146869	4	-26.92	-38.27
CPT000000091811	2	-27.661	-31.633	CPT000000146928	3	-28.12	-38.54
CPT000000091814	2	-21.73	-28.175	CPT000000147207	3	-31.37	-38.07
CPT000000097366	1	-22.588	-28.667	CPT000000147221	3	-24.52	-38.6
CPT000000130642	4	-22.34	-38.75	CPT000000147556	3	-24.21	-38.61
CPT000000130968	3	-21.47	-39.63	CPT000000147882	3	-33.96	-38.81
CPT000000130982	3	-21.32	-37.84	CPT000000156354	1	-20.376	-28.463
CPT000000131904	3	-31.4	-38.16	CPT000000156355	1	-23.978	-30.389
CPT000000132170	3	-22.51	-37.75	CPT000000156358	1	-25.391	-29.324
CPT000000132368	4	-26.47	-32.9	CPT000000156364	1	-23.614	-28.917
CPT000000132891	3	-23.32	-38.74	CPT000000156370	1	-22.7	-29.772
CPT000000133208	4	-25.25	-31.4	CPT000000156372	1	-26.085	-29.362
CPT000000133214	4	-24.17	-35.29	CPT000000156376	1	-23.581	-26.711
CPT000000133221	4	-23.27	-34.67	CPT000000156384	1	-20.711	-26.081
CPT000000133522	4	-23.09	-36.78	CPT000000156388	1	-23.248	-26.708
CPT000000133821	4	-27.5	-38.08	CPT000000156395	1	-25.855	-28.403
CPT000000133845	4	-30.34	-37.12	CPT000000156401	1	-23.447	-28.309

Table C.7: Top and bottom of the Pleistocene sand layer in Botlek after removing the transition zones.

Pernis

CPT ID	Site ID	Estimated layer top [m NAP]	Estimated layer bottom [m NAP]	CPT ID	Site ID	Estimated layer top [m NAP]	Estimated layer bottom [m NAP]
CPT000000130932	3	-19.16	-25.45	CPT000000144494	1	-18.19	-26.79
CPT000000130956	3	-15.26	-26	CPT000000144681	1	-21.04	-26.14
CPT000000133438	3	-15.06	-26.43	CPT000000145890	1	-17.04	-24.49
CPT000000140125	3	-14.94	-24.78	CPT000000145969	1	-21.24	-26.13
CPT000000140814	1	-18.86	-25.95	CPT000000150567	1	-21.67	-27.22
CPT000000141380	2	-17.6	-28.29	CPT000000150577	1	-19.17	-26.72
CPT000000141532	2	-17.69	-28.66	CPT000000155906	4	-17.31	-29.4
CPT000000141803	2	-23.31	-27.97	CPT000000155919	4	-17.23	-29.09
CPT000000142179	1	-15.12	-25.98	CPT000000155925	4	-17.09	-29.22
CPT000000142322	2	-18.28	-27.22	CPT000000155932	4	-19.87	-29.24
CPT000000143102	2	-17.61	-27.05	CPT000000155992	4	-17.05	-26.19
CPT000000143203	2	-17.44	-27.96	CPT000000156001	4	-16.92	-26.14
CPT000000143237	2	-17.48	-28.25	CPT000000156007	4	-17.17	-25.49

Table C.8: Top and bottom of the Pleistocene sand layer in Pernis before removing the transition zones.

CPT ID	Site ID	Definitive layer top [m NAP]	Definitive layer bottom [m NAP]	CPT ID	Site ID	Definitive layer top [m NAP]	Definitive layer bottom [m NAP]
CPT000000130932	3	-21.56	-24.27	CPT000000144494	1	-21.14	-24.94
CPT000000130956	3	-23.6	-25.40	CPT000000144681	1	-21.76	-24.26
CPT000000133438	3	-22.87	-24.95	CPT000000145890	1	-17.29	-20.49
CPT000000140125	3	-21.88	-23.18	CPT000000145969	1	-21.95	-25.33

CPT000000140814	1	-21.3	-25.63	CPT000000150567	1	-22.59	-26.17
CPT000000141380	2	-22.81	-26.68	CPT000000150577	1	-20.04	-24.16
CPT000000141532	2	-21.42	-26.60	CPT000000155906	4	-18.49	-26.49
CPT000000141803	2	-23.57	-26.33	CPT000000155919	4	-19.22	-26.20
CPT000000142179	1	-21.8	-24.31	CPT000000155925	4	-19.08	-25.39
CPT000000142322	2	-22.55	-25.27	CPT000000155932	4	-21.47	-25.86
CPT000000143102	2	-21.08	-25.42	CPT000000155992	4	-20.82	-25.13
CPT000000143203	2	-20.72	-23.00	CPT000000156001	4	-20.33	-24.07
CPT000000143237	2	-18.98	-23.12	CPT000000156007	4	-20.66	-22.84

Table C.9: Top and bottom of the Pleistocene sand layer in Pernis after removing the transition zones.

C.3. Borehole verification

This section compares the measured boundary of the Pleistocene sand to the estimated boundaries. The measured layer boundary comes from borehole data and the estimated layer boundaries comes from five CPTs which are closest to the borehole. With the comparison one can roughly validate whether the soil profile and the chosen sand layer from the SBT_n approach correspond to the measured soil profile and the correct geological formation.

For each site, a borehole will be used for the comparison. The comparison is split into two sections. The first section is a comparison of the upper layer boundary and the result is summarized into the tables below. For the second section, only five CPTs will be used and it is a visual comparison of the measured and estimated soil profiles. The “measured” geological formations will also displayed and with the estimated upper layer boundary in mind, one can validate whether the chosen sand layer belongs to the Kreftenheye and Boxtel Formation, Delwijnen Member.

C.3.1. Comparison of the upper layer boundary of the Pleistocene sand

The comparison between upper Pleistocene layer boundaries are summarized in the tables below and the estimated upper layer boundary from before the transition zone removal is used.

Maasvlakte

Borehole ID	Measured upper Pleistocene sand layer boundary [m NAP]		
B37A0178	-23.73		
CPT ID	Estimated upper Pleistocene sand layer boundary [m NAP]	Difference between measured and estimated [m]	Distance from borehole [m]
CPT000000156130	-23.531	+0.199	664.88
CPT000000156180	-18.119	+5.611	668.92
CPT000000156191	-17.014	+6.716	665.56
CPT000000156249	-23.239	+0.491	665.26
CPT000000156275	-22.955	+0.775	667.06

Table C.10: Comparison of the measured and five estimated upper Pleistocene sand layer boundaries at site M1.

Borehole ID	Measured upper Pleistocene sand layer boundary [m NAP]		
B37A0089	-22.95		
CPT ID	Estimated upper Pleistocene sand layer boundary [m NAP]	Difference between measured and estimated [m]	Distance from borehole [m]
CPT000000156472	-23.898	-0.948	278.34
CPT000000156491	-22.642	+0.308	268.32
CPT000000156525	-22.571	+0.379	252.96
CPT000000156533	-23.554	-0.604	273.08
CPT000000156460	-22.698	+0.252	289.08

Table C.11: Comparison of the measured and five estimated upper Pleistocene sand layer boundaries at site M2.

Borehole ID	Measured upper Pleistocene sand layer boundary [m NAP]		
B37A0259	-23.04		
CPT ID	Estimated upper Pleistocene sand layer boundary [m NAP]	Difference between measured and estimated [m]	Distance from borehole [m]
CPT000000156041	-23.428	-0.388	2539.70
CPT000000156120	-23.838	-0.798	2065.81
CPT000000156129	-25.404	-2.364	2416.85
CPT000000156143	-23.751	-0.711	1921.01
CPT000000156145	-22.558	+0.482	2432.57

Table C.12: Comparison of the measured and five estimated upper Pleistocene sand layer boundaries at site M3.

Borehole ID	Measured upper Pleistocene sand layer boundary [m NAP]		
B37A0177	-23.20		
CPT ID	Estimated upper Pleistocene sand layer boundary [m NAP]	Difference between measured and estimated [m]	Distance from borehole [m]
CPT000000130993	-23.66	-0.46	178.31
CPT000000132169	-22.78	+0.42	43.07
CPT000000132692	-23.33	-0.13	28.33
CPT000000132990	-23.58	-0.38	128.13
CPT000000142698	-21.22	+1.98	224.89

Table C.13: Comparison of the measured and five estimated upper Pleistocene sand layer boundaries at site M4.

Botlek

Borehole ID	Measured upper Pleistocene sand layer boundary [m NAP]		
B37G0164	-18.45		
CPT ID	Estimated upper Pleistocene sand layer boundary [m NAP]	Difference between measured and estimated [m]	Distance from borehole [m]
CPT000000087531	-20.526	-2.076	65.89
CPT000000087532	-23.943	-5.493	86.70
CPT000000097366	-19.329	-0.879	101.84
CPT000000156354	-19.022	-0.572	92.35
CPT000000156388	-20.969	-2.519	74.72

Table C.14: Comparison of the measured and five estimated upper Pleistocene sand layer boundaries at site B1.

Borehole ID	Measured upper Pleistocene sand layer boundary [m NAP]		
B37G0355	-20.10		
CPT ID	Estimated upper Pleistocene sand layer boundary [m NAP]	Difference between measured and estimated [m]	Distance from borehole [m]
CPT000000091785	-18.442	+1.658	500.31
CPT000000091809	-18.664	+1.436	438.98
CPT000000091810	-18.704	+1.396	493.28
CPT000000091811	-18.55	+1.550	478.29
CPT000000091814	-18.566	+1.534	458.39

Table C.15: Comparison of the measured and five estimated upper Pleistocene sand layer boundaries at site B2.

Borehole ID	Measured upper Pleistocene sand layer boundary [m NAP]		
B37G0502	-19.12		
CPT ID	Estimated upper Pleistocene sand layer boundary [m NAP]	Difference between measured and estimated [m]	Distance from borehole [m]
CPT000000130968	-18.23	+0.89	305.41
CPT000000130982	-18.75	+0.37	366.71
CPT000000131904	-24.68	-5.56	274.52
CPT000000132891	-18.51	+0.61	320.03
CPT000000145558	-22.41	-3.29	297.09

Table C.16: Comparison of the measured and five estimated upper Pleistocene sand layer boundaries at site B3.

Borehole ID	Measured upper Pleistocene sand layer boundary [m NAP]		
B37D0079	-18.90		
CPT ID	Estimated upper Pleistocene sand layer boundary [m NAP]	Difference between measured and estimated [m]	Distance from borehole [m]
CPT000000130642	-19.69	-0.79	244.87
CPT000000133221	-19.08	-0.18	236.68
CPT000000140863	-19.93	-1.03	263.53
CPT000000145450	-24.3	-5.40	236.13
CPT000000146786	-19.02	-0.12	228.42

Table C.17: Comparison of the measured and five estimated upper Pleistocene sand layer boundaries at site B4.

Pernis

Borehole ID	Measured upper Pleistocene sand layer boundary [m NAP]		
B37G0478	-17.92		
CPT ID	Estimated upper Pleistocene sand layer boundary [m NAP]	Difference between measured and estimated [m]	Distance from borehole [m]
CPT000000140814	-18.86	-0.94	121.95
CPT000000142179	-15.12	+2.80	125.97
CPT000000144681	-21.04	-3.12	142.08
CPT000000145969	-21.24	-3.32	146.75
CPT000000150567	-21.67	-3.75	242.57

Table C.18: Comparison of the measured and five estimated upper Pleistocene sand layer boundaries at site P1.

Borehole ID	Measured upper Pleistocene sand layer boundary [m NAP]		
B37G0482	-18.07		
CPT ID	Estimated upper Pleistocene sand layer boundary [m NAP]	Difference between measured and estimated [m]	Distance from borehole [m]
CPT000000141803	-23.31	-5.24	148.34
CPT000000142322	-18.28	-0.21	247.24
CPT000000143102	-17.61	+0.46	221.66
CPT000000143203	-17.44	+0.63	270.82
CPT000000143237	-17.48	+0.59	295.42

Table C.19: Comparison of the measured and five estimated upper Pleistocene sand layer boundaries at site P2.

Borehole ID	Measured upper Pleistocene sand layer boundary [m NAP]		
B37G0472	-17.16		
CPT ID	Estimated upper Pleistocene sand layer boundary [m NAP]	Difference between measured and estimated [m]	Distance from borehole [m]
CPT000000130932	-19.16	-2.00	1947.04
CPT000000130956	-15.26	+1.90	1796.75
CPT000000133438	-15.06	+2.10	1846.83
CPT000000140125	-14.94	+2.22	1896.92

Table C.20: Comparison of the measured and five estimated upper Pleistocene sand layer boundaries at site P3.

Borehole ID	Measured upper Pleistocene sand layer boundary [m NAP]		
B37H0497	-17.02		
CPT ID	Estimated upper Pleistocene sand layer boundary [m NAP]	Difference between measured and estimated [m]	Distance from borehole [m]
CPT000000155919	-17.23	-0.21	543.17
CPT000000155925	-17.09	-0.07	567.48
CPT000000155992	-17.05	-0.03	469.51
CPT000000156001	-16.92	+0.10	443.09
CPT000000156007	-17.17	-0.15	492.53

Table C.21: Comparison of the measured and five estimated upper Pleistocene sand layer boundaries at site P4.

C.3.2. Comparison between measured and estimated soil profiles

Maasvlakte

Site M1

Identification :	B37A0178
Coordinates :	60565 , 443230 (RD)
Surface level:	-9.90 m rel. to NAP
Available information:	Scanned documents and digital recordings
Description standard:	Unknown
Quality of geological interpretation:	Automated interpretation from modelling workflo\

Lithostratigraphy
- AAOP
- NAWO
- EC
- NIBA
- KR

Lithology
- Clay
- Sand, fine category
- Sand, medium category
- Shells
- Peat
- No sample

Borehole log profile

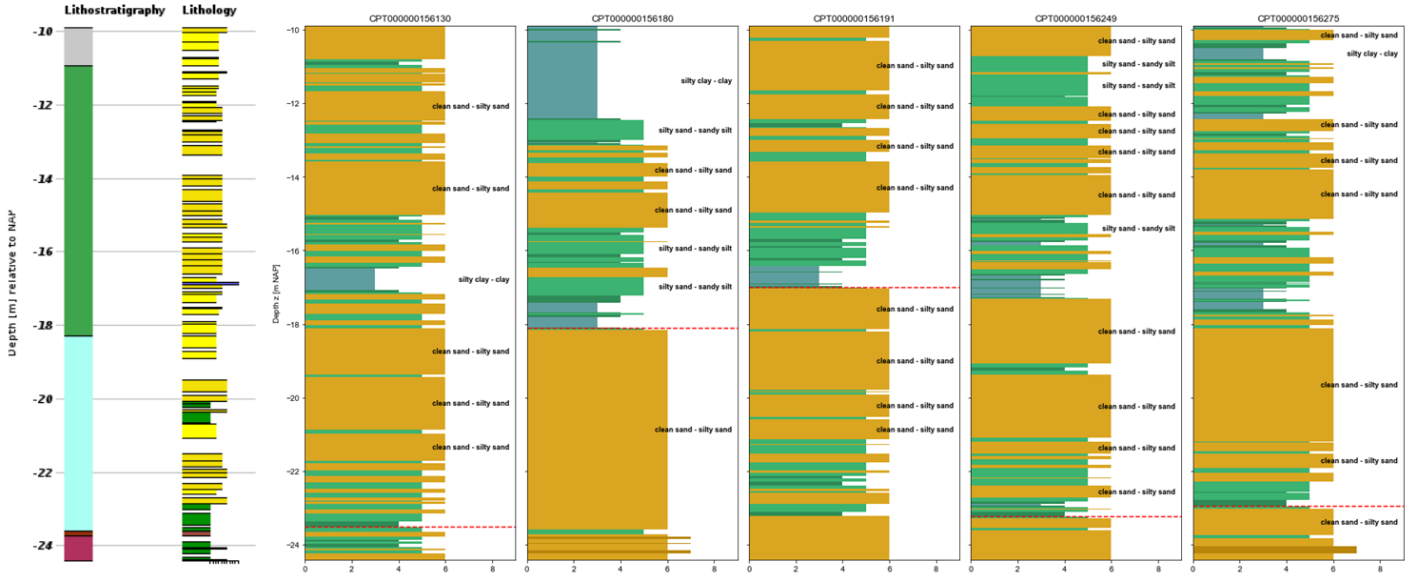

Figure C.1: Visual comparison between borehole and CPTs from site M1.

Site M2

Identification :	B37A0089
Coordinates :	64360 , 439360 (RD)
Surface level:	-0.70 m rel. to NAP
Available information:	Scanned documents and digital recordings
Description standard:	Unknown
Quality of geological interpretation:	Automated interpretation from modelling workflo\

Lithostratigraphy
- AAOP
- NIBA
- KR

Lithology
- Clay
- Sand, fine category
- Sand, medium category
- Sand, coarse category
- Shells
- Peat
- No sample

Borehole log profile

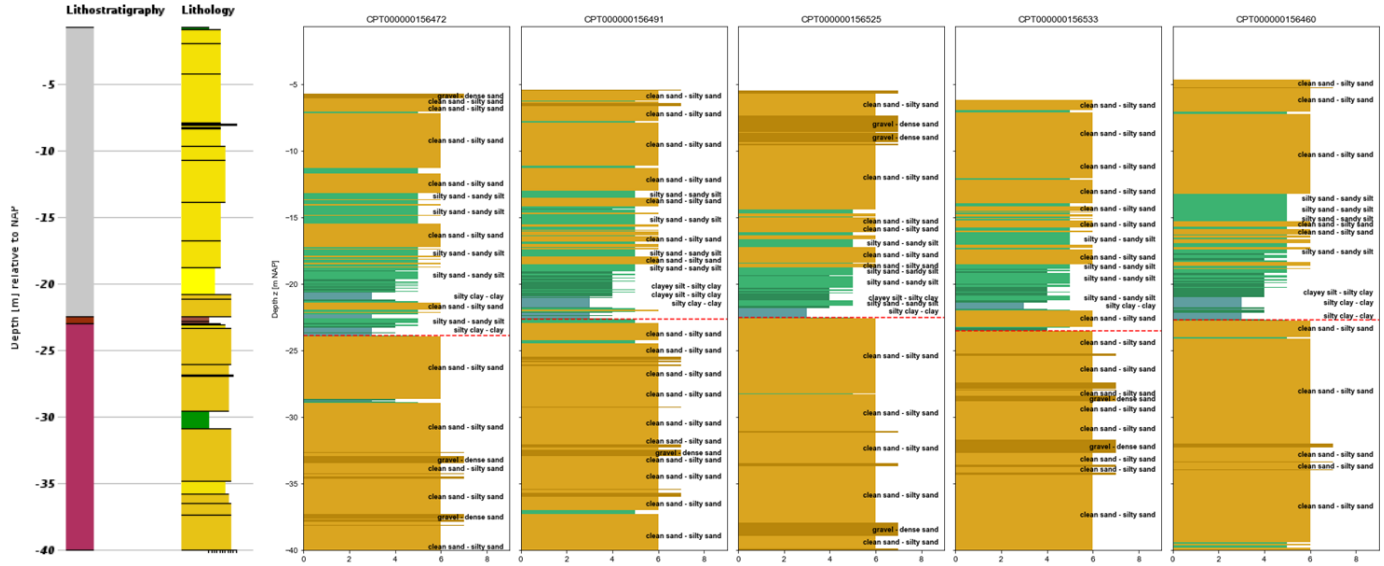

Figure C.2: Visual comparison between borehole and CPTs from site M2.

Site M3

Identification :	B37A0259
Coordinates :	61305 , 441630 (RD)
Surface level:	4.96 m rel. to NAP
Available information:	Digital recordings
Description standard:	Unknown
Quality of geological interpretation:	Automated interpretation from modelling workflo

Lithostratigraphy
- AAOP
- NAWO
- KR

Lithology
- Clay
- Sand, fine category

Borehole log profile

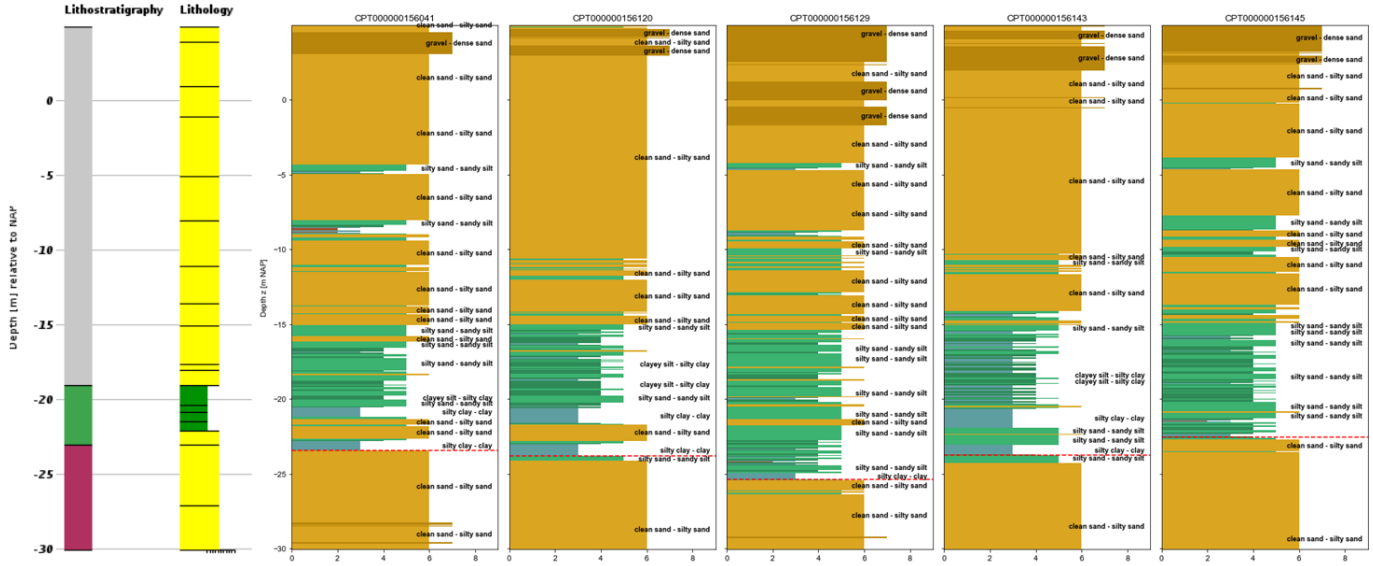

Figure C.3: Visual comparison between borehole and CPTs from site M3.

Site M4

Identification :	B37A0177
Coordinates :	61410 , 444090 (RD)
Surface level:	-9.60 m rel. to NAP
Available information:	Digital recordings
Description standard:	Unknown
Quality of geological interpretation:	Automated interpretation from modelling workflo

Lithostratigraphy
- AAOP
- NAWO
- KR

Lithology
- Clay
- Sand, fine category

Borehole log profile

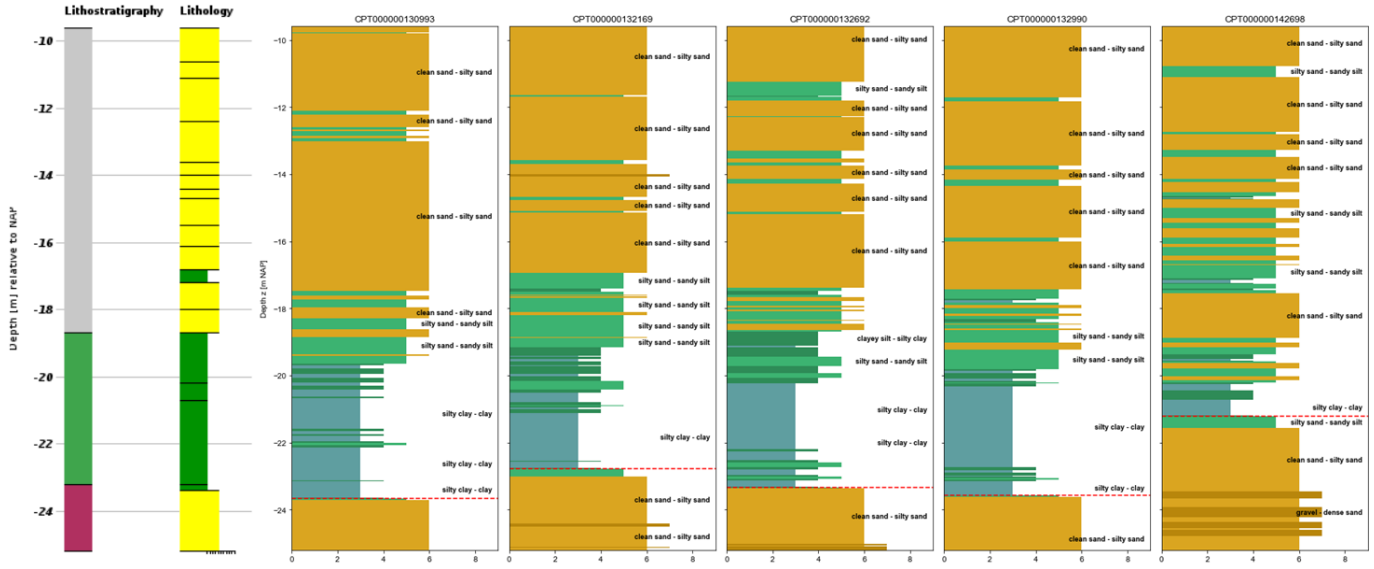

Figure C.4: Visual comparison between borehole and CPTs from site M4.

Botlek

Site B1

Identification :	B37G0164
Coordinates :	81060 , 433795 (RD)
Surface level:	-3.40 m rel. to NAP
Available information:	Digital recordings
Description standard:	Unknown
Quality of geological interpretation:	Automated interpretation from modelling workflo\

Lithostratigraphy
- NAWA
- NAWO
- KR

Lithology
- Clay
- Sand, fine category
- Sand, medium category

Borehole log profile

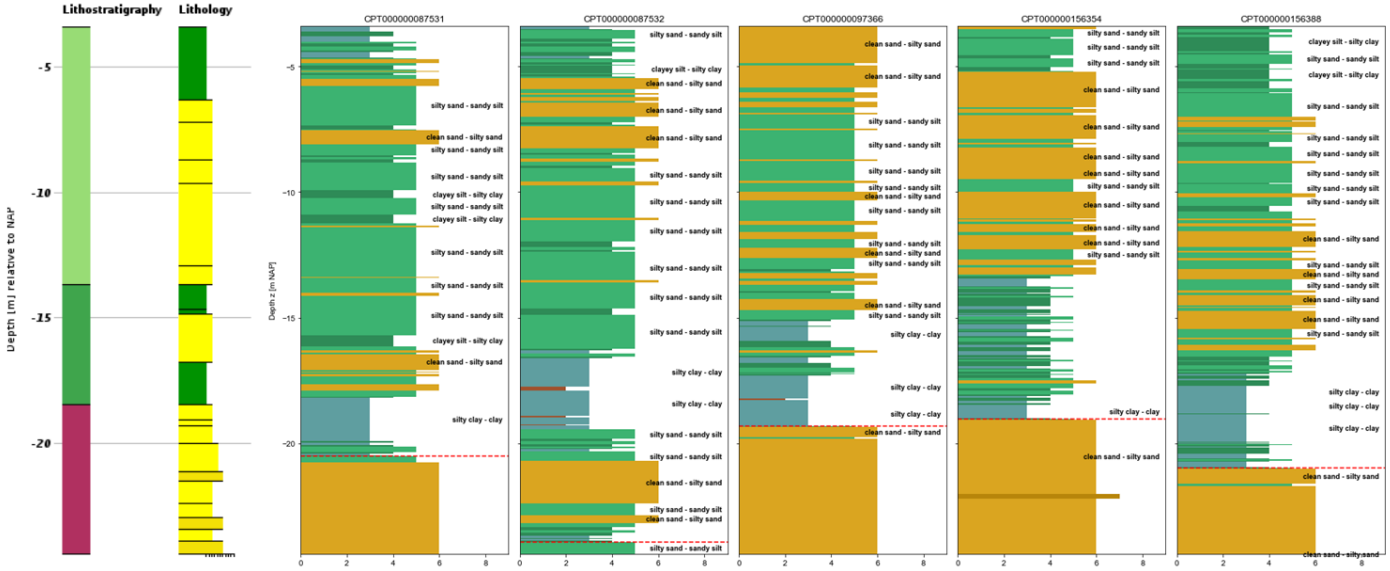

Figure C.5: Visual comparison between borehole and CPTs from site B1.

Site B2

Identification :	B37G0355
Coordinates :	81468 , 432891 (RD)
Surface level:	4.40 m rel. to NAP
Available information:	Digital recordings
Description standard:	Unknown
Quality of geological interpretation:	Automated interpretation from modelling workflo\

Lithostratigraphy
- AAOP
- NAWA
- NI
- EC
- KR

Lithology
- Clay
- Sand, fine category
- Peat

Borehole log profile

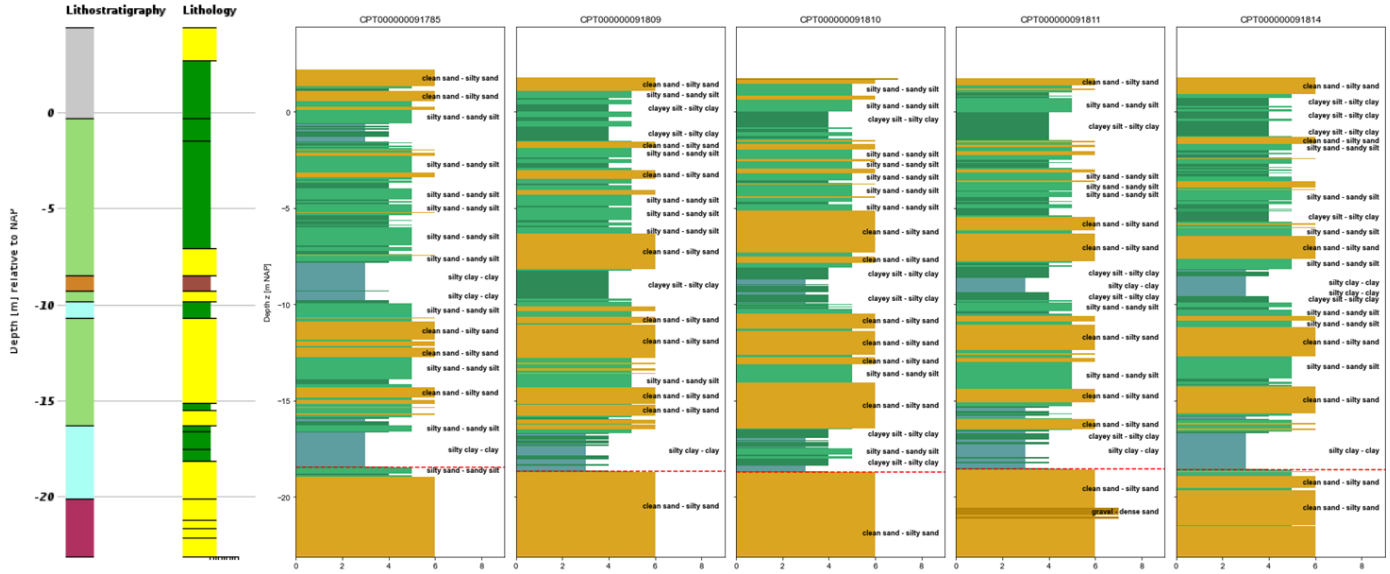

Figure C.6: Visual comparison between borehole and CPTs from site B2.

Site B3

Identification :	B37G0502
Coordinates :	81240 , 432030 (RD)
Surface level:	4.98 m rel. to NAP
Available information:	Digital recordings
Description standard:	Unknown
Quality of geological interpretation:	Automated interpretation from modelling workflo\

Lithostratigraphy

- AAOP
- NAWA
- NAWO
- KR
- WA

Lithology

- Clay
- Sand, fine category
- Sand, medium category
- Sand, coarse category

Borehole log profile

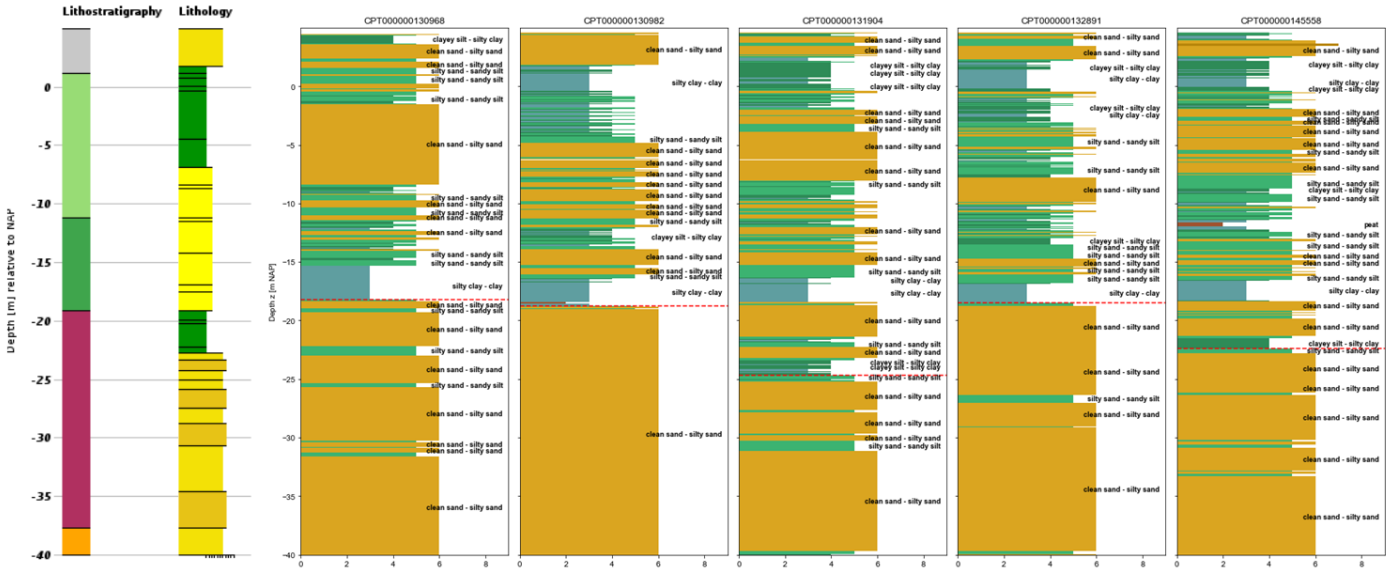

Figure C.7: Visual comparison between borehole and CPTs from site B3.

Site B4

Identification :	B37D0079
Coordinates :	79290 , 434470 (RD)
Surface level:	0.50 m rel. to NAP
Available information:	Digital recordings
Description standard:	Unknown
Quality of geological interpretation:	Automated interpretation from modelling workflo\

Lithostratigraphy
- NAWA
- NAWO
- NIBA
- KR

Lithology
- Loam
- Clay
- Sand, medium category
- Sand, coarse category
- Peat
- No sample

Borehole log profile

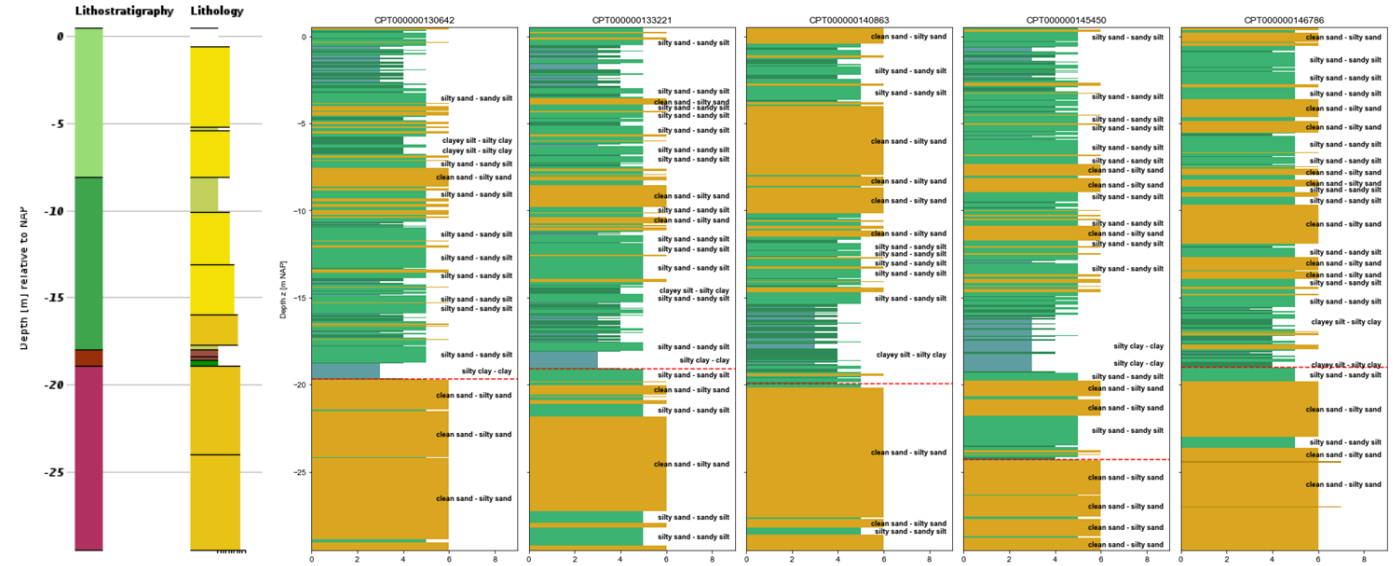

Figure C.8: Visual comparison between borehole and CPTs from site B4.

Pernis

Site P1

Identification :	B37G0478
Coordinates :	87270 , 432700 (RD)
Surface level:	6.08 m rel. to NAP
Available information:	Digital recordings
Description standard:	Unknown
Quality of geological interpretation:	Automated interpretation from modelling workflo\

Lithostratigraphy

- AAOP
- NAWA
- NIHO
- NAWO
- EC
- KR

Lithology

- Loam
- Clay
- Sand, fine category
- Sand, medium category
- Sand, coarse category
- Peat
- Not determined

Borehole log profile

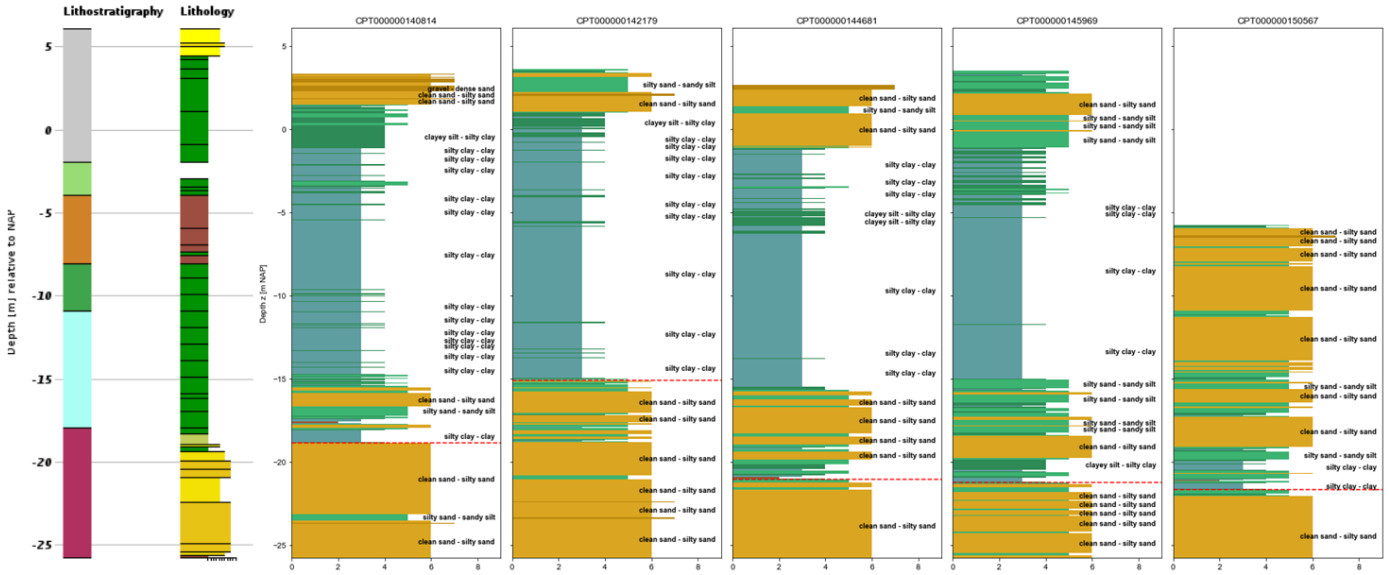

Figure C.9: Visual comparison between borehole and CPTs from site P1.

Site P2

Identification :	B37G0482
Coordinates :	87443 , 433210 (RD)
Surface level:	3.15 m rel. to NAP
Available information:	Digital recordings
Description standard:	Unknown
Quality of geological interpretation:	Automated interpretation from modelling workflo\

Lithostratigraphy
- AAOP
- NAWA
- NI
- NIHO
- NAWO
- EC
- NIBA
- KR

Lithology
- Clay
- Sand, fine category
- Sand, medium category
- Sand, coarse category
- Peat
- No sample

Borehole log profile

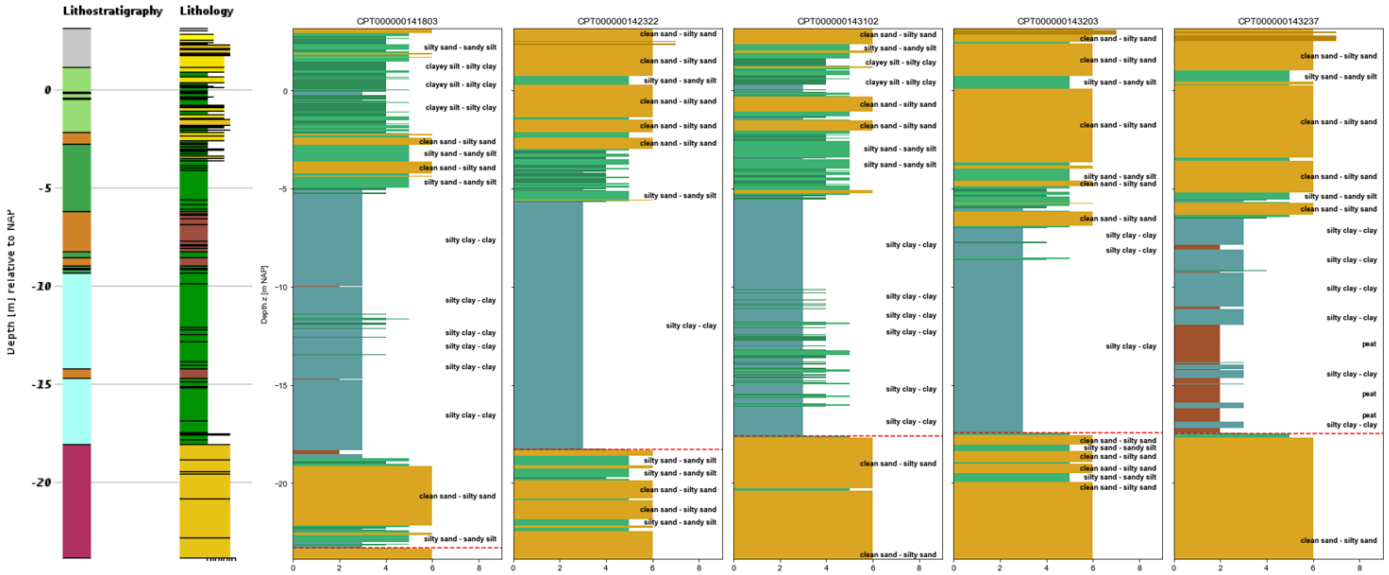

Figure C.10: Visual comparison between borehole and CPTs from site P2.

Site P3

Identification :	B37G0472
Coordinates :	89455 , 434250 (RD)
Surface level:	-5.00 m rel. to NAP
Available information:	Digital recordings
Description standard:	Unknown
Quality of geological interpretation:	Automated interpretation from modelling workflo

Lithostratigraphy
- NAW0
- NI
- EC
- NIBA
- KRWY
- KR

Lithology
- Clay
- Sand, fine category
- Peat

Borehole log profile

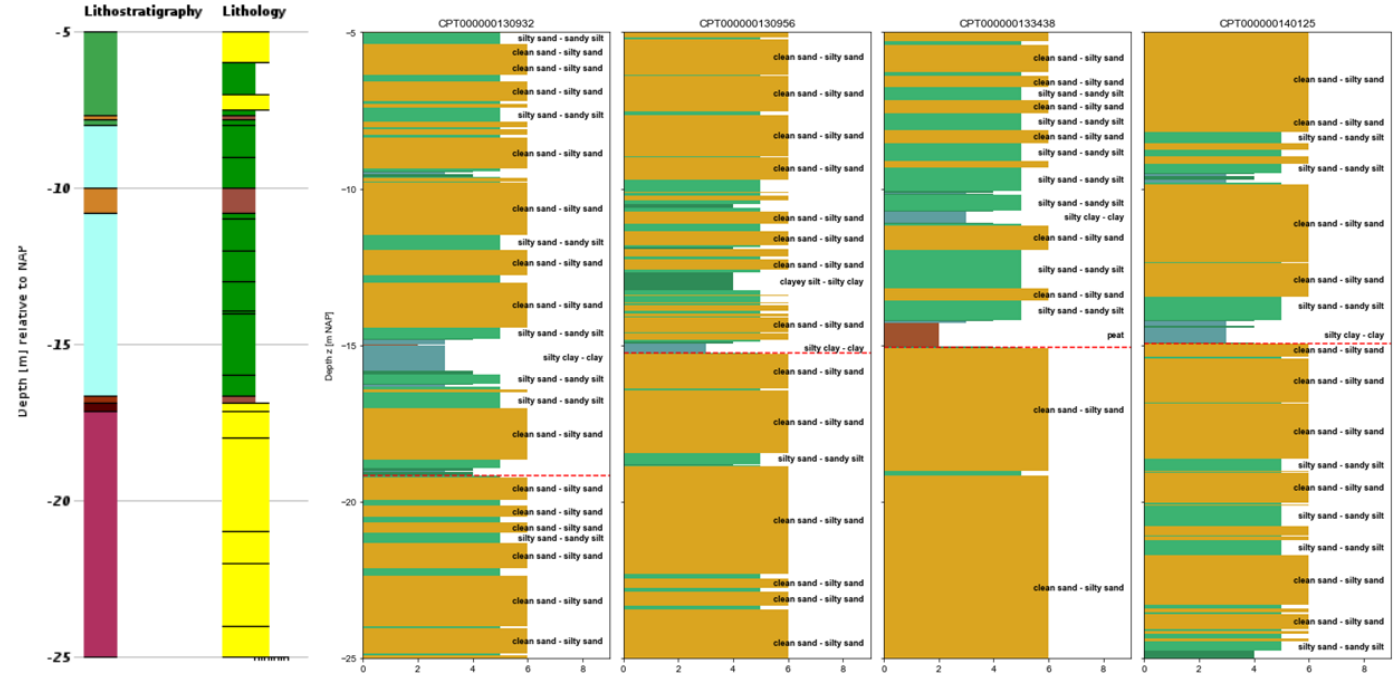

Figure C.11: Visual comparison between borehole and CPTs from site P3.

Site P4

Identification :	B37H0497
Coordinates :	91500 , 433685 (RD)
Surface level:	-1.02 m rel. to NAP
Available information:	Digital recordings
Description standard:	Unknown
Quality of geological interpretation:	Automated interpretation from modelling workflo\

Lithostratigraphy
- NAWA
- NIHO
- NAWO
- KR
- WA

Lithology
- Clay
- Sand, fine category
- Sand, coarse category
- Peat

Borehole log profile

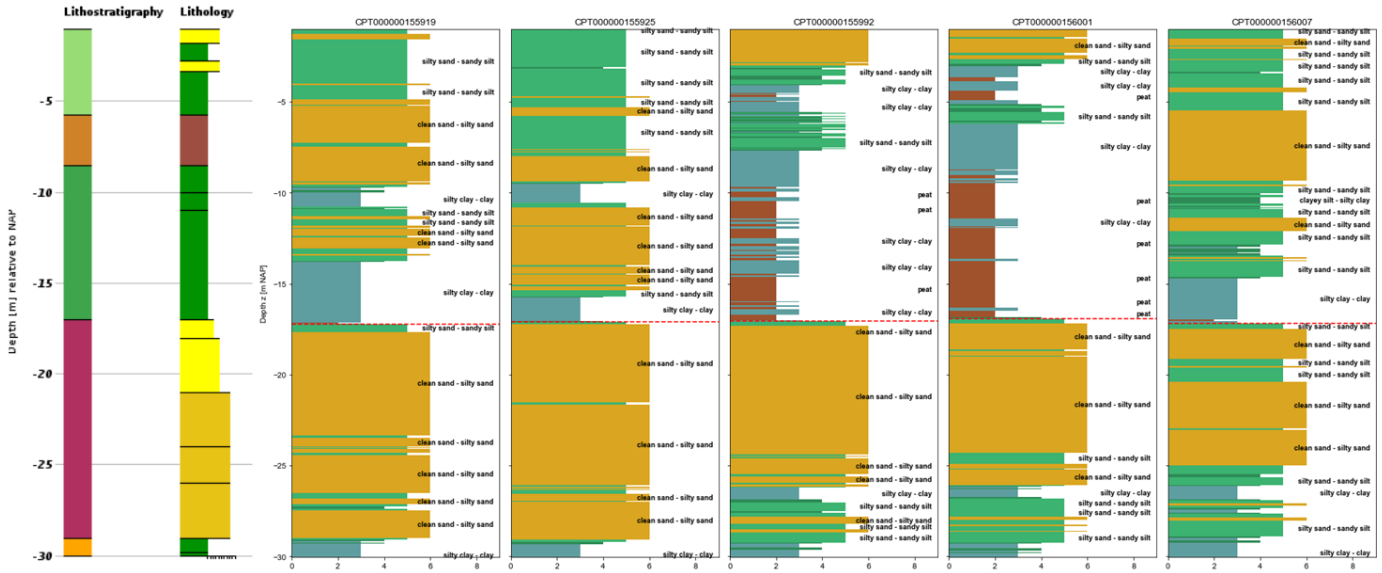

Figure C.12: Visual comparison between borehole and CPTs from site P4.

D. Results of the analysis stage

This appendix contains the results of the analysis stage. Thus it will only contain information about trend lines, vertical scales of fluctuation, random fields that were generated from random field theory and the computed pile base capacities from those random fields.

D.1. Detrending results

This section contains the tables and figures of the trend data for the sites. The mean μ is the mean of the q_c profile and the standard deviation σ is the standard deviation of the residuals.

Maasvlakte

Group ID	$T(z)$ [MPa]	Distribution	μ [MPa]	σ [MPa]	c_v [-]
M.1	$q_c = 39.32$	N	39.32	8.77	0.22
M.2	$q_c - 1.45 * z - 12.65$ (top sublayer)	N	26.69	6.35	0.24
	$q_c - 3.28 * z - 77.20$ (bottom sublayer)	N	40.08	7.99	0.20
M.3	$q_c = -1.20 * z + 9.52$	N	46.79	11.19	0.24
M.4	$q_c = -0.64 * z + 24.02$	N	42.49	9.12	0.21

Table D.1: Results of the trend removal in the Maasvlakte sites.

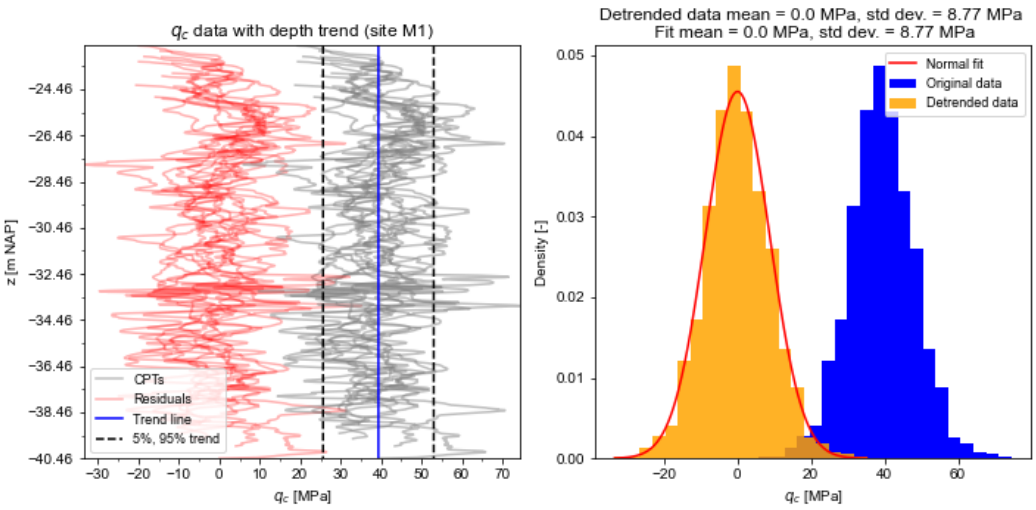

Figure D.1: Trend removal for group M1

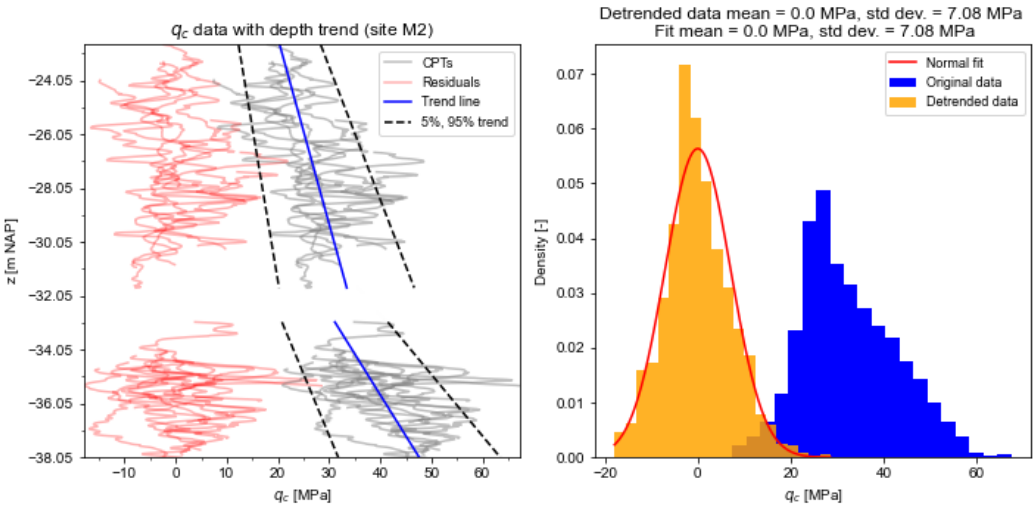

Figure D.2: Trend removal for group M2

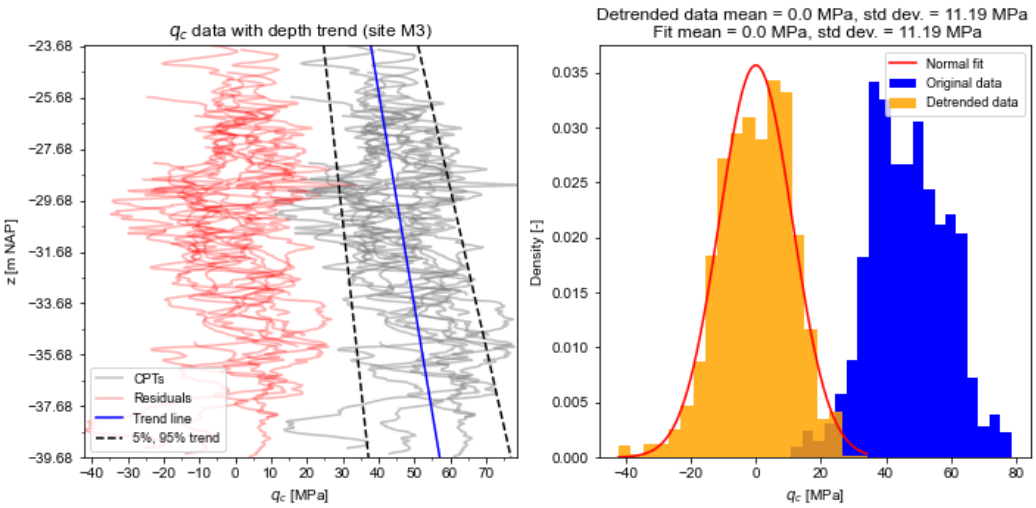

Figure D.3: Trend removal for group M3

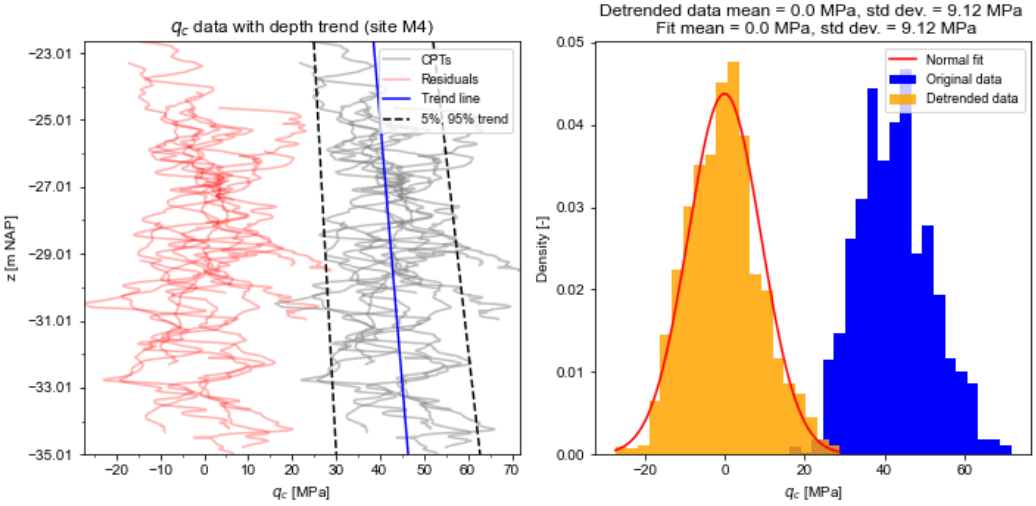

Figure D.4: Trend removal for group M4

Botlek

Group ID	$T(z)$ [MPa]	Distribution	μ [MPa]	σ [MPa]	c_v [-]
B.1	$q_c = -1.20 * z - 7.07$	N	23.89	5.92	0.25
B.2	$q_c = -0.33 * z + 15.47$	N	24.59	5.36	0.22
B.3	$q_c = -0.51 * z + 8.66$	LN	24.82	6.99	0.28
B.4	$q_c = -0.18 * z + 21.40$	LN	26.81	7.00	0.26

Table D.2: Results of the trend removal in the Botlek sites.

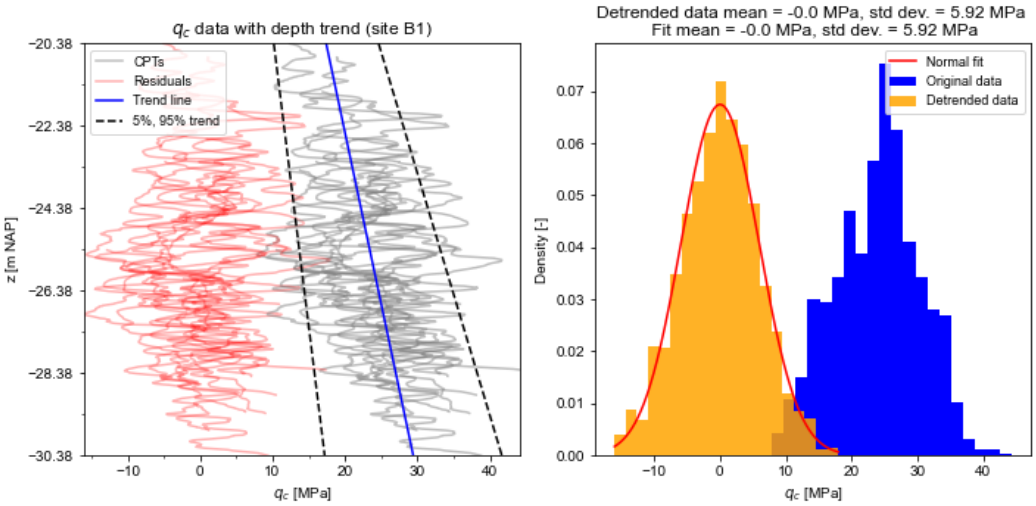

Figure D.5: Trend removal for group B1

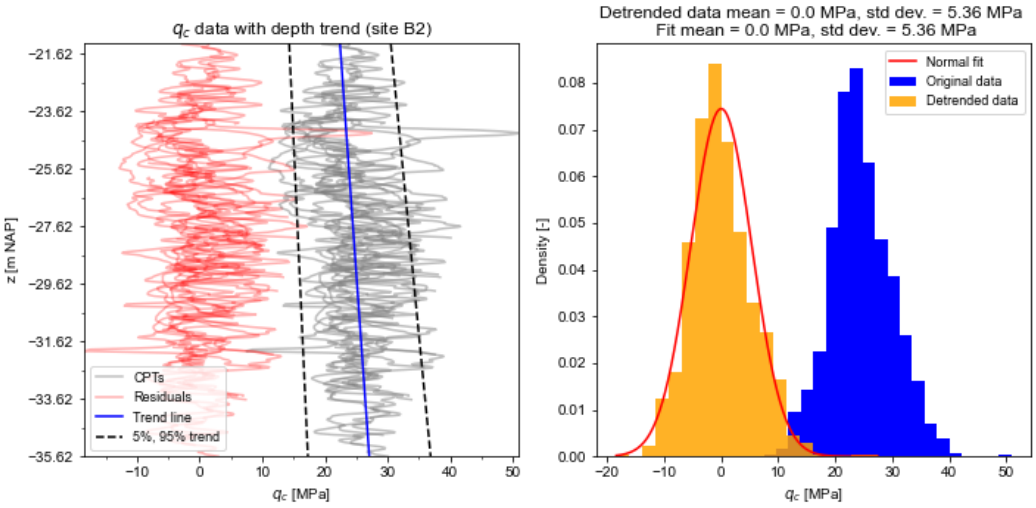

Figure D.6: Trend removal for group B2

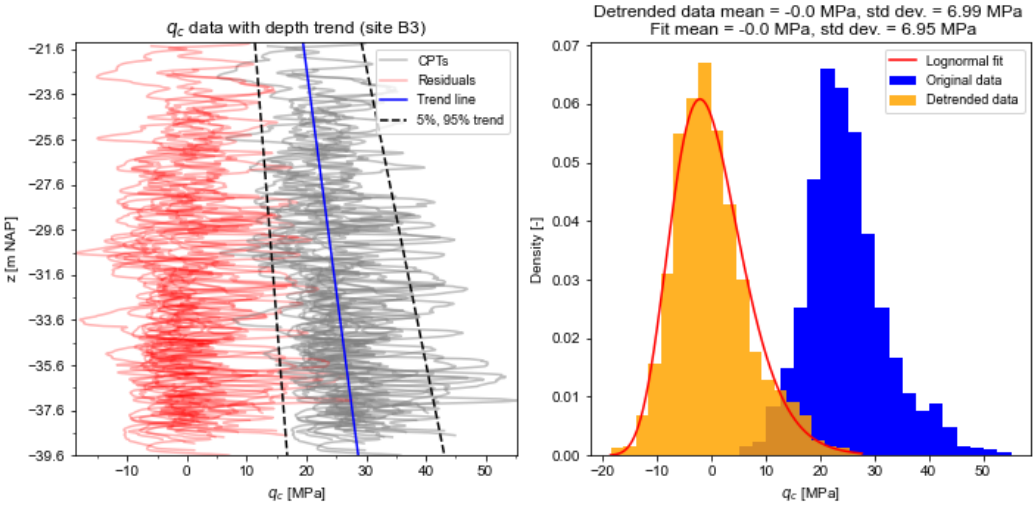

Figure D.7: Trend removal for group B3

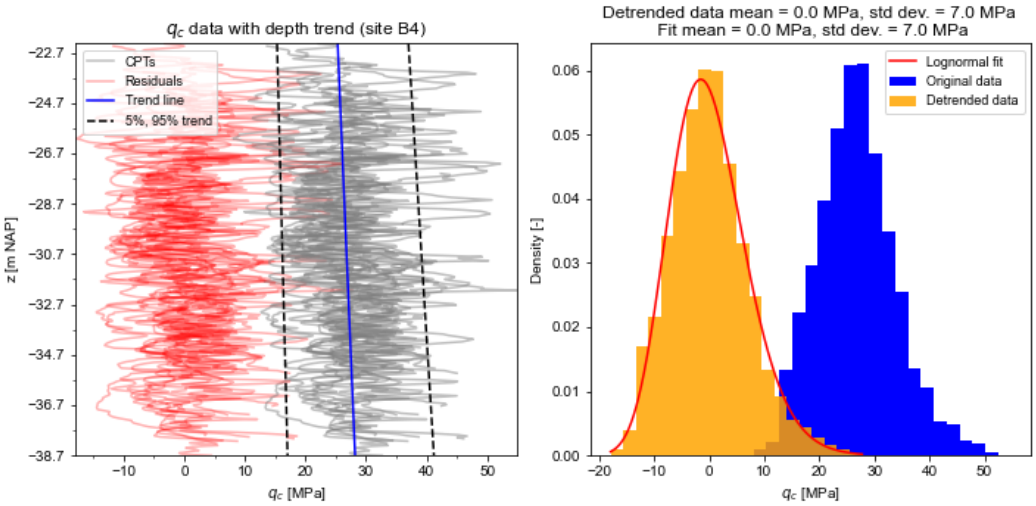

Figure D.8: Trend removal for group B4

Pernis

Group ID	$T(z)$ [MPa]	Distribution	μ [MPa]	σ [MPa]	c_v [-]
P.1	$q_c = 18.60$	N	18.60	5.70	0.31
P.2	$q_c = -0.30 * z + 13.17$	N	20.18	6.01	0.30
P.3	$q_c = 17.96$	N	17.96	4.10	0.23
P.4	$q_c = -0.30 * z + 11.82$	LN	18.64	4.17	0.22

Table D.3: Results of the trend removal in the Pernis sites.

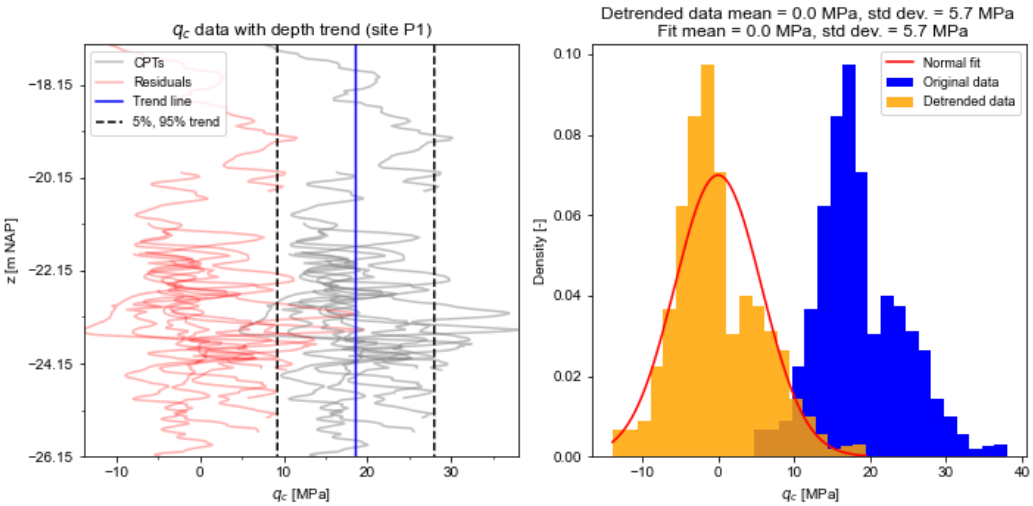

Figure D.9: Trend removal for group P1

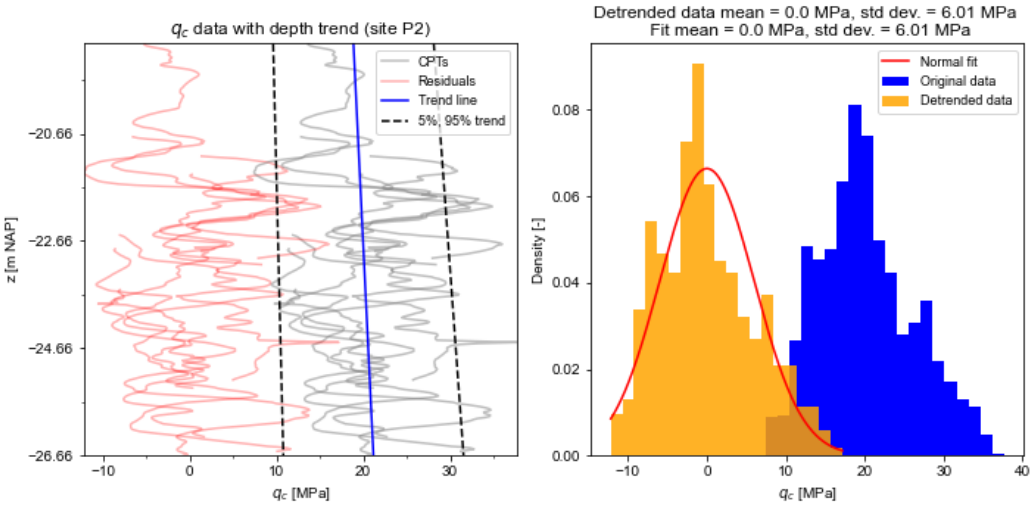

Figure D.10: Trend removal for group P2

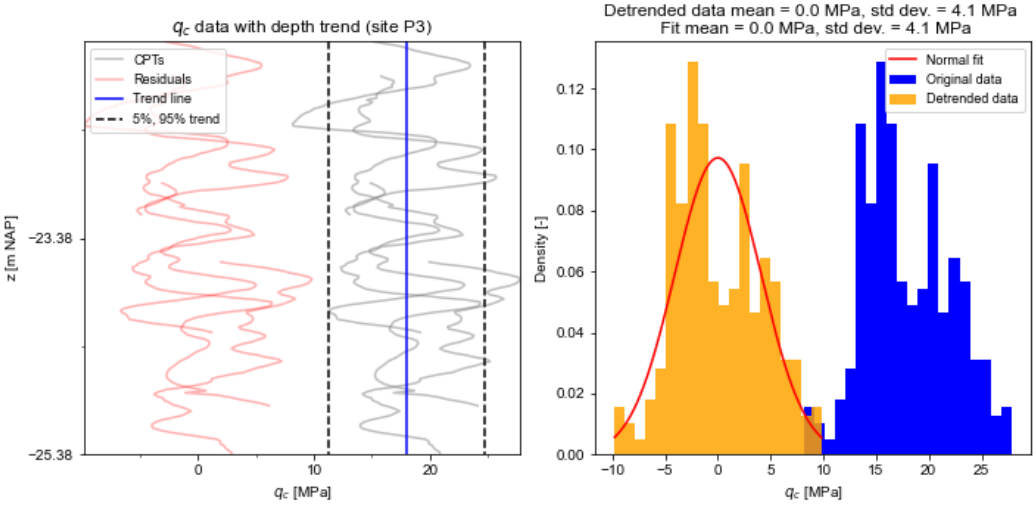

Figure D.11: Trend removal for group P3

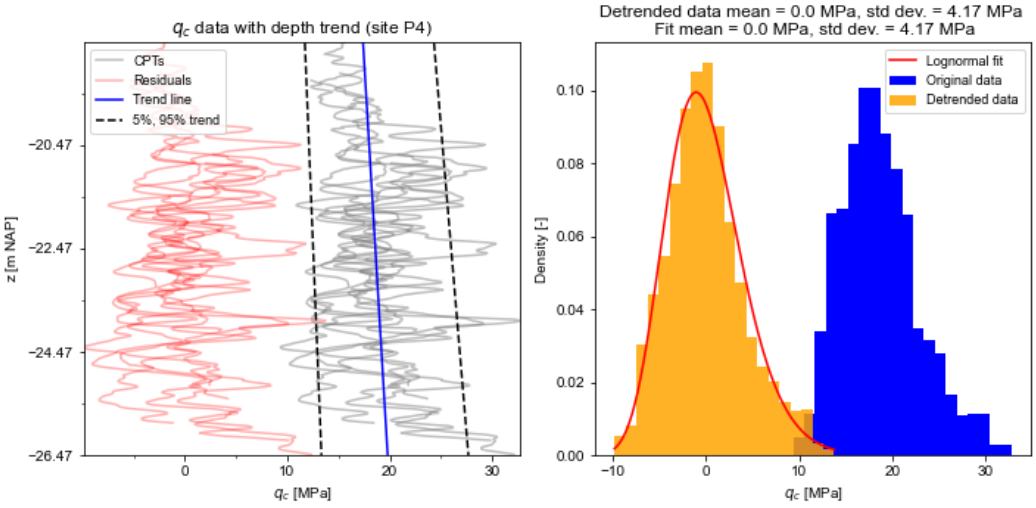

Figure D.12: Trend removal for group P4

D.2. Vertical scale of fluctuation

This section contains the tables and figures for the vertical scale of fluctuation for each site and individual CPTs.

Maasvlakte

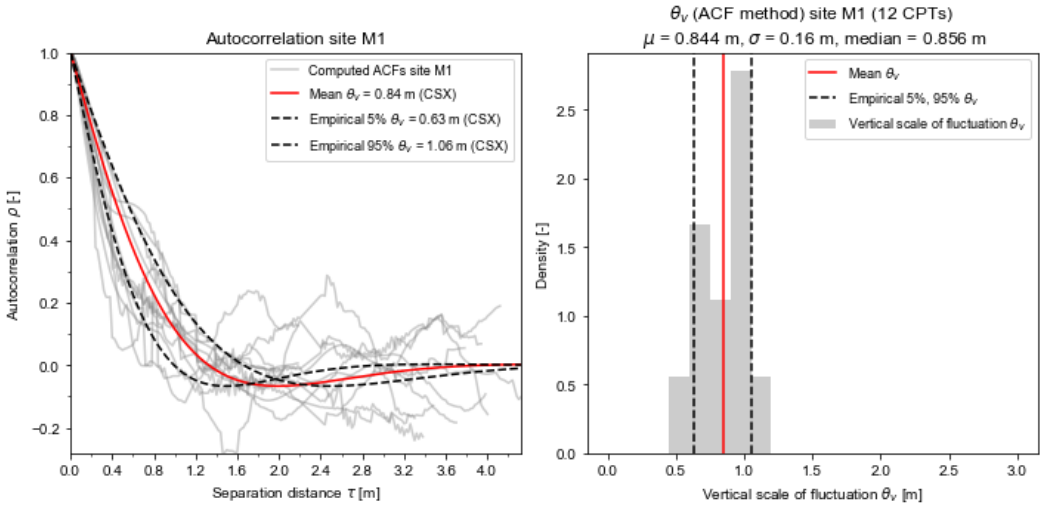

Figure D.13: Autocorrelation plot and histogram of site M1.

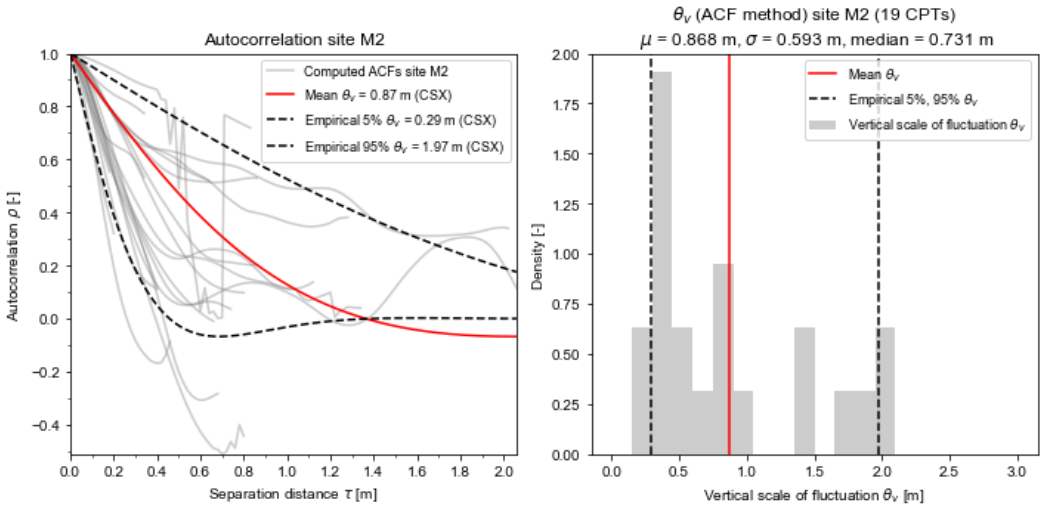

Figure D.14: Autocorrelation plot and histogram of site M2.

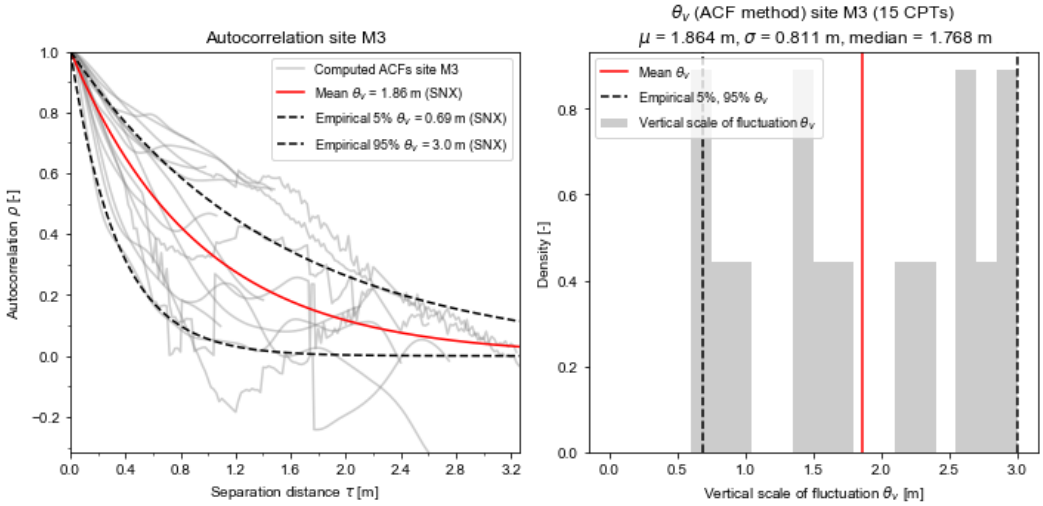

Figure D.15: Autocorrelation plot and histogram of site M3.

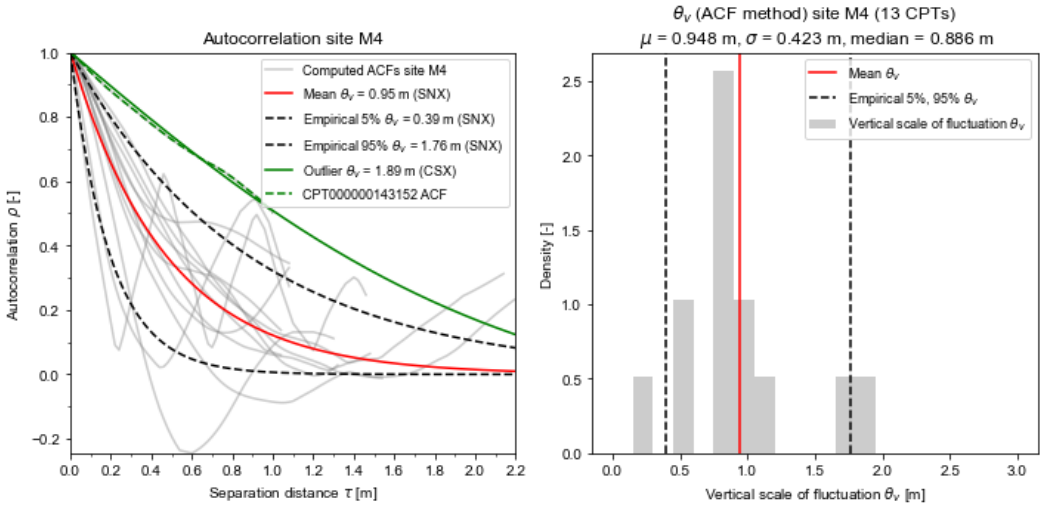

Figure D.16: Autocorrelation plot and histogram of site M4.

Botlek

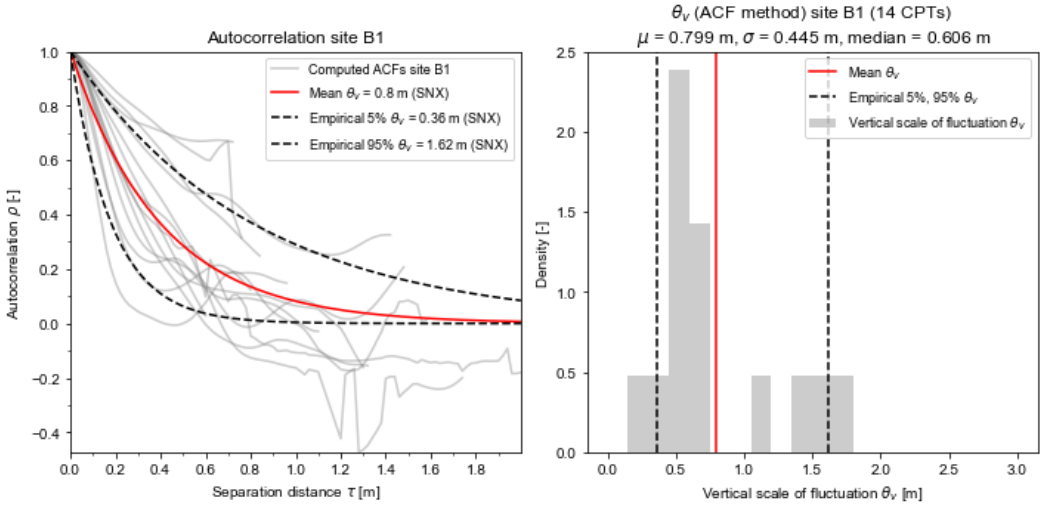

Figure D.17: Autocorrelation plot and histogram of site B1.

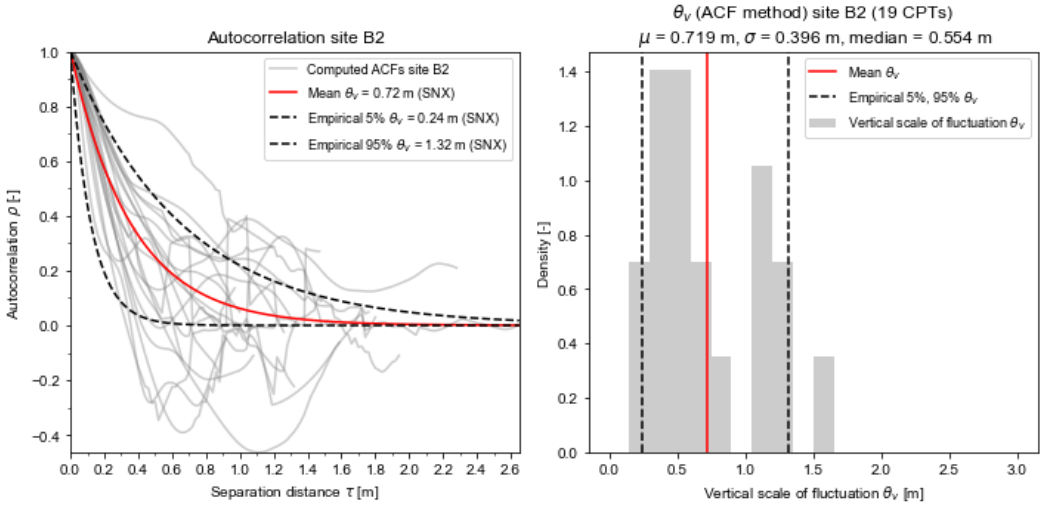

Figure D.18: Autocorrelation plot and histogram of site B2.

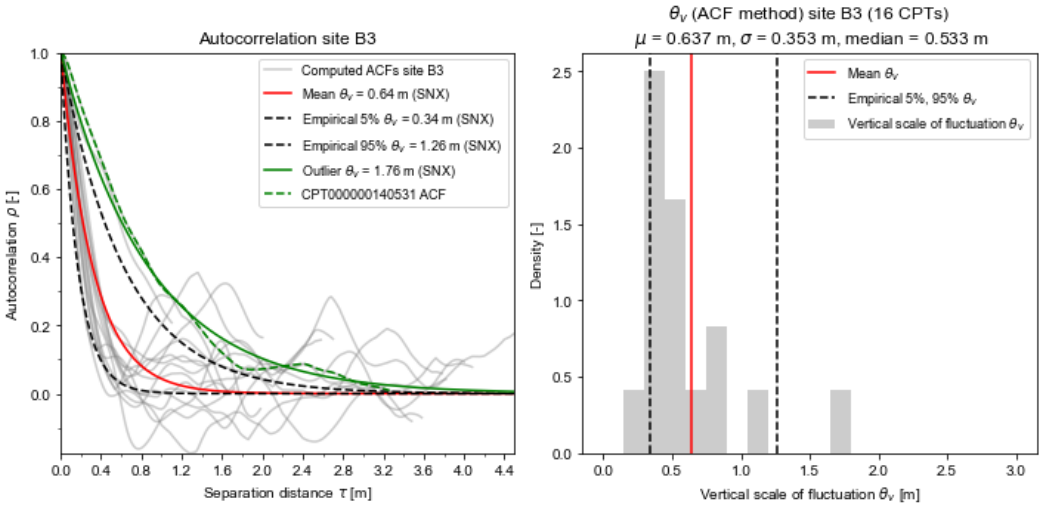

Figure D.19: Autocorrelation plot and histogram of site B3.

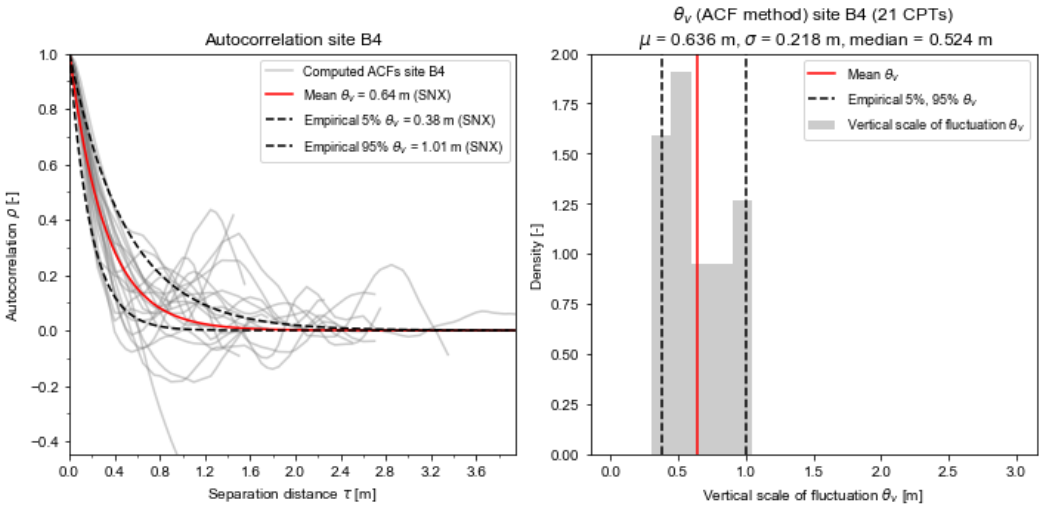

Figure D.20: Autocorrelation plot and histogram of site B4.

Pernis

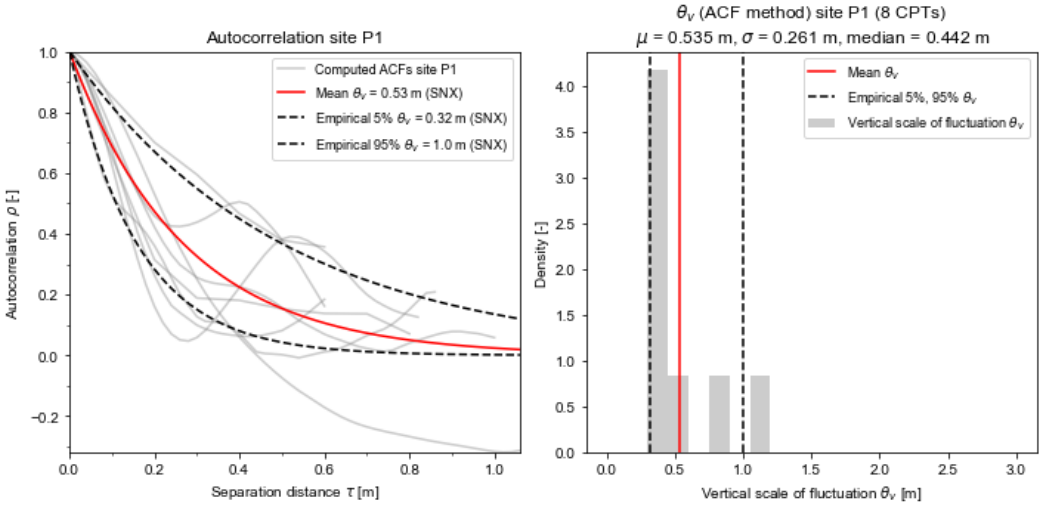

Figure D.21: Autocorrelation plot and histogram of site P1.

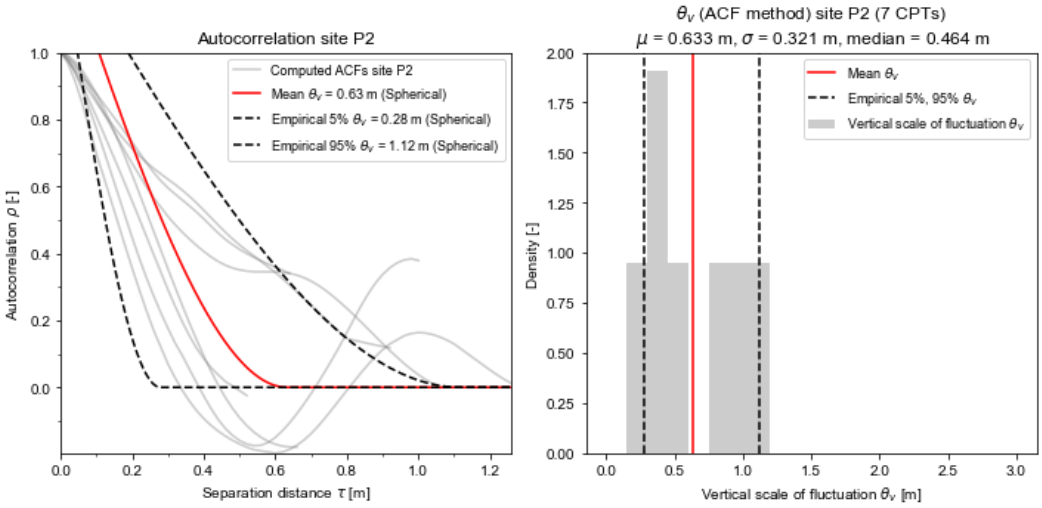

Figure D.22: Autocorrelation plot and histogram of site P2.

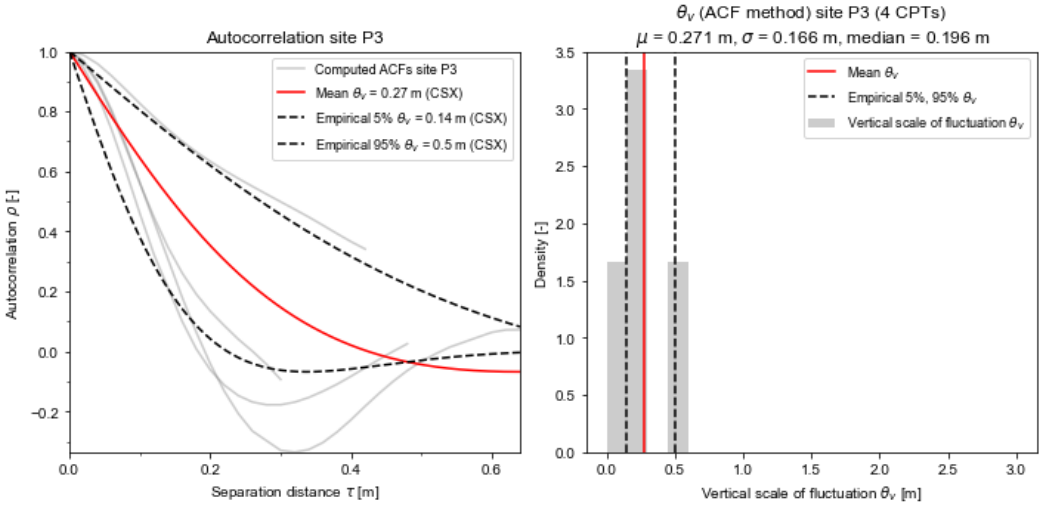

Figure D.23: Autocorrelation plot and histogram of site P3.

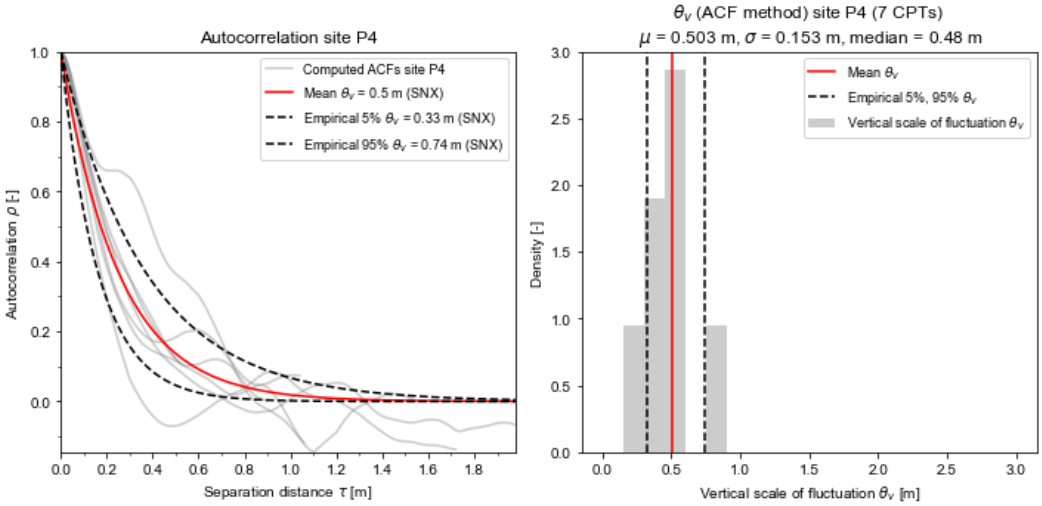

Figure D.24: Autocorrelation plot and histogram of site P4.

Individual CPTs

This section contain the tables for the vertical scale of fluctuation for each individual CPT.

CPT ID	θ_v [m]		CPT ID	θ_v [m]	
	ACF	Model		ACF	Model
CPT000000130993	0.88	CSX	CPT000000156212	1.37	SNX
CPT000000132169	1.18	SNX	CPT000000156214	0.81	SNX
CPT000000132692	1.67	SNX	CPT000000156222	0.96	SNX
CPT000000132746	0.29	CSX	CPT000000156227	3.00	SNX
CPT000000132990	0.94	SNX	CPT000000156228	0.69	Triangular
CPT000000134189	0.90	SNX	CPT000000156233	1.01	CSX
CPT000000140082	0.89	CSX	CPT000000156249	0.75	CSX
CPT000000140543	1.02	SNX	CPT000000156256	0.67	SNX
CPT000000142698	0.76	CSX	CPT000000156275	0.98	CSX
CPT000000143152	1.89	CSX	CPT000000156451	1.97	SNX
CPT000000146237	0.60	SNX	CPT000000156452	0.73	CSX
CPT000000147186	0.46	CSX	CPT000000156458	0.42	CSX
CPT000000147306	0.84	SNX	CPT000000156460	0.30	CSX
CPT000000155990	0.88	SQX	CPT000000156466	0.41	Triangular
CPT000000156016	0.70	SNX	CPT000000156472	1.76	SNX
CPT000000156041	1.01	SNX	CPT000000156475	1.97	CSX
CPT000000156058	1.41	SQX	CPT000000156476	1.03	SNX
CPT000000156091	2.18	SNX	CPT000000156482	0.77	SQX
CPT000000156106	2.56	CSX	CPT000000156491	0.80	SNX
CPT000000156120	1.64	Triangular	CPT000000156494	0.47	SQX
CPT000000156129	3.00	Triangular	CPT000000156498	0.29	Triangular
CPT000000156130	0.58	CSX	CPT000000156499	0.32	CSX
CPT000000156135	2.58	CSX	CPT000000156512 (0)	0.32	CSX
CPT000000156143	2.83	CSX	CPT000000156512 (1)	1.89	SNX
CPT000000156144	1.12	Triangular	CPT000000156517	0.26	Triangular
CPT000000156145	0.66	CSX	CPT000000156519	0.52	SQX
CPT000000156159	0.96	CSX	CPT000000156525	0.81	SNX
CPT000000156167	1.77	SNX	CPT000000156527	1.38	SQX
CPT000000156180	0.91	SNX	CPT000000156533 (0)	1.39	CSX
CPT000000156191	0.69	CSX	CPT000000156533 (1)	0.43	CSX
CPT000000156196	2.37	CSX			

Table D.4: Vertical scales of fluctuation for individual CPTs in the Maasvlakte.

CPT ID	θ_v [m]		CPT ID	θ_v [m]	
	ACF	Model		ACF	Model
CPT000000087531	1.70	SNX	CPT000000140531	1.76	SNX
CPT000000087532	1.57	CSX	CPT000000140632	0.27	CSX
CPT000000091781	1.08	SNX	CPT000000140863	0.75	SNX
CPT000000091782	1.08	SNX	CPT000000141556	1.05	SNX
CPT000000091784	0.24	CSX	CPT000000141676	0.68	SNX
CPT000000091785	1.28	SNX	CPT000000141902	0.45	Triangular
CPT000000091786	0.41	Triangular	CPT000000142443	0.49	CSX
CPT000000091790	0.44	CSX	CPT000000142481	0.52	SNX
CPT000000091791	0.24	CSX	CPT000000143085	0.42	SQX
CPT000000091795	1.13	SNX	CPT000000143723	0.73	SNX
CPT000000091799	0.33	CSX	CPT000000145368	0.85	SNX
CPT000000091800	0.49	SNX	CPT000000145450	0.46	SNX
CPT000000091801	0.53	CSX	CPT000000145558	0.42	SNX
CPT000000091804	1.64	SQX	CPT000000145626	0.77	SNX
CPT000000091806	0.30	CSX	CPT000000145634	0.78	SNX
CPT000000091807	0.87	SNX	CPT000000145998	0.72	SNX
CPT000000091808	1.20	SNX	CPT000000146636	0.44	SNX
CPT000000091809	0.61	CSX	CPT000000146786	0.43	CSX
CPT000000091810	0.71	SNX	CPT000000146869	0.46	Triangular
CPT000000091811	0.51	SQX	CPT000000146928	0.60	SNX
CPT000000091814	0.55	CSX	CPT000000147207	0.57	Triangular

CPT000000097366	0.60	SNX	CPT000000147221	0.73	SNX
CPT000000130642	0.49	SNX	CPT000000147556	0.76	SNX
CPT000000130968	0.58	SNX	CPT000000147882	1.09	CSX
CPT000000130982	0.45	CSX	CPT000000156354	0.56	CSX
CPT000000131904	0.50	SNX	CPT000000156355	0.25	SQX
CPT000000132170	0.39	CSX	CPT000000156358	0.71	CSX
CPT000000132368	0.38	CSX	CPT000000156364	0.68	SNX
CPT000000132891	0.37	CSX	CPT000000156370	0.53	CSX
CPT000000133208	0.95	SNX	CPT000000156372	0.48	SNX
CPT000000133214	0.37	Triangular	CPT000000156376	1.46	Triangular
CPT000000133221	1.01	SNX	CPT000000156384	0.42	CSX
CPT000000133522	0.98	SNX	CPT000000156388	1.10	Triangular
CPT000000133821	0.42	CSX	CPT000000156395	0.61	Triangular
CPT000000133845	0.48	SQX	CPT000000156401	0.53	SNX

Table D.5: Vertical scales of fluctuation for individual CPTs in the Botlek.

CPT ID	θ_v [m]		CPT ID	θ_v [m]	
	ACF	Model		ACF	Model
CPT000000130932	0.15	CSX	CPT000000144494	0.44	SNX
CPT000000130956	0.55	CSX	CPT000000144681	0.81	SNX
CPT000000133438	0.14	CSX	CPT000000145890	1.10	SNX
CPT000000140125	0.24	SQX	CPT000000145969	0.45	SNX
CPT000000140814	0.34	CSX	CPT000000150567	0.34	SNX
CPT000000141380	0.76	CSX	CPT000000150577	0.50	SNX
CPT000000141532	0.24	CSX	CPT000000155906	0.48	SNX
CPT000000141803	0.46	Triangular	CPT000000155919	0.29	Triangular
CPT000000142179	0.31	SQX	CPT000000155925	0.44	SNX
CPT000000142322	1.18	SNX	CPT000000155932	0.82	Triangular
CPT000000143102	0.98	SNX	CPT000000155992	0.53	SNX
CPT000000143203	0.44	Triangular	CPT000000156001	0.56	SNX
CPT000000143237	0.37	Triangular	CPT000000156007	0.41	CSX

Table D.6: Vertical scales of fluctuation for individual CPTs in Pernis.

D.3. Pile base capacities

This chapter is divided into three parts. The first part shows a few pictures of the generated fields and how the pile base capacities were computed. The second part shows the plots of the coefficients of variation of pile base capacities and the third part shows histograms of the computed pile base capacities.

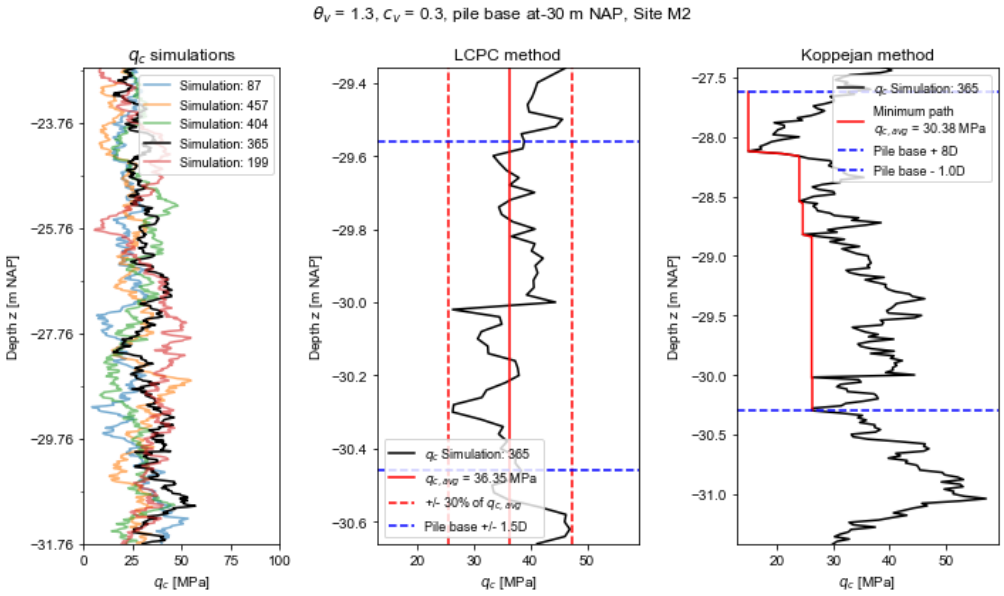

Figure D.25: Site M2 random field of cone resistances with the LCPC and Koppejan method.

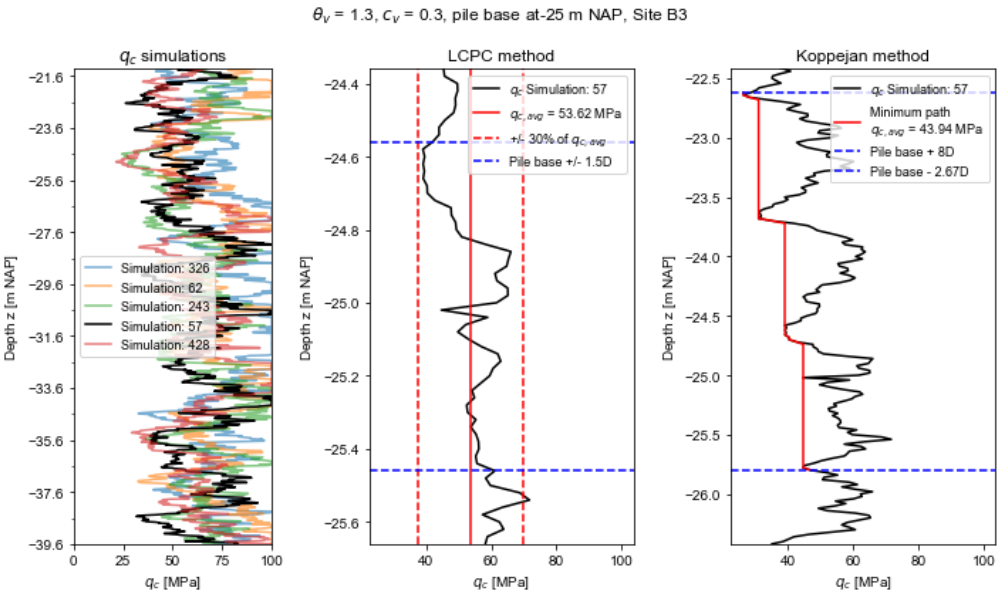

Figure D.26: Site B3 random field of cone resistances with the LCPC and Koppejan method.

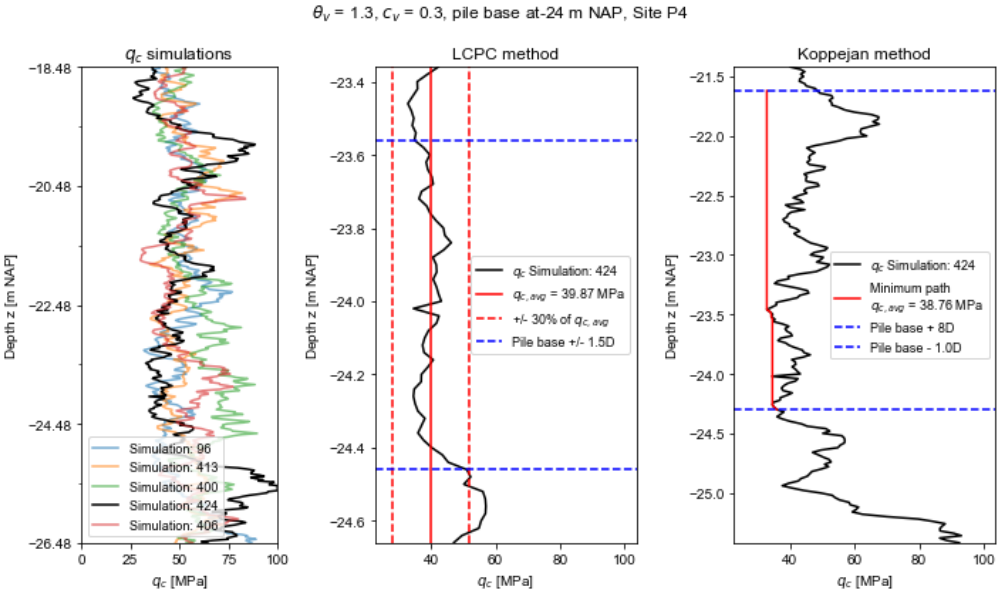

Figure D.27: Site P4 random field of cone resistances with the LCPC and Koppejan method.

D.3.1. Comparison averaging methods in pile base capacity uncertainty

Maasvlakte

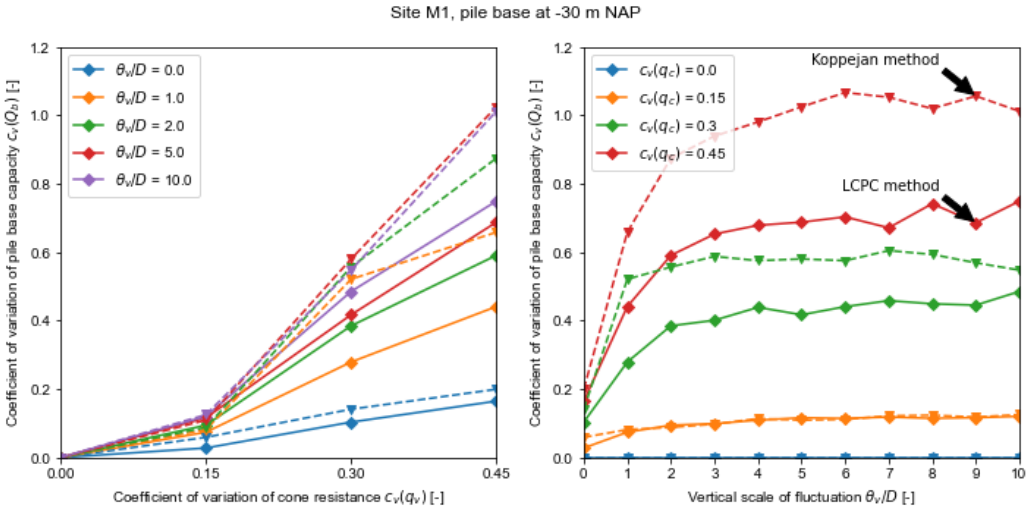

Figure D.28: Site M1 coefficients of variation of pile base capacity.

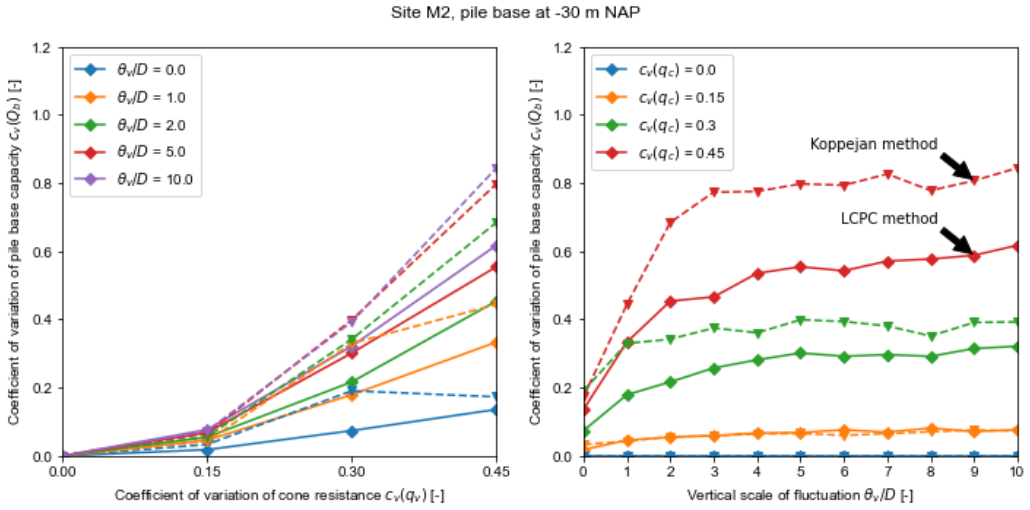

Figure D.29: Site M2 coefficients of variation of pile base capacity.

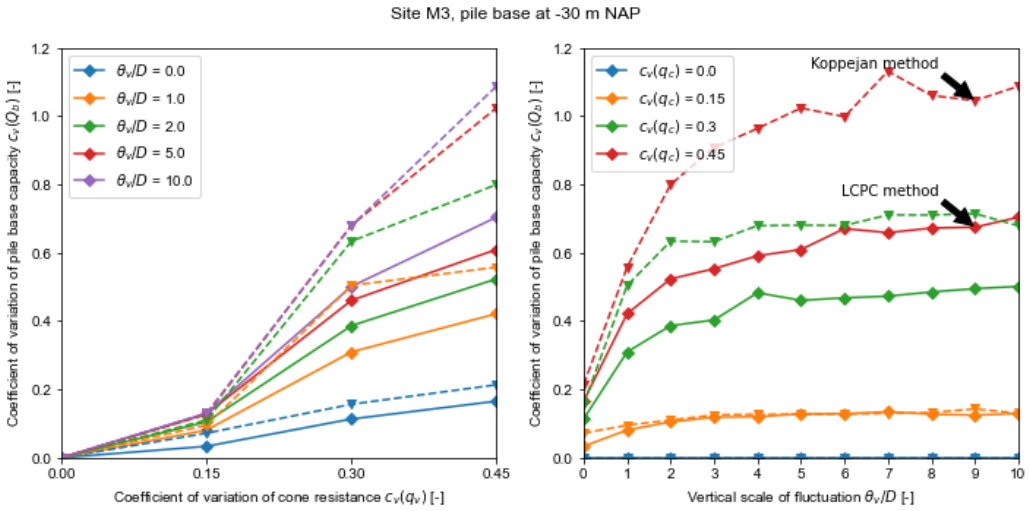

Figure D.30: Site M3 coefficients of variation of pile base capacity.

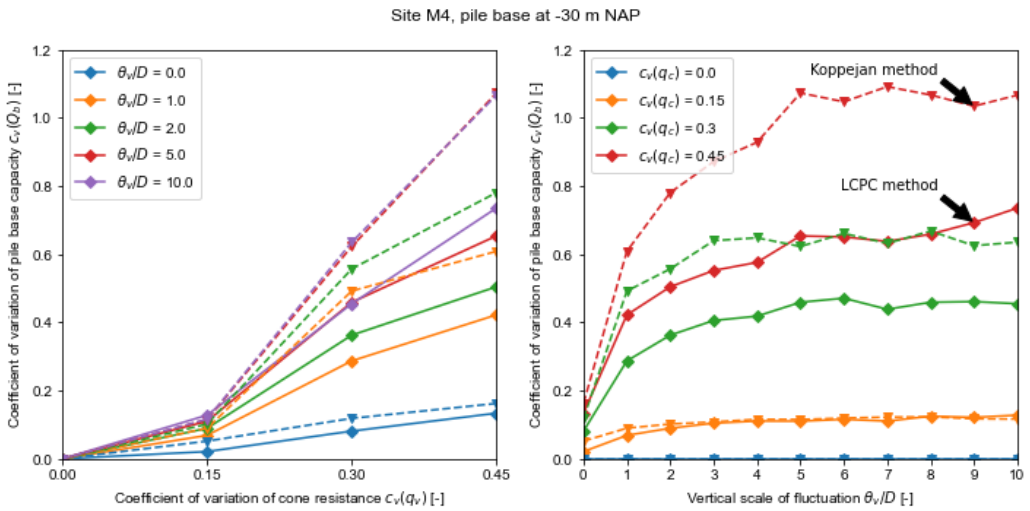

Figure D.31: Site M4 coefficients of variation of pile base capacity.

Botlek

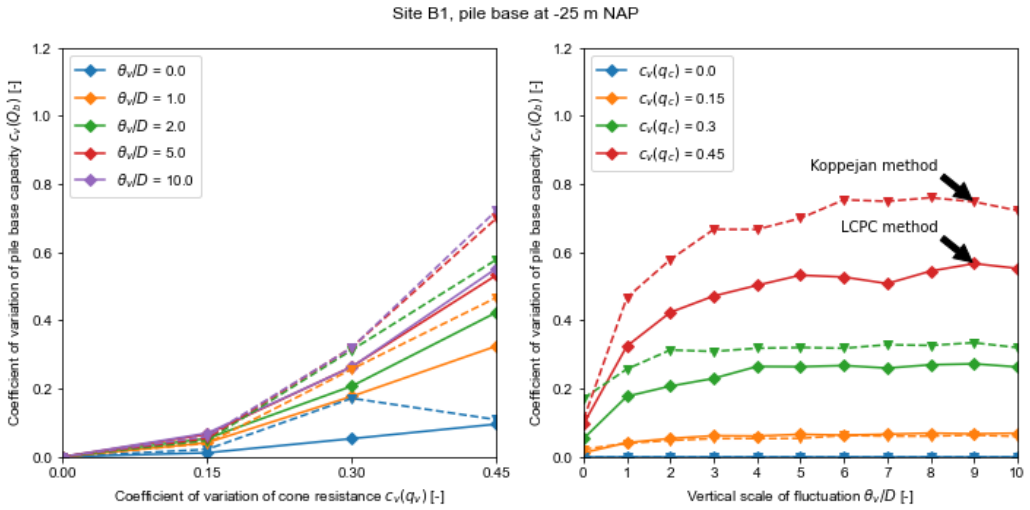

Figure D.32: Site B1 coefficients of variation of pile base capacity.

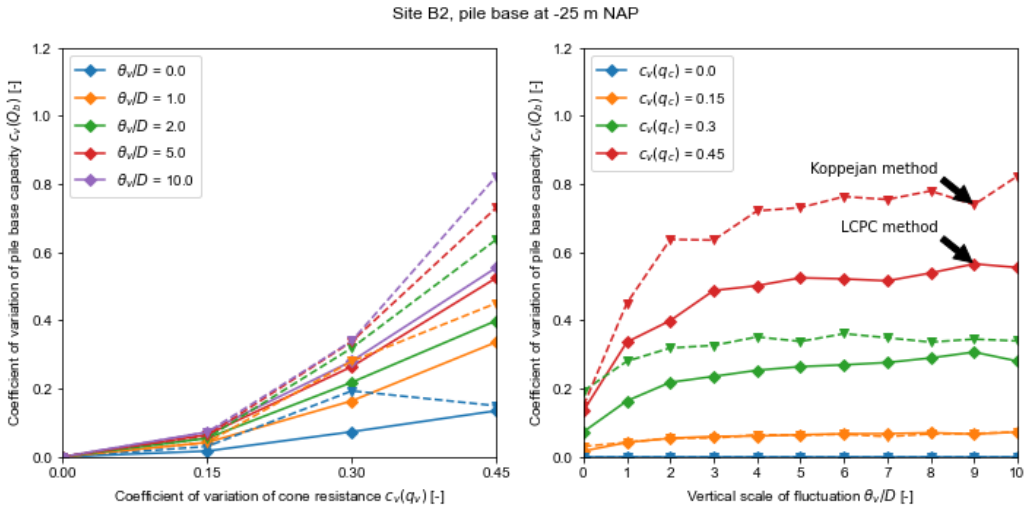

Figure D.33: Site B2 coefficients of variation of pile base capacity.

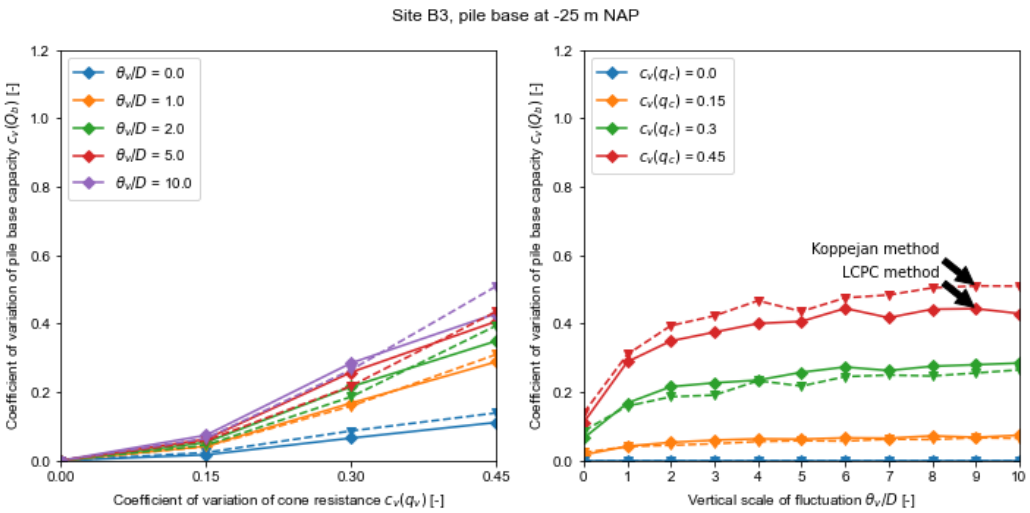

Figure D.34: Site B3 coefficients of variation of pile base capacity.

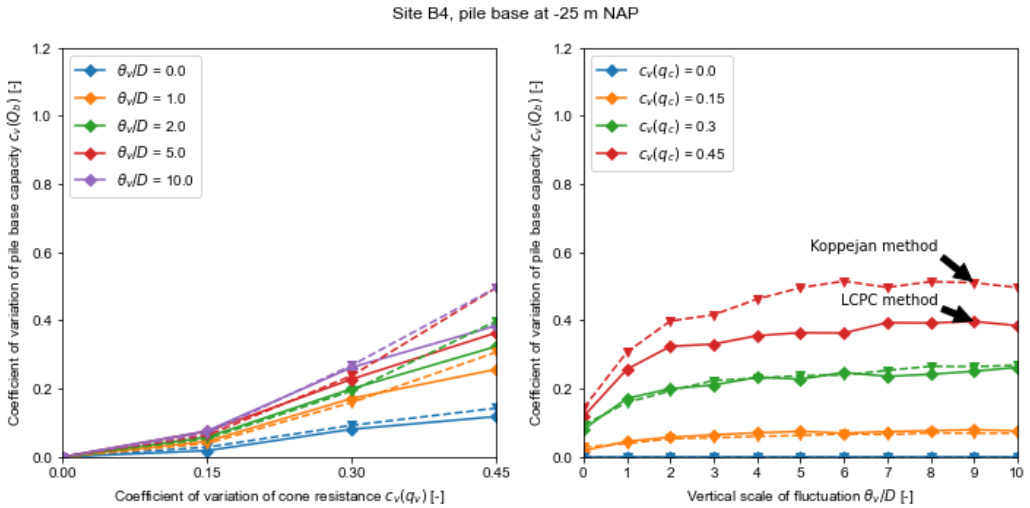

Figure D.35: Site B4 coefficients of variation of pile base capacity.

Pernis

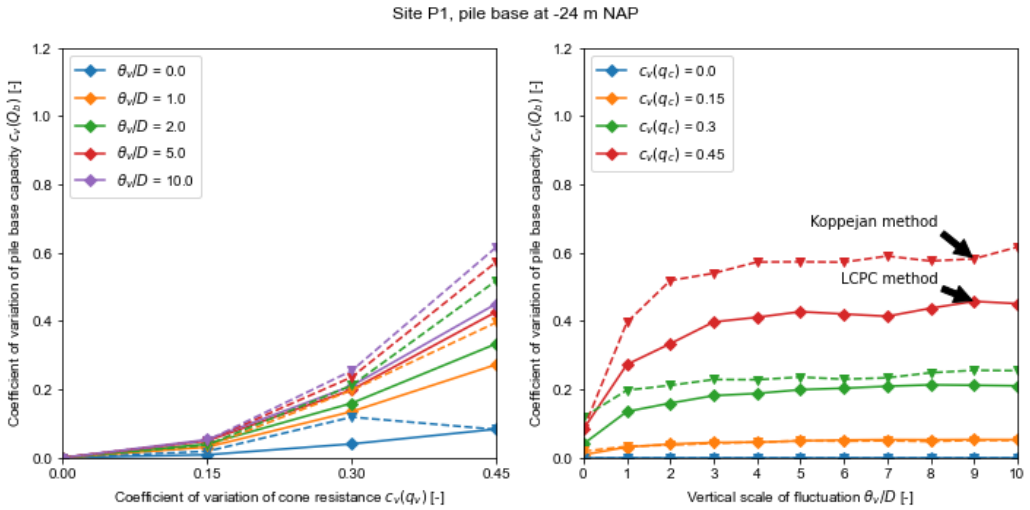

Figure D.36: Site P1 coefficients of variation of pile base capacity.

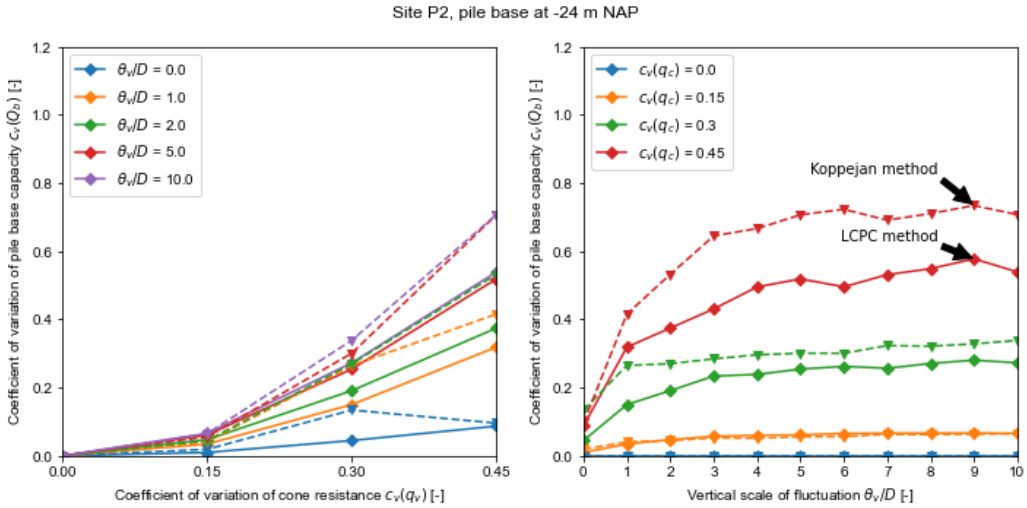

Figure D.37: Site P2 coefficients of variation of pile base capacity.

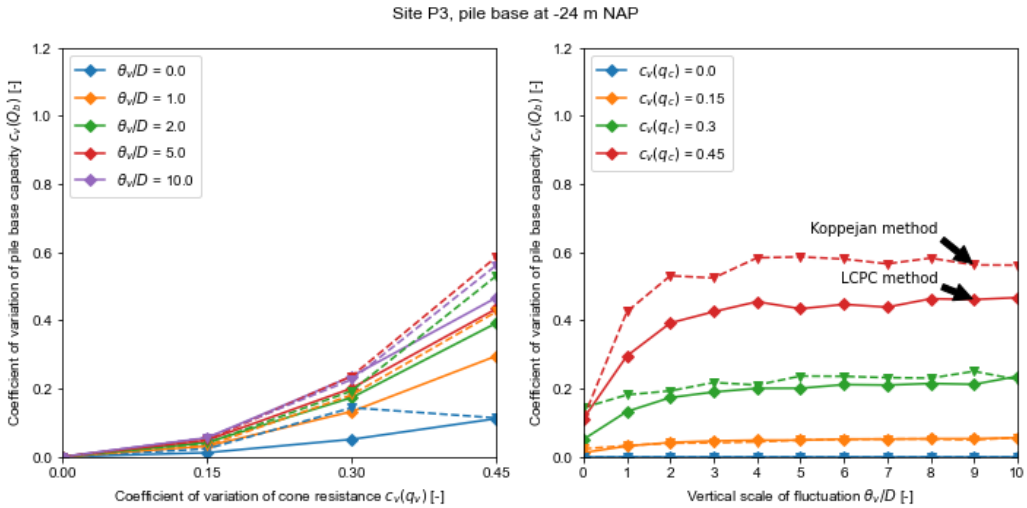

Figure D.38: Site P3 coefficients of variation of pile base capacity.

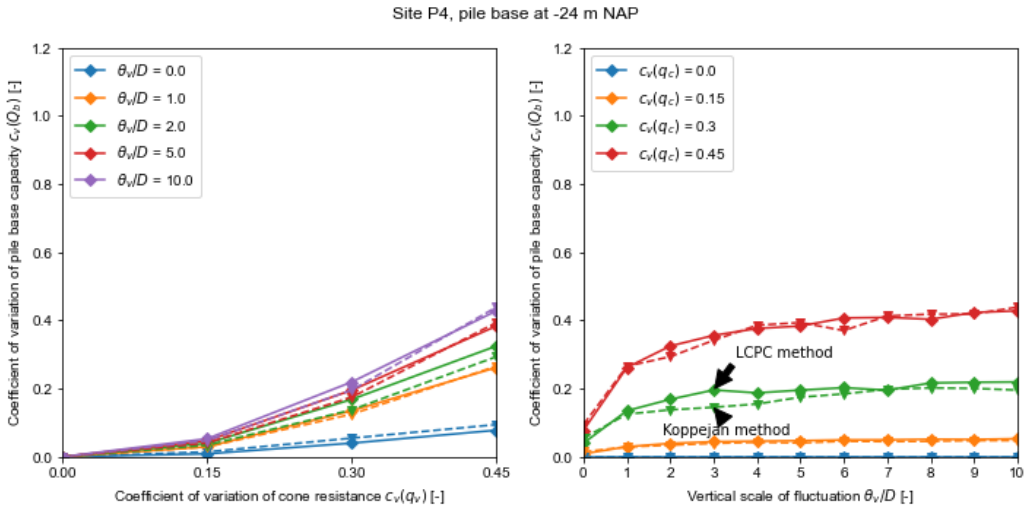

Figure D.39: Site P4 coefficients of variation of pile base capacity.

D.3.2. Pile base capacities

The pile base capacities were computed with the coefficient of variation of cone resistance being 0.3.

Maasvlakte

Site M1

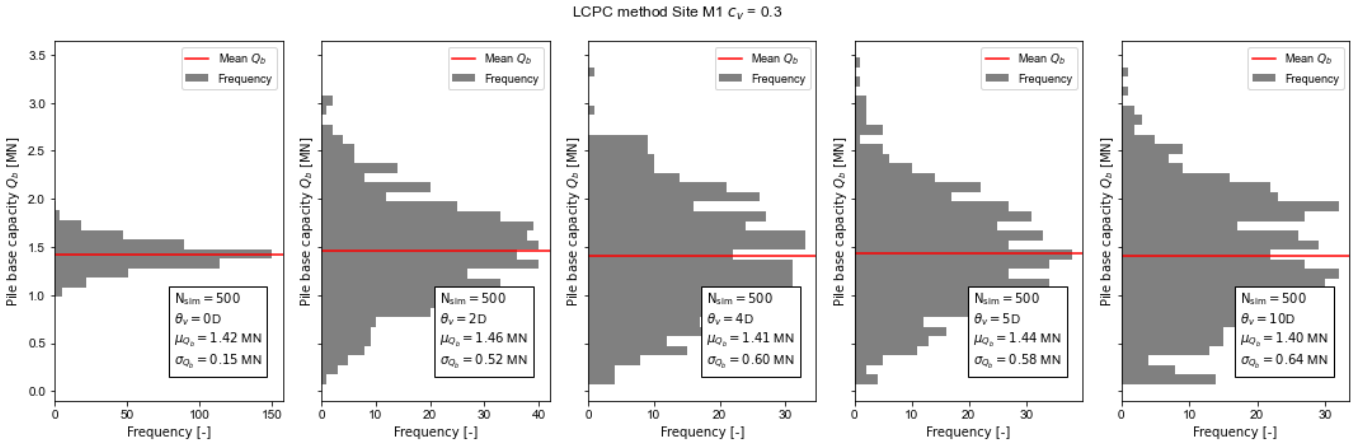

Figure D.40: Pile base capacities at site M1 for different vertical scales of fluctuation using LCPC method.

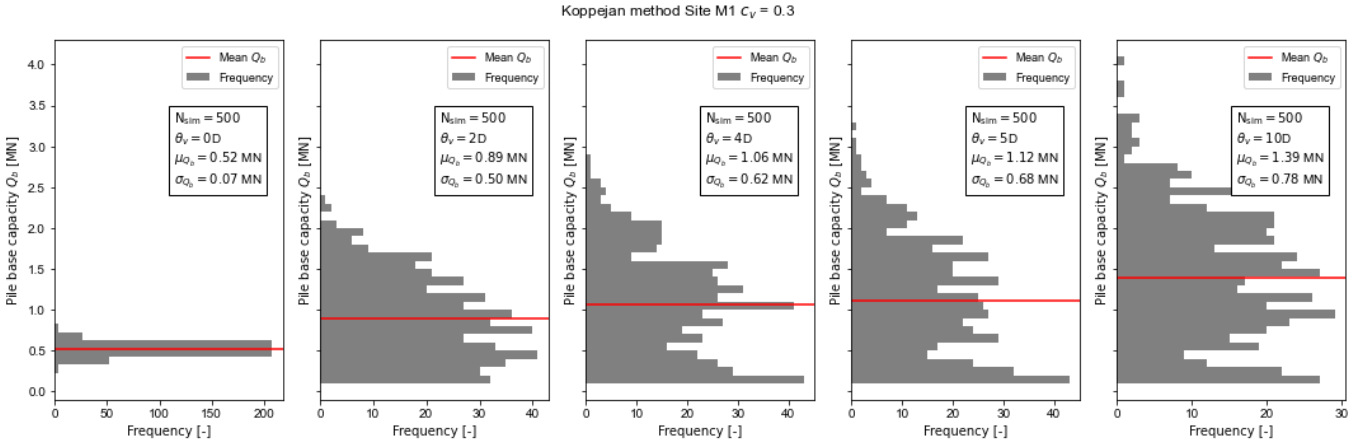

Figure D.41: Pile base capacities at site M1 for different vertical scales of fluctuation using Koppejan method.

Site M2

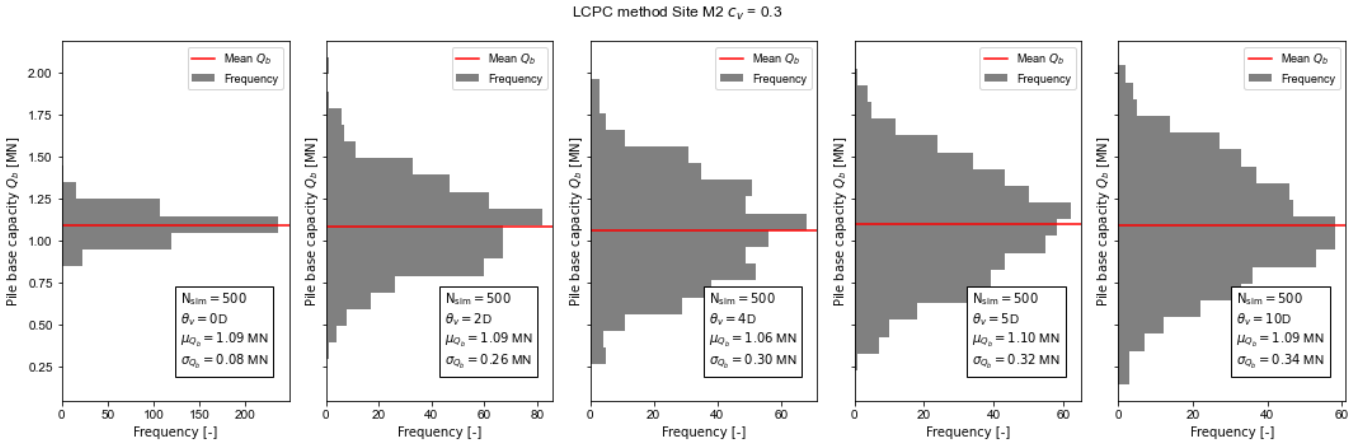

Figure D.42: Pile base capacities at site M2 for different vertical scales of fluctuation using LCPC method.

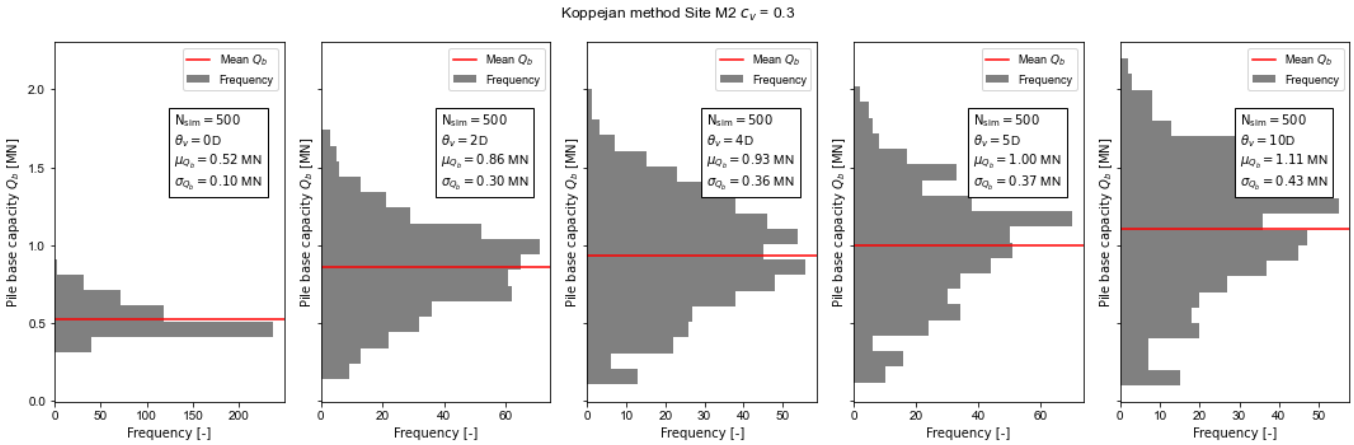

Figure D.43: Pile base capacities at site M2 for different vertical scales of fluctuation using Koppejan method.

Site M3

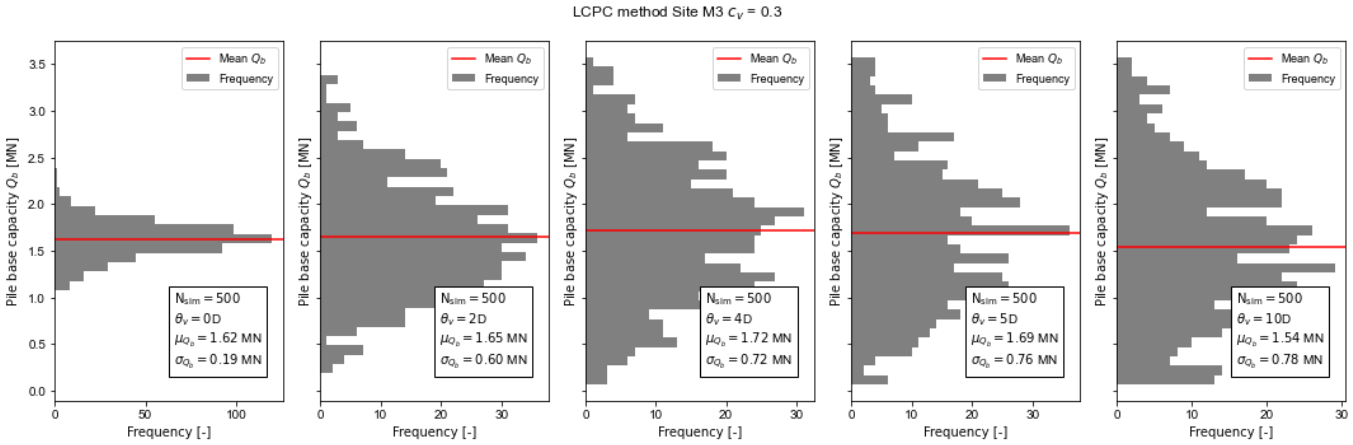

Figure D.44: Pile base capacities at site M3 for different vertical scales of fluctuation using LCPC method.

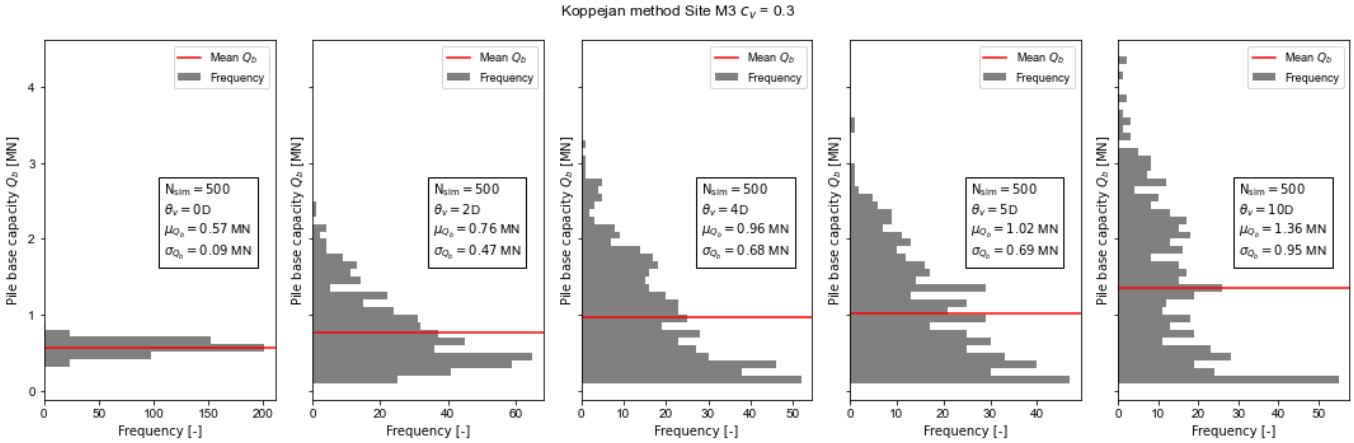

Figure D.45: Pile base capacities at site M3 for different vertical scales of fluctuation using Koppejan method.

Site M4

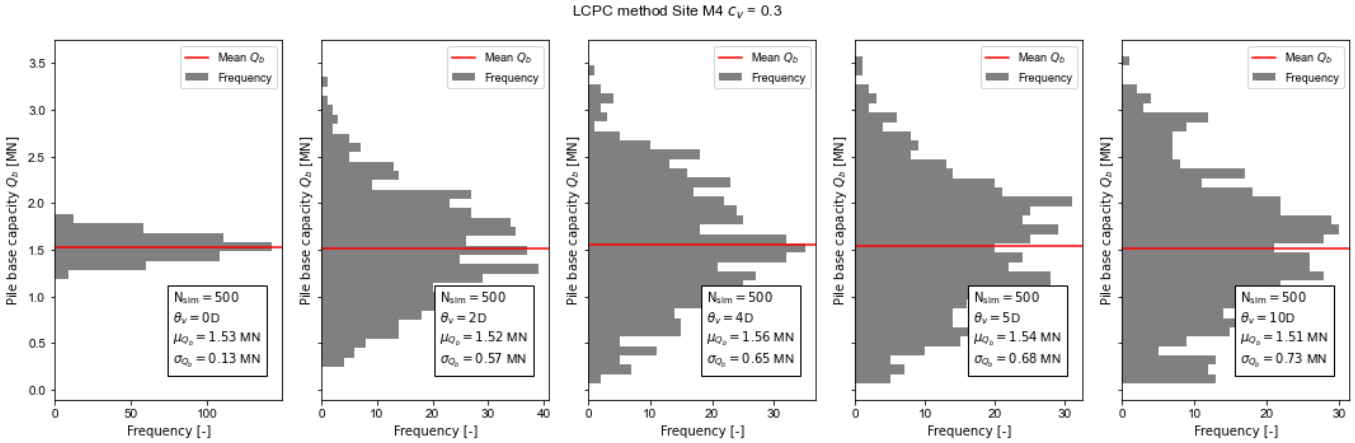

Figure D.46: Pile base capacities at site M4 for different vertical scales of fluctuation using LCPC method.

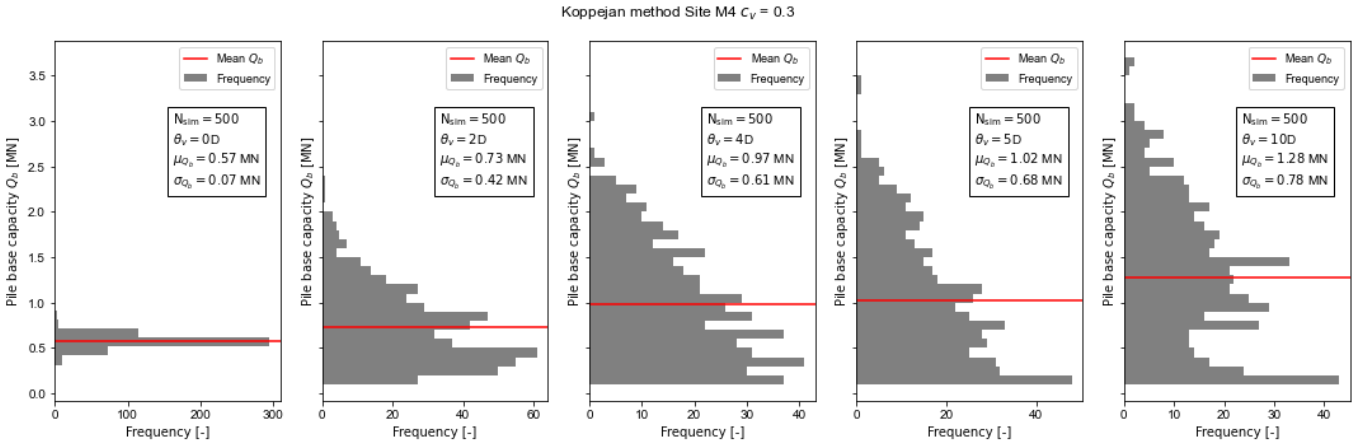

Figure D.47: Pile base capacities at site M4 for different vertical scales of fluctuation using Koppejan method.

Botlek

Site B1

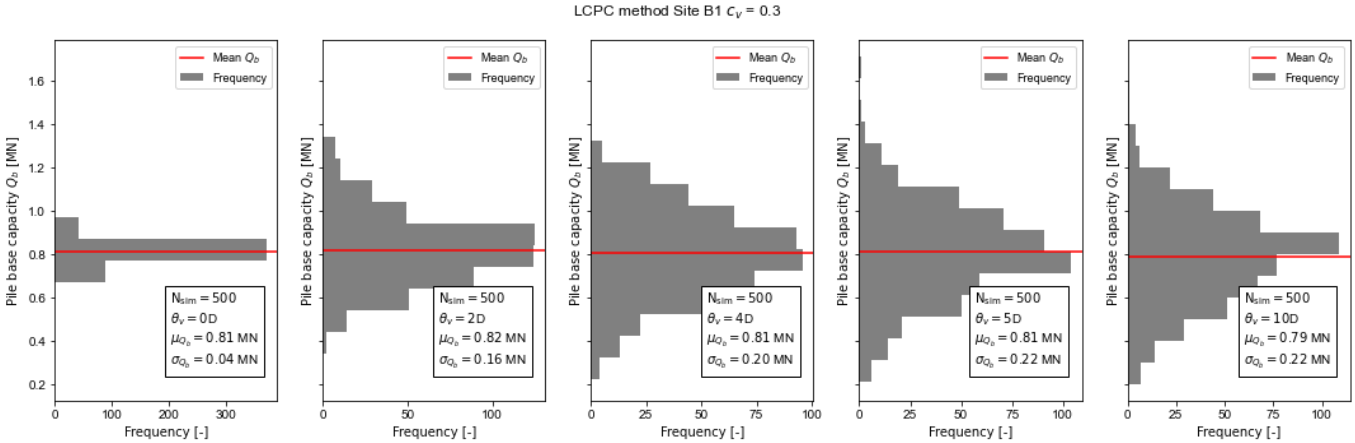

Figure D.48: Pile base capacities at site B1 for different vertical scales of fluctuation using LCPC method.

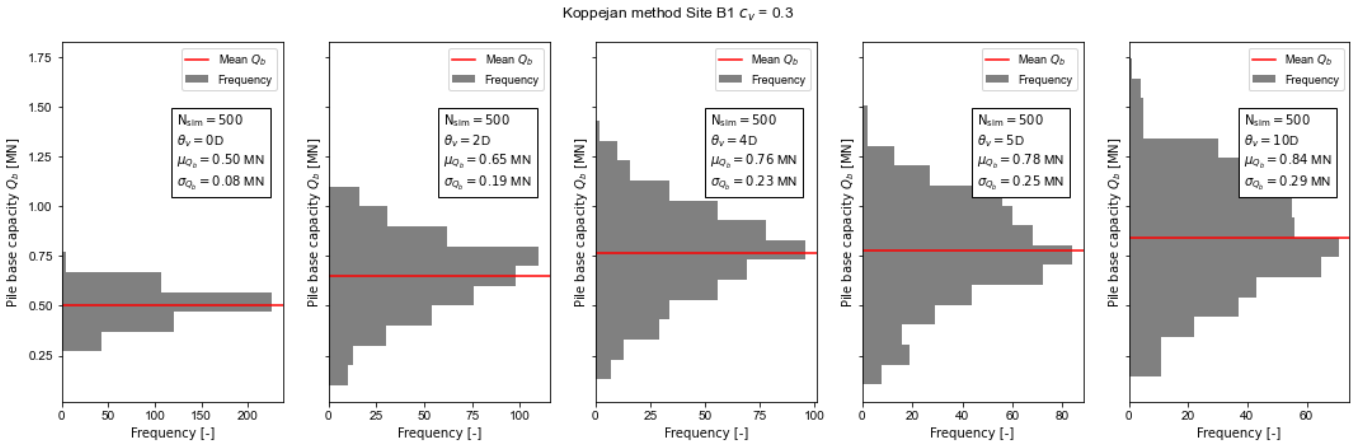

Figure D.49: Pile base capacities at site B1 for different vertical scales of fluctuation using Koppejan method.

Site B2

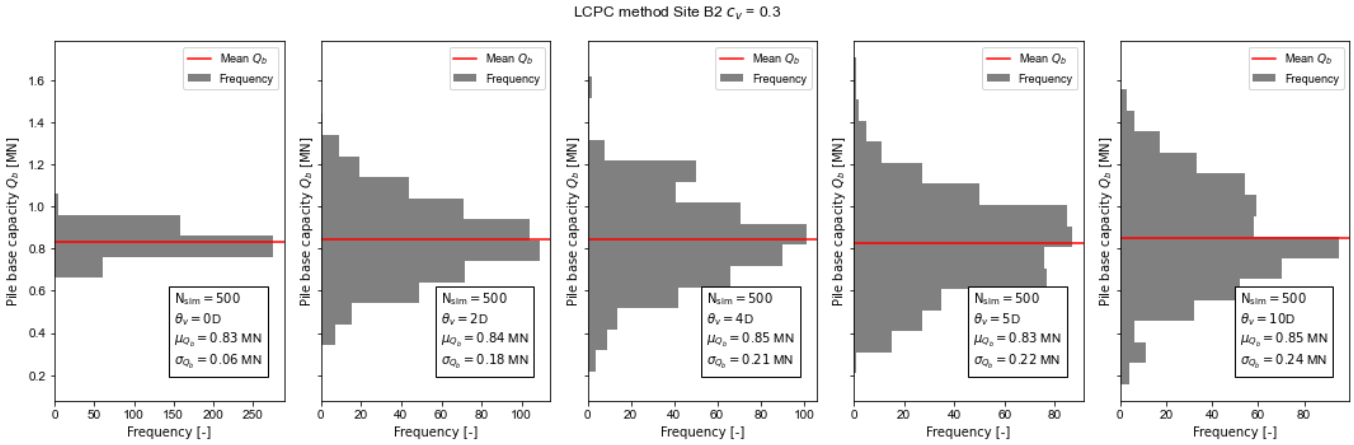

Figure D.50: Pile base capacities at site B2 for different vertical scales of fluctuation using LCPC method.

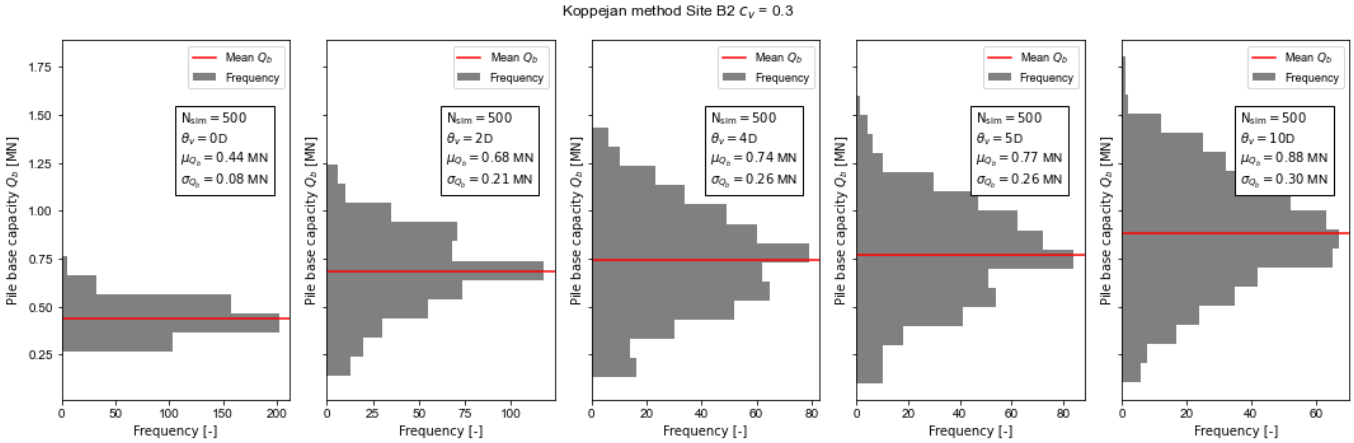

Figure D.51: Pile base capacities at site B2 for different vertical scales of fluctuation using Koppejan method.

Site B3

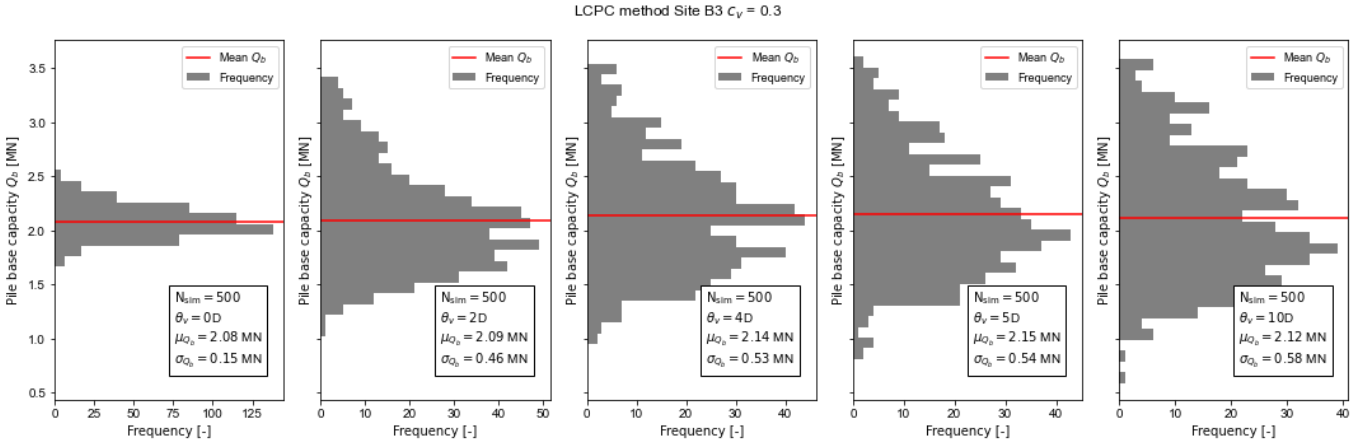

Figure D.52: Pile base capacities at site B3 for different vertical scales of fluctuation using LCPC method.

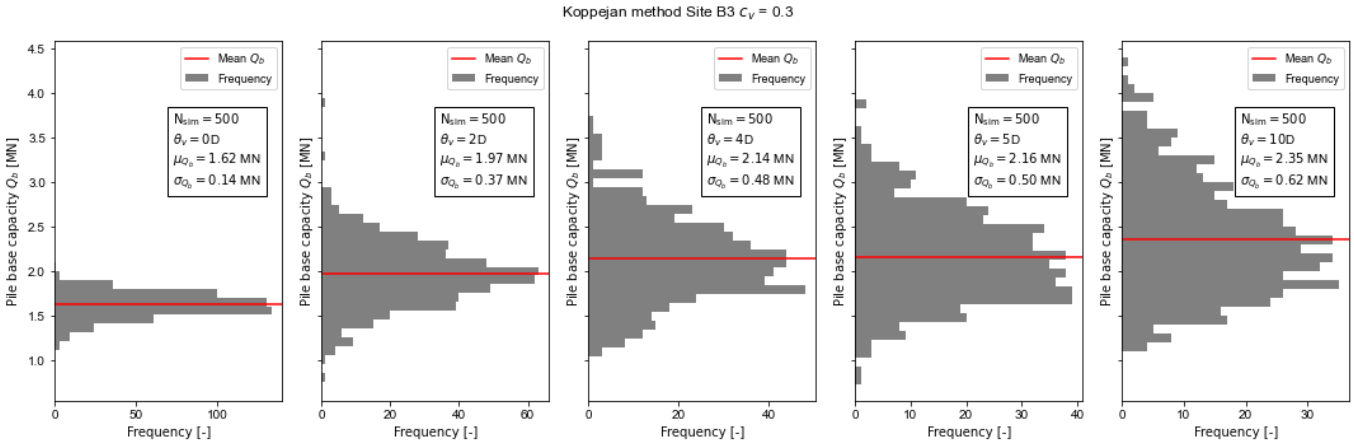

Figure D.53: Pile base capacities at site B3 for different vertical scales of fluctuation using Koppejan method.

Site B4

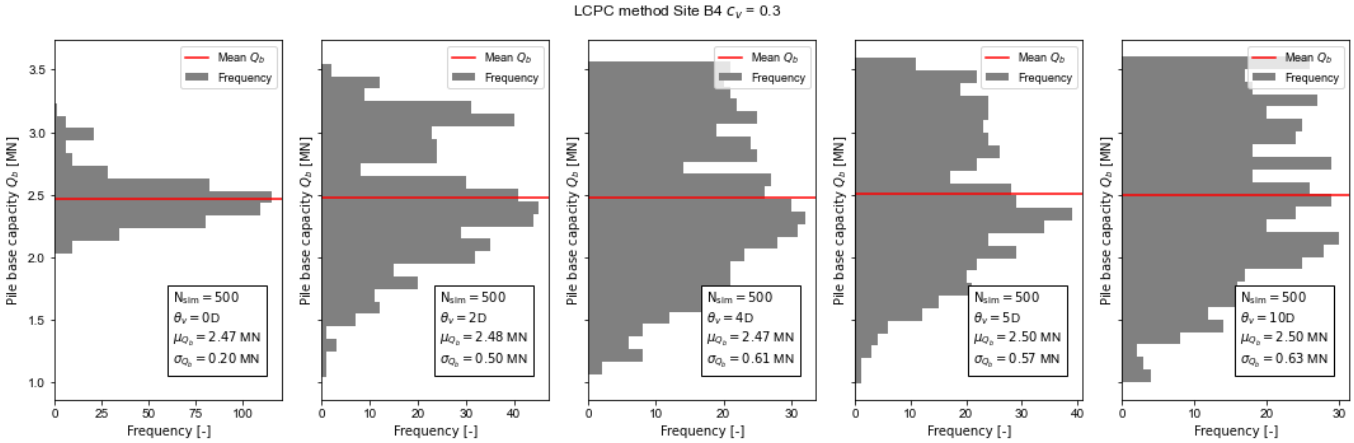

Figure D.54: Pile base capacities at site B4 for different vertical scales of fluctuation using LCPC method.

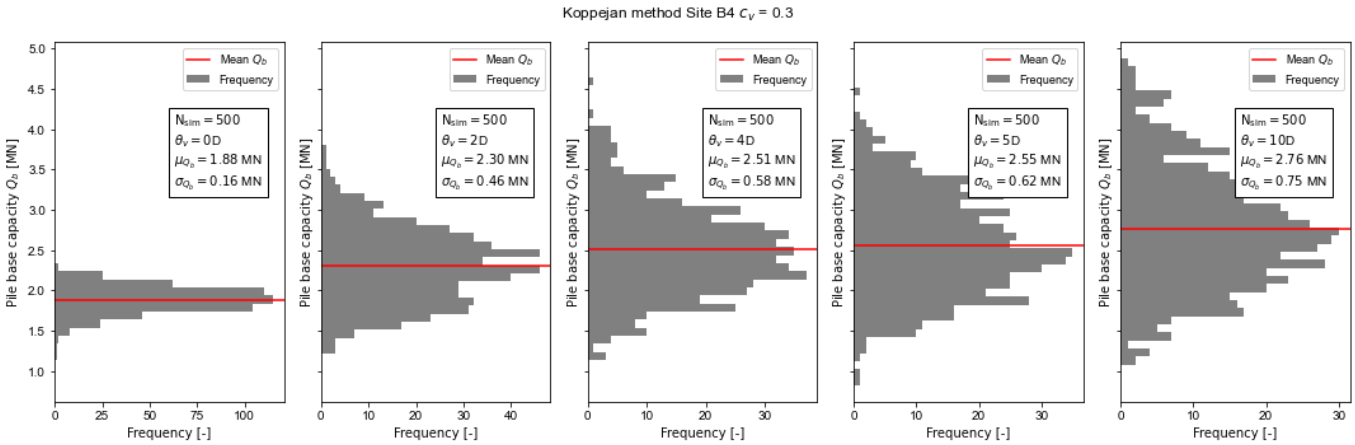

Figure D.55: Pile base capacities at site B4 for different vertical scales of fluctuation using Koppejan method.

Pernis

Site P1

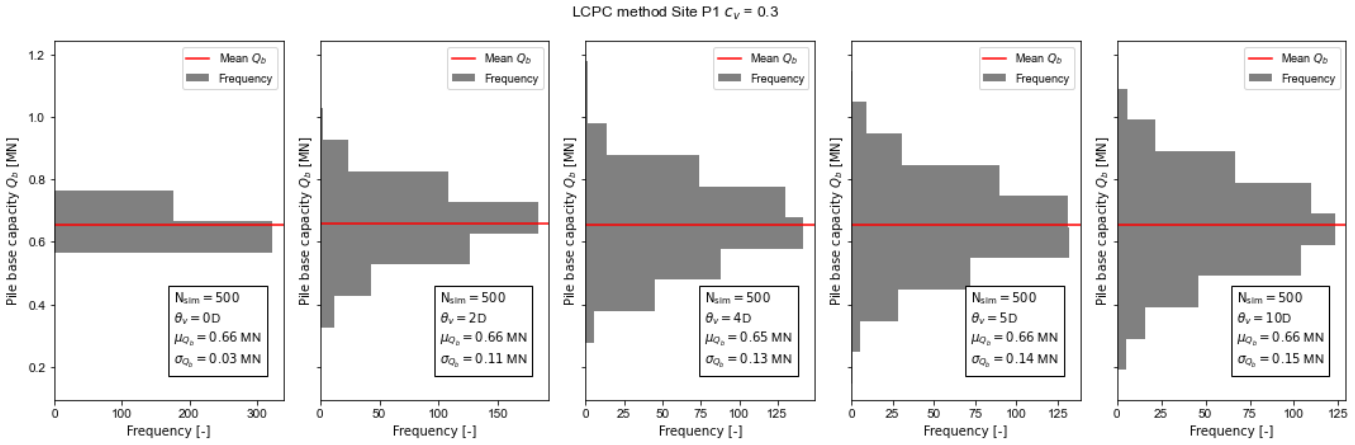

Figure D.56: Pile base capacities at site P1 for different vertical scales of fluctuation using LCPC method.

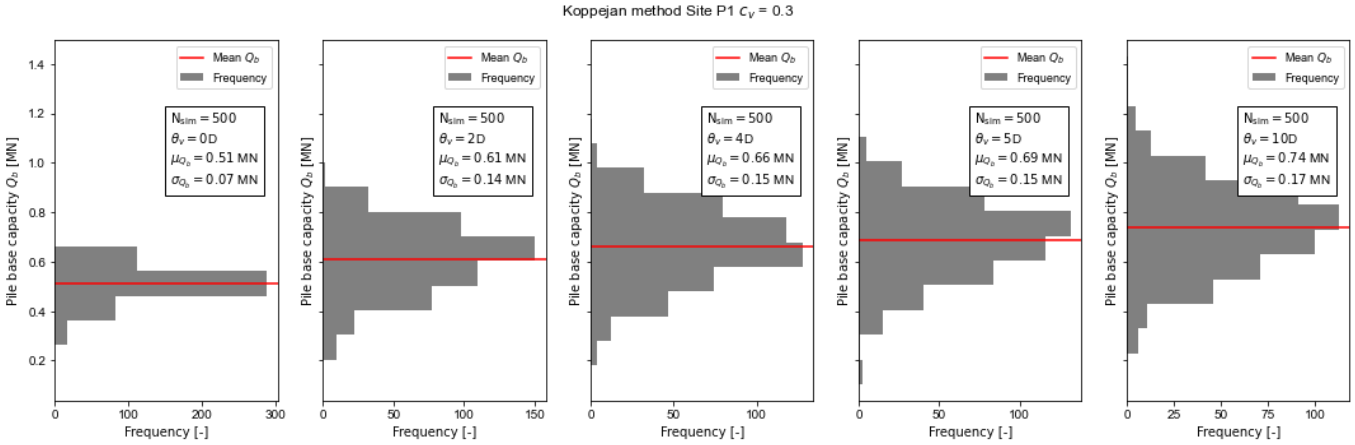

Figure D.57: Pile base capacities at site P1 for different vertical scales of fluctuation using Koppejan method.

Site P2

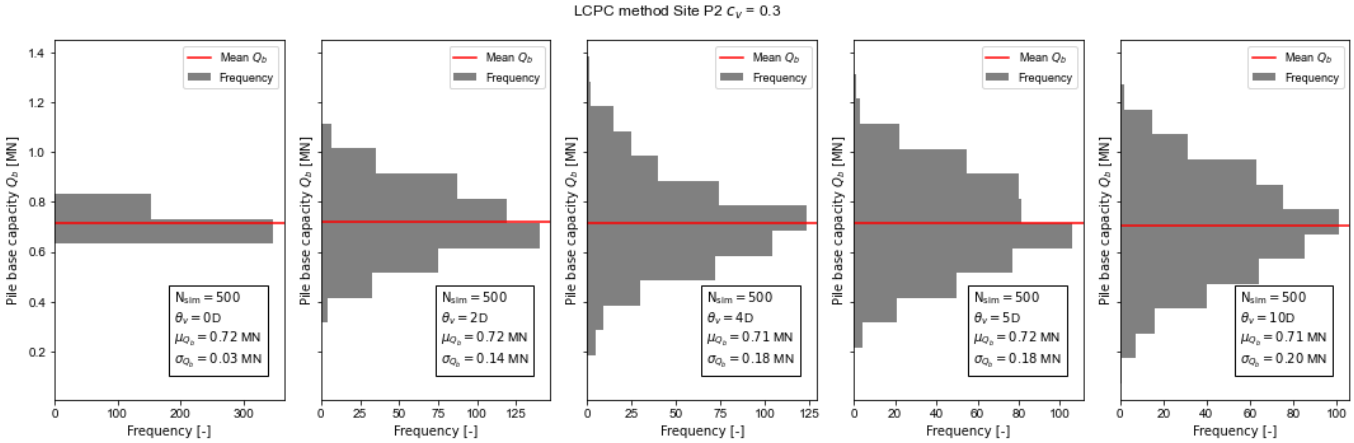

Figure D.58: Pile base capacities at site P2 for different vertical scales of fluctuation using LCPC method.

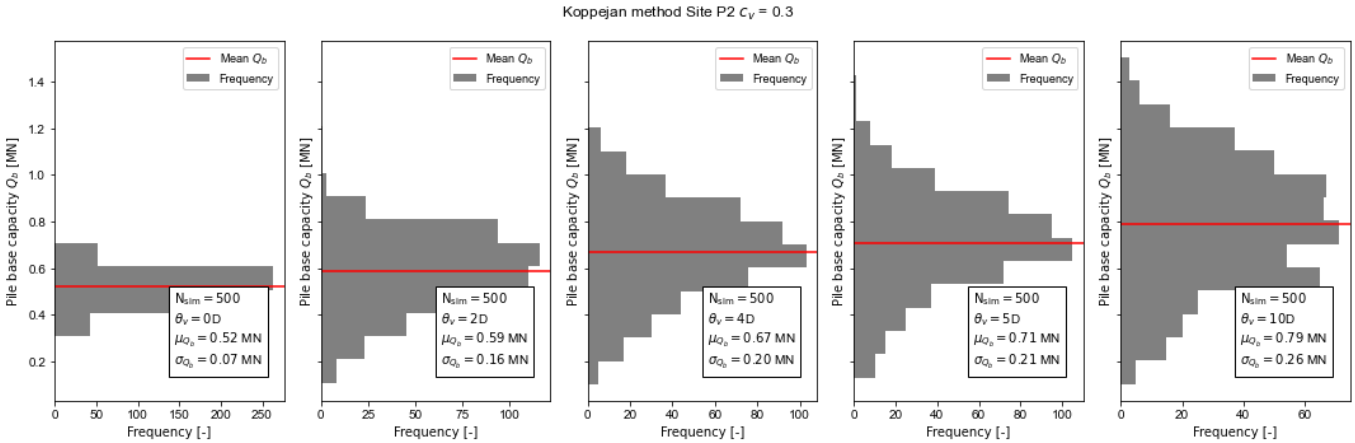

Figure D.59: Pile base capacities at site P2 for different vertical scales of fluctuation using Koppejan method.

Site P3

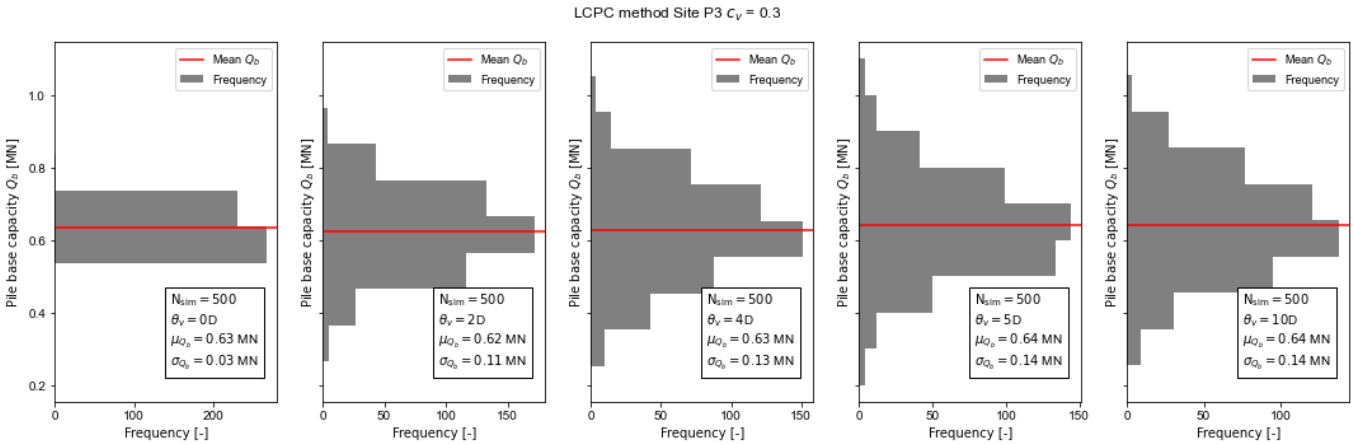

Figure D.60: Pile base capacities at site P3 for different vertical scales of fluctuation using LCPC method.

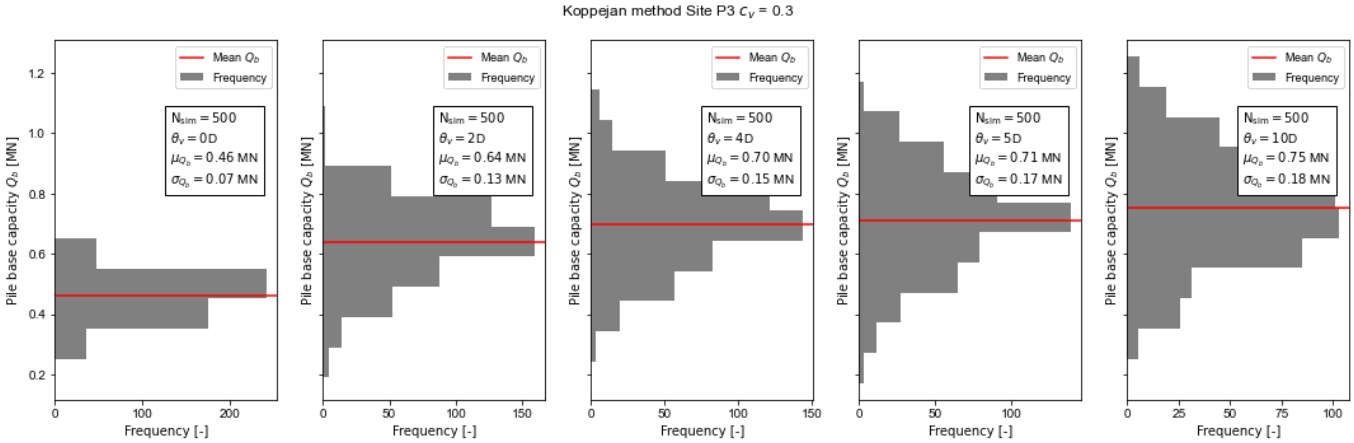

Figure D.61: Pile base capacities at site P3 for different vertical scales of fluctuation using Koppejan method.

Site P4

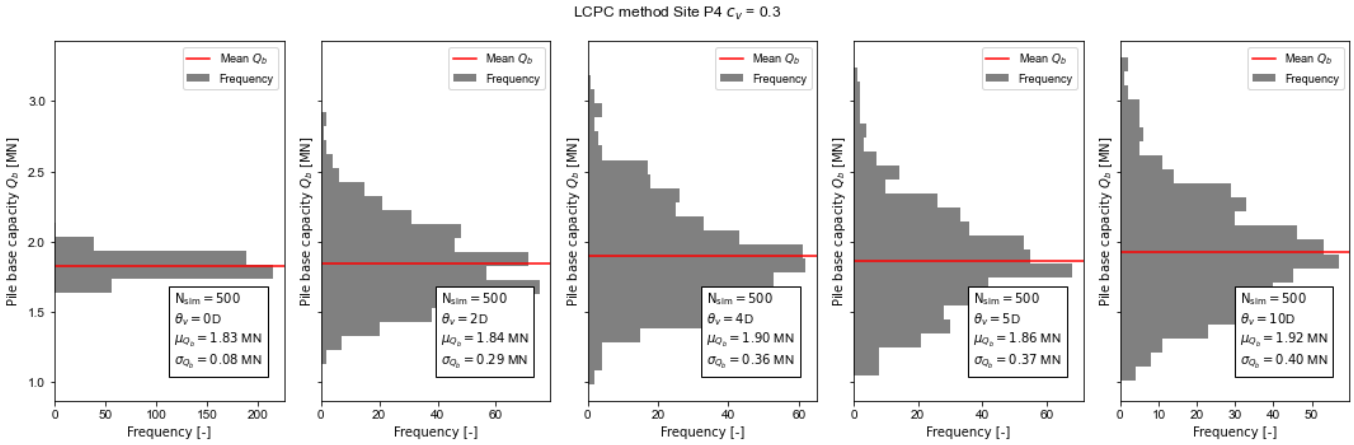

Figure D.62: Pile base capacities at site P4 for different vertical scales of fluctuation using LCPC method.

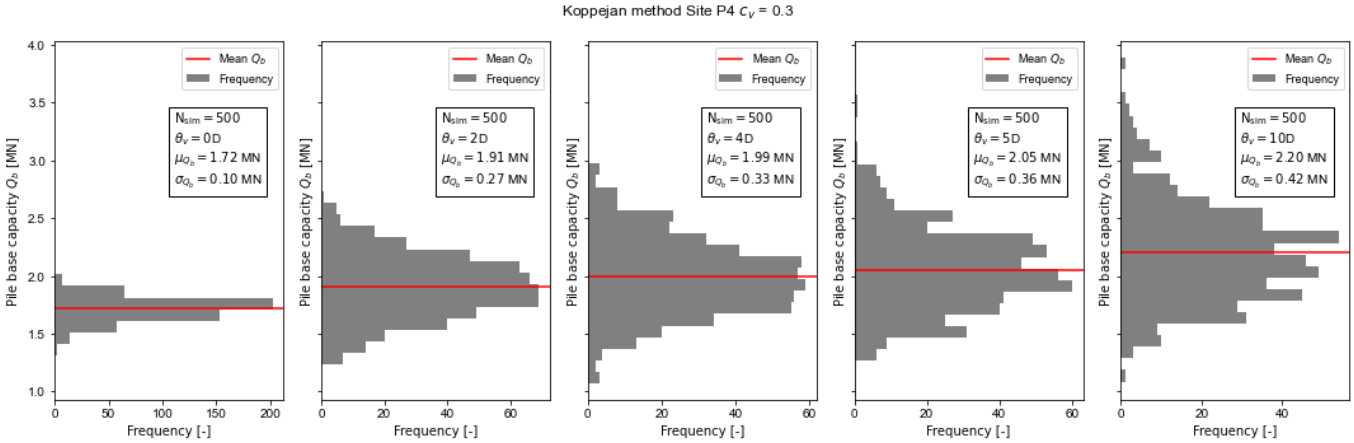

Figure D.63: Pile base capacities at site P4 for different vertical scales of fluctuation using Koppejan method.